Author:
Bloxham, Harry

Title:
Model updating using limited experimental data for the quantification of ultrasonic array inspection.

Model updating using limited experimental data for the quantification of ultrasonic array inspection.

Harry A. Bloxham

A dissertation submitted to the University of Bristol

in accordance with the requirements for award of the degree of

Doctor of Philosophy in the Faculty of Engineering

Department of Mechanical Engineering

January 2019

Word count: 33,542

Abstract

Ultrasonic non-destructive testing inspections using phased arrays are performed on a wide range of components and materials. All real inspections suffer, to varying extents, from coherent noise including image artefacts and speckle caused by complex geometries and grain scatter respectively. By its nature, this noise is not reduced by averaging; however, it degrades the signal to noise ratio of defects and ultimately limits their detectability. When evaluating the effectiveness of an inspection, a large pool of data from samples containing a range of different defects is important to estimate the probability of detection of defects and to help characterise them. For a given inspection, coherent noise is easy to measure experimentally but hard to model realistically. Conversely, the ultrasonic response of defects can be simulated relatively easily.

This thesis investigates a novel method of simulating realistic array data by combining noise-free simulations of defect responses with coherent noise taken from experimental data. This technique, referred to as the superposition technique, was validated both experimentally using samples with physical defects present and against FE models. It has been shown to provide accurate results over the full range of signal to noise ratios where the defect remains detectable. The work presented here expands the available modelling capabilities for ultrasonic imaging data for high noise inspections which has traditionally been difficult to achieve.

Acknowledgements

First and foremost I'd like to thank my supervisors, Sasha Velichko and Paul Wilcox, for their continued support and guidance through my PhD. Their knowledge and insights have been invaluable in producing the work presented here.

I'd also like to thank BAE Systems, Andy Nixon and Tom Barber, not only for their assistance in funding this work, but also their kindness in hosting me in their lab in Barrow-in-Furness on my multiple visits.

Jie Zhang has been a fount of knowledge whenever I've had any uncertainties and along with the rest of the NDT and ultrasonics group have always been there to offer a helping hand since my undergraduates projects in the department, for which I'm thankful.

Thanks must also go to my parents for their unconditional support throughout my education.

And last and most definitely least, no thanks at all to the coffee which killed my computer too close to the deadline for comfort.

Author's declaration

I declare that the work in this dissertation was carried out in accordance with the requirements of the University's Regulations and Code of Practice for Research Degree Programmes and that it has not been submitted for any other academic award. Except where indicated by specific reference in the text, the work is the candidate's own work. Work done in collaboration with, or with the assistance of, others, is indicated as such. Any views expressed in the dissertation are those of the author.

SIGNED: ..... DATE:.....

Thesis publications

1. Bloxham, H. A., A. Velichko, and P. D. Wilcox (2016). "Combining simulated and experimental data to simulate ultrasonic array data from defects in materials with high structural noise". In: *IEEE Transactions On Ultrasonics Ferroelectrics and Frequency Control* 63.12, pp. 2198–2206.

2. Bloxham, H. A., A. Velichko, and P. D. Wilcox (2018). "Establishing the limits of validity of the superposition of experimental and analytical ultrasonic responses for simulating imaging data". In: *IEEE transactions on ultrasonics, ferroelectrics, and frequency control*.

Contents

List of Figures

List of Tables

1 Introduction

1.1 Industrial motivation

It is common practice during the manufacture of safety critical systems for parts to be inspected for defects which may cause a failure during its service life. These inspections come in many forms from simple visual inspections, to eddy current and liquid penetrant inspections which are effective at detecting surface cracks, to ultrasound and X-ray inspections which are capable of analysing the full volume of the part (Hellier and Shakinovsky, 2001).

For each part, there is a defined maximum allowable size for each type of defect, any defect which exceeds these limits is considered a critical defect and remedial action must be taken to correct it. The nature of these critical defects and the geometry and material properties of the part to be inspected will determine which is the most suitable inspection method to use. This work was funded by BAE Systems Marine whose Astute class submarine requires tens of thousands of welds during manufacture. These consist of many different types, geometries and materials, which will each favour different NDE inspection methods and indeed a full range of difference techniques are used throughout the boat. The 'small-bore' class of pipes (30-60mm diameter) are currently inspected using X-ray film radiography. However, this method introduces safety risks due to the ionising radiation it requires. As such, its use requires severe restrictions on any concurrent work being carried out in the vicinity which results in increased manufacturing time and costs. Additionally, X-ray radiography is a poor technique for detecting cracks relative to ultrasound (Whittaker, 1972). As cracks have high stress concentration factors, it is important that the inspection method being used has good sensitivity to them. If these X-Ray inspections could be replaced by ultrasound, it is estimated that the NDE costs would be reduced by an order of magnitude and sensitivity to the most critical defects can potentially be increased and this is the goal at which the project is ultimately aimed at helping to deliver. There are several difficulties in achieving this however. Namely, the copper nickel alloy which

is used in the pipes due to its corrosion resistance is highly anisotropic making it challenging to inspect using ultrasound, and the curvature of the pipes and weld caps make coupling an ultrasonic transducer and interpreting the response difficult.

Advances in ultrasonic NDE methods mean that phased array imaging may now be a viable alternative to X-rays for this inspection and would remove the additional regulatory burden imposed by radiography. For any new inspection technique to be adopted, it must first be scrutinised in a validation study, the primary aim of which is to determine if the method is capable of detecting critical defects with acceptable false negative and false positive results. For this study to be performed, a data pool must be obtained covering a wide range of defect locations, sizes and types. This pool must be large enough such that reliable statistics can be drawn for the full range of defects. While it is possible to create this pool using only experimental data, the manufacture of samples with known defects present is costly which greatly limits the possible pool size (Thompson and Gray, 1986). In addition, they require independent means of testing to verify the exact nature of the defect further adding to the cost. The ability to create this data set predominantly from simulations would allow for large data sets to be created at only a computational cost (Ludwig and Lord, 1988) with the obvious benefits to industry. Such techniques are already common practice with less challenging inspections (Thompson et al., 2009).

1.2 Ultrasonic NDE inspections

The use of ultrasound as a method of flaw detection began with (Sokolov, 1929), initially via through-thickness measurements utilising two piezoelectric transducers, and later by pulse-echo measurements where one transducer is used for both transmission and reception. When excited by an electrical pulse, the piezoelectric element of the transducer will expand and contract, allowing it to create a mechanical wave. Conversely, if an external force is applied to this element, it will generate an electrical signal, a process which can be used to receive signals

(Berlincourt, 1971). Using a single monolithic transducer statically, it is only possible to capture one-dimensional information about the target. The information it produces is a time-trace of the received signal amplitude vs. time and is called an A-scan. With knowledge of the speed of sound of the material, this can easily be converted into a plot of depth vs reflected signal amplitude giving you knowledge of the depth of any discontinuity which would reflect an ultrasonic wave in the sample. While A-scans are effective at measuring material thickness, useful for monitoring corrosion and wear, and at detecting large defects, their usefulness is limited when attempting to detect smaller defects and determining their nature.

Initial attempts at producing two-dimensional images were made by combining A-scans taken at different physical positions or angles (Bradfield, 1954; Howry, 1957). However the major breakthrough in two-dimensional imaging came with phased array transducers, these consisted of multiple piezoelectric elements, usually arranged linearly, which could be controlled independently (Somer, 1968). By adjusting the relative phase of each element, beam-forming and electronic scanning techniques, already commonly used in sonar and radar (Welsby and Dunn, 1963; Allen, 1964), enabled the array to rapidly scan a volume of the sample and produce a two-dimensional image in real time using static hardware.

1.2.1 Imaging techniques

Traditional imaging techniques relied on transmitting on a subgroup of the array's elements, called a sub-aperture, to create an A-scan of the region directly below the sub-aperture. Using different sub-apertures, the section being inspected could be varied and a 2D image formed. The most basic way this was done, a plane B-scan, was by firing all of the elements of the sub-aperture in phase to emulate a single monolithic transducer, the amplitude vs. depth response of this would form one line of pixels in the image. After shifting the sub-aperture by one element, the process could be repeated and the adjacent line of pixels could be formed from the next A-scan. This is done over the full width of the array to form a 2D image. As these technologies

matured, more advanced imagine techniques developed. Focussed B-scans adjust the phase between elements in the sub-aperture, the transmitted beam can then be focused to a given depth, this reduces its divergence and improves its resolving power. Sector B-scans have also been in common use since the earliest days of phased array imaging, these use the full array as the sub-aperture and use the phase delays to steer the beam through various angles in a 2D image using classical beam forming. This allows a larger area to be imaged and is still common in medical imaging.

The logical conclusion of these developments would be to focus the full array, in both transmission and reception, at every pixel in the image, now referred to the Total Focusing Method (TFM). However achieving this poses challenges, both in terms of the hardware requirements that this would require, and the time that it would take to acquire a full data set. After any elements have been fired, sufficient time must be left to allow the sample to return to its unperturbed state before the next firing to prevent any interference between measurements. Much of the research in the area by this point had been focussed on medical imaging where it is a requirement to be able to capture the data in a short time frame due to the transient nature of many medical targets, for example a beating heart. This is also a requirement to a lesser extent in NDE to allow the operator to scan a large area in a reasonable time.

It wasn't until there were sufficient improvements in computing power that this method became practicably achievable. The development of post-processing techniques meant that it was possible to move away from physical beam-forming at the time of transmission and take advantage of the linear nature of ultrasound to apply the imaging algorithm at a later time (Holmes et al., 2005). To do this requires a Full Matrix Capture (FMC) data set, this consists of the time-trace for all transmit-receive pairs of elements in the array and is acquired by firing each element of the array in turn while receiving on all elements. The previously discussed imaging techniques can be recreated from this data set by summing the relevant time-traces with the appropriate delays to recreate any sub-aperture. While acquiring an FMC data set is slower than a tradition B-scan, it is not significantly so and post-processing the data allows much

more complex imaging algorithms to be applied which are not practical using traditional beamforming methods such as an iterative auto-focusing algorithm to account for unknown surface profiles of the sample (Hunter et al., 2010). The Total Focusing Method synthetically focuses the array at every pixel in the image by applying the appropriate time delay to coherently sum the response at pixel in the image, it has been shown to provide significant improvements in imaging resolution over traditional B-scans (Holmes et al., 2005). The time delays used for this technique are calculated as follows,

$$I(x,z) = \left| \sum_{i=1}^{N} \sum_{j=1}^{N} f_{ij} \frac{\sqrt{(x_i - x)^2 + z^2}\sqrt{(x_j - x)^2 + z^2}}{v} \right|, \tag{1}$$

where $I(x,z)$ is the image amplitude at the coordinates (x,z), N is the number of elements in the array, f_{ij} is the response in the time-domain transmitting on the ith element and receiving on the jth, x_i and x_j are the x-positions of the centre of the ith and jth elements respectively and v is the speed of sound in the sample being imaged. This assume an homogeneous and isotropic material on a macro level, this is valid for most cases however, for small-bore pipe welds, the weld material's properties will differ to that of the parent material so the time delays would have to be modified for this case to account for the different speeds of sound.

While B-scans image a two-dimensional cross-section of the specimen in the x and z dimensions where x is the dimension along which each of the array's elements are place and z is the depth, C-scans produce an image of the x-y plane. These are created by raster scanning a single transducer over the surface of the component and are useful for the likes of corrosion mapping (Iyer et al., 2005) and impact damage (Růžek et al., 2006). While they can cover a larger area than phased array B-scans, they are not as sensitive to small defects. The challenge imposed in the inspection of small-bore pipes requires the resolving power which is currently only available in ultrasonics with phased arrays. Because of this, TFM B-scans are used as the sole imaging technique in this thesis.

1.3 Structural noise

There are two categories of noise that can negatively effect the results of NDE inspections, coherent and incoherent. Incoherent noise sources such as random electrical noise introduced by the array controller will be different for every measurement taken, because of this it can be reduced by averaging and is therefore not a focus of this work. Coherent noise sources are inherent of the inspection and will not vary between measurements and can therefore not be reduced by averaging. It is this noise that poses the most serious challenges to inspections and the most common cause of it is backscatter from grain boundaries.

1.3.1 Grain scatter

Metals are a polycrystalline material by nature. Any given metal sample will be formed of many individual grains. The exact grain structure present is dependant on a variety of factors. Initially it will set depending on the conditions under which the material solidified when cast, however, heat-treatments, machining, working, welding and any other process which physically alters the sample is likely to change its internal structure.

Each of these crystals is anisotropic in nature but due to the generally random orientation of these grains, the bulk properties tend to exhibit isotropic properties if the grains on average, have approximately the same dimensions in all axes and are randomly orientated. However, on a micro-scale, any elastic wave propagating through the material will have to cross many grain boundaries which will, depending on the grains relative orientation, present a change in refractive index to the wave. This causes dispersion and scattering as the wave refracts and reflects (Huntington, 1950; Stanke and Kino, 1984). When averaged over the many thousands of grains in the thickness of a typical engineering sample, this manifests as a reduction in amplitude of the forward propagating wave combined with back scatter which presents noise in a single time-trace and as speckle in the resultant image from an array. This image speckle is caused by

the superposition of array responses from many grains with spatial variations dependant on the ultrasonic frequency used and does not directly correlate to the position of individual grains (Yu et al., 2010). This significance of this effect depends on the grain size relative to the wavelength, the grain orientations, and the level of anisotropy in each grain (Mason and McSkimin, 1948). An example of this speckle is seen in figure 1.1. For reference, typical grain sizes in copper are 100-200 µm.

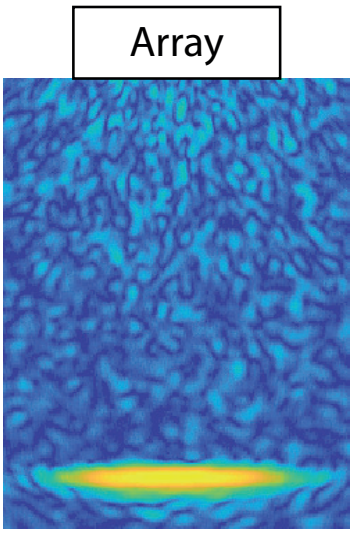

Figure 1.1: An example TFM image showing speckle, a back wall and the location of the array.

1.3.2 Attenuation

As a mechanical wave propagates through a medium, its amplitude progressively reduces due to two main mechanisms of attenuation. The most simple of these, geometric attenuation, is a product of the conservation of energy. As a wave spreads spatially, its total energy must remain constant and therefore the amplitude at any given point must reduce as the wave front occupies a progressively larger area.

The other major mechanism is a result of the scattering that occurs, in this case, at grain

boundaries. At each discontinuity in the material, some energy will be lost to signals which are scattered in directions different to the bulk wave. This attenuation in polycrystalline materials is a much studied subject with three distinct regimes. When the wavelength is much larger than the grain size (Papadakis, 1963), the attenuation and frequency relationship follows a Rayleigh regime (Rayleigh, 1896) which is effectively a single scattering regime. When the grain size and wavelength are of comparable size, there is a stocastic relationship (Huntington, 1950) and for wavelengths much smaller than the grain size, there is a geometric regime (Mason and McSkimin, 1948). Stanke and Kino (1984) proposed a unified theory which covered the full range of grain sizes, their results are shown in figure 1.2.

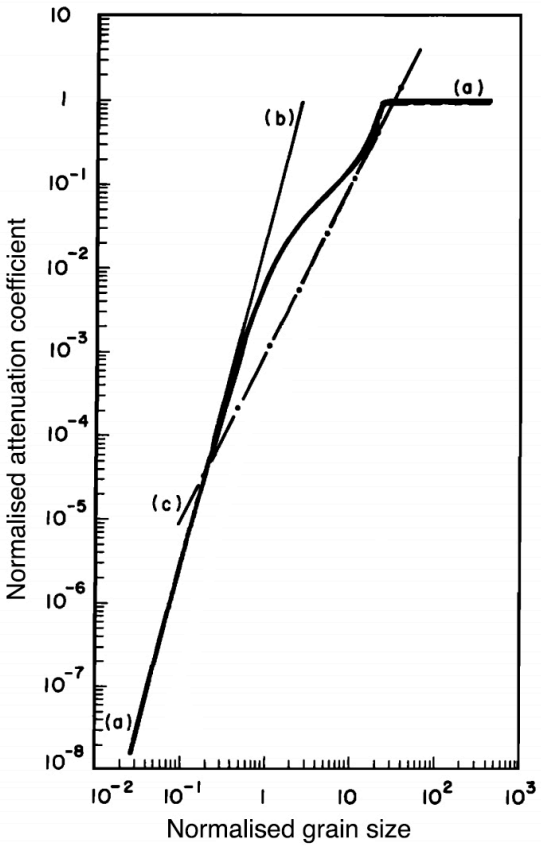

Figure 1.2: The Stanke and Kino unified theory attenuation curve for iron (a) with the Rayleigh limit (b) and stochastic asymptote (c) (Stanke and Kino, 1984).

The Rayleigh regime can be seen in figure 1.2 where the unified theory (a) agrees with the Rayleigh limit (b), the stochastic region is between where (a) departs from (b) and where (a) meets the stochastic asymptote (c) and the geometric region is the region beyond (c).

Absorption, caused by the conversion of mechanical energy within the material into heat, also contributes to the total attenuation. These loses however are generally orders of magnitude lower than those caused by scattering (Willems, 1987) for the inspections relevant to this thesis and its effects are not significant for the materials studied in this work.

1.3.3 Artefacts

In addition to grain speckle, many inspections, especially of complex geometries, exhibit other artefacts as a result of e.g. multiple reflections, diffractions at sharp corners and wave mode conversions. While in theory these artefacts can be modelled accurately, the compound nature of their formation means that they are extremely sensitive to any error in the either the simulated geometry or material properties making it practically challenging to simulate.

1.4 Single scattering assumption

The single scattering assumption assumes that the ultrasonic ray in question is emitted by an array element, reflected by a scatterer, and then received by an array element. This leads to the result that the response of a system can be expressed as the sum of the individual response of each scatterer in the system. i.e. that it is a linear system and there is no interaction between scatterers. This is a commonly held assumption in ultrasonics and is one which is used by imaging algorithms, including TFM, to sum the response from a given point in the image coherently. Despite its wide use, there is usually some level of multiple scattering occurring in reality. In low noise regimes this is normally of little consequence with the only commonly visible effect being shadowing of the back wall by defects caused by multiple scattering between

a defect and the back wall, not by interactions between grains.

Even in specimens of moderate noise it is an assumption that can be empirically shown to be valid, indeed Margetan et al. (1993) produced and validated a model for grain back scatter produced by the sum of the single scattering response of a series of randomly positioned scatterers in an otherwise homogeneous and isotropic medium. It was suggested by Wilcox et al. (2011) that single scattering models are appropriate for the majority of the frequency range of interest for NDE applications, however multiple scattering does begin to dominate the response at low SNRs so it must be given attention in these scenarios. While the majority of imaging algorithms are dependant on the single scattering response of the system, there are modern techniques, such as the multiple scattering filter (Shahjahan et al., 2014), which allow defects to be detected beyond the point where multiple scattering dominates.

1.5 Superposition of data sets

Under the assumption of single scattering, ultrasonic measurements can generally be considered a linear system meaning that the sum of the response from two separate signals is equal to the response of both signals occurring simultaneously. Taking advantage of this, the response of a defect in a sample containing high levels of structural noise can also be described as the sum of the response from the defect-free sample and the response from the defect in a noise-free sample of the same geometry. The benefit of this is that the high noise defect-free sample response is easily acquired experimentally and the defect response from a noise-free sample can be simulated accurately using a range of well established methods.

There are several methods currently used to simulate ultrasonic back scatter and image speckle. The most common method is to model a series of omni-directional point reflectors in the parent material (Margetan et al., 1993; Cohen, 1992; Yalda et al., 1996) which has been shown to provide realistic results. Stochastic models have also been used successfully (Derin et al., 1990) and more recently FE techniques have become commonplace (Ghoshal and Turner, 2009;

Van Pamel et al., 2017; Bai et al., 2018) to model the individual grains within the full structure to predict the expected backscatter. While each of these methods are capable of producing results that accurately match experimental data, achieving sufficient accuracy requires detailed knowledge of the material being studied including grain size, orientation and phase distributions as well as the anisotropic stiffness constants of the grains. These parameters are rarely readily available and are often difficult to determine experimentally.

The superposition technique would provide method of simulating defects in a noisy material without the difficulties usually associated with accurately simulating that noise.

These principles have recently been used by Dobson and Cawley (2016) for guided waves in inspections with low levels of structural noise. However, no attempt was made to validate their method against experimental data.

1.6 Aims and objectives

In order for BAE to replace X-ray radiography with phased array ultrasound imaging for their small-bore pipe inspections in the Astute class of submarine, both the challenges associated with the high noise material and pipe geometry need to be solved. The issues associated with the geometry are actively being researched (Barber, 2017) and is beyond the scope of this work. This thesis will focus on the difficulties presented by high noise materials.

The motivations behind this work are to improve the currently available capabilities of accurately and efficiently simulating ultrasonic phased array data for NDE purposes in inspections where this has traditionally been difficult to achieve due to coherent noise. The currently available models, as described in the previous section, all require empirical tuning to accurately match the material in question which is non-trivial and the accuracy is not guaranteed.

A model will be developed based on the superposition of readily available experimental data with easily simulated defect responses with a focus on creating a reliable procedure which can

readily be adopted in industry and which requires a minimum amount of empirical data to achieve accurate results. By using experimental data to directly create the noise in the image, it ensures that the resultant image is a realistic representation of the true noise as could be expected in any future experimental measurements.

The limits of this model will also be tested to determine what scenarios this is likely to be an appropriate modelling methodology for and when it is likely to fail.

1.6.1 Thesis outline

Chapter 2 details the model which was used for simulating the ultrasonic response from defects as well as presenting experimental results to validate it. It goes on to validate this model experimentally and discusses its limitations

In chapter 3, the method of producing simulated data to superimpose with experimental data is presented and the full process which is to be followed is described along with the required assumptions of the model.

Chapter 4 compares the results of the superposition technique to experimental data to show that it is a valid technique to be used to simulate ultrasonic imaging data in noisy samples for defects at a range of depths and positions relative to the array.

Chapter 5 furthers the results of chapter 4 using FE an model to determine the regimes over which the proposed technique can be expected to produce accurate results. It also shows the effects the un-modelled multiple scattering between the defect and grains has on the superposition technique's accuracy.

Chapter 6 discusses the potential benefits this model can bring to the NDE industry and demonstrates the potential of the technique in an analysis using large volumes of data which it has created.

2 Simulating ultrasonic data

This chapter describes the model used in this work for the simulation of analytical ultrasonic imaging data, while the model itself is not novel, there are several subtleties introduced which must be adhered to in order for it to be used in the proposed superposition technique. The description of this model is also found, in a more concise form, in Bloxham et al. (2016).

For the purposes of evaluating the superposition technique, a model capable of simulating the ultrasonic response of a range of defects is required. The principles behind simulating ultrasonic imaging data has been known for several decades (Hasegawa and Yosioka, 1969; Bamber and Dickinson, 1980) and there are a range of established techniques capable of achieving this using analytical (White, 1958; Schmerr, 1998), semi-analytical (Felice et al., 2015) and numerical methods (Lord et al., 1990).

The superposition technique is independent of the modelling method used for the defect response, it only requires it to be accurate. In this work, there is a preference to use analytical models where a solution exists due to their computational efficiency over numerical methods.

Most commonly used transducer arrays have an element length, in the dimension normal to the imaging plane, much greater than their width. For modelling purposes, it is common to assume that the elements are infinitely long, this allows the model to be collapsed into a 2D plane and is an assumption used in the majority of the literature. This places the restriction of only being able to model defects and interfaces which are also infinitely long in the same dimension. 3D models are available however they greatly increase the computational cost. This 2D assumption neglects any beam spread normal to the imaging plane which would occur in reality, the significance of this effect is dependant on the relative sizes of the wavelength being used, the 3D element's length and the propagation distance of the wave but is often not significant in the type of inspection geometries discussed in this work. It is also not possible to simulate defects which are not uniform along the collapsed dimension which limits its use in modelling

several types of realistic defects such as pores, inclusions and non-uniform cracks.

2.1 Ray tracing model

2D ray-tracing techniques are widely used (Liu and Wirdelius, 2007; Felice et al., 2015; Zhang et al., 2018) and have become an established technique for the simulation of ultrasonic data. It also forms the basis of the commercial package CIVA (Iakovleva et al., 2014) which is both well used and validated in both industry and academia. This method considers the propagation of the sound wave along all relevant ray paths connecting two point sources, the transmit and receive locations. While there are an infinite number of ray paths connecting any two locations, under the single scattering assumption and with a finite number of reflectors, there are a finite number of ray paths which will arrive within the time frame of interest for the imaging algorithm being used. For a single defect and back wall being imaged with standard (no skips) TFM, these ray paths are shown in figure 2.1. The calculations can be performed in either the time or frequency domains, however as many of the interactions are frequency dependant, calculations are more easily performed in the frequency domain and hence it was chosen for this work. The model described here was implemented using MATLAB.

To calculate the path each ray takes, first the model geometry must be defined as a series of reflectors. For the purposes of modelling, these are split into two main groups, planar reflectors and omni-directional scatterers. Ray paths incident on a planar reflector (such as a back wall) must reflect at angles which satisfy Snell's law whereas rays hitting a scatterer will reflect in all directions with an amplitude defined by a scattering matrix (Varatharajulu and Pao, 1976). Scattering matrices allow any defect to be defined as a point target and define the reflected signal's phase and amplitude as a function of the incident and reflected wave boundaries. For side-drilled holes, an exact analytical solution exists (White, 1958) but for more complex defects, numerical methods must be employed. FE models allow the scattering matrix to be calculated for a defect of any geometry (Wilcox and Velichko, 2010) which makes the ray-tracing method

very flexible in terms of defect types which can be simulated.

The material is assumed to be homogeneous on a macro scale meaning that the rays can only travel in straight lines. For the direct contact case, the ray paths of interest are shown in figure 2.1.

The response from the scatterer and the back wall are obtained using rays a and b while rays c, d and e are used to calculate any shadowing effects caused by multiple scattering between the scatterer and the back wall. Shadowing occurs due to interference between the scattered signals on paths c, d and e with the directly-reflected signal from the back wall on path a. In an image, this results in an area of lower intensity at a point on the back wall, typically directly behind the scatterer.

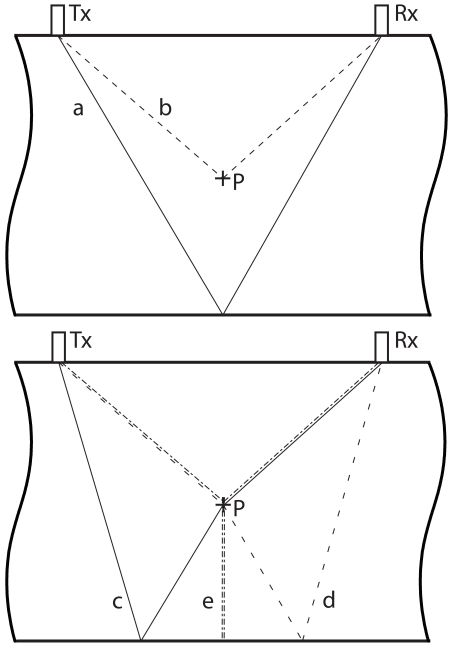

Figure 2.1: Direct ray paths, a and b, and secondary ray paths, c, d and e, in a sample with a scatterer located at P where element Tx is transmitting and element Rx receiving.

These ray paths assume the simple case of a single defect present in a single material. The reality of small-bore pipes is that the weld material exhibits different properties to that of the parent material and will present another interface at which the rays will refract and reflect

which would introduce additional ray paths which need to be accounted for. The paths these rays take can be calculated using Fermat's principle (Ben-Menahem and Singh, 2012) but the full complexity of modelling such a geometry is beyond the scope of this work, it can however be seen in Budyn et al. (2019).

2.1.1 Calculating the ultrasonic response

Calculating the ultrasonic response from each of these ray paths can be done as follows:

Ray path a: Each element of the array has varying abilities to transmit and receive at different angles relative to its normal, to account for this and remove the assumption that each element is a point source from the ray tracing model, a directivity function, $D(\phi, \omega)$, is needed. The exact solution for an infinitely long line source is given by Miller and Pursey (1954) but for longitudinal waves, $\cos\phi$ provides a reasonable approximation. Integrating over the length of a finite-sized element results in an additional *sinc* term to give a directivity function of:

$$D(\phi, \omega) \approx \operatorname{sinc} \frac{\pi a \sin\phi}{\lambda} \cos\phi, \tag{2}$$

where a is the element width, ϕ is the angle between the ray and the normal of the element and λ is the wavelength.

For an array with an element width of 0.35 mm transmitting into copper, the directivity pattern, as calculated with (2), can be seen in figure 2.2

The amplitude of the signal is attenuated as it propagates by two mechanisms, both of which must be accounted for. The first is geometric attenuation, A_g^a, caused by the beam spreading spatially as it propagates and is calculated using:

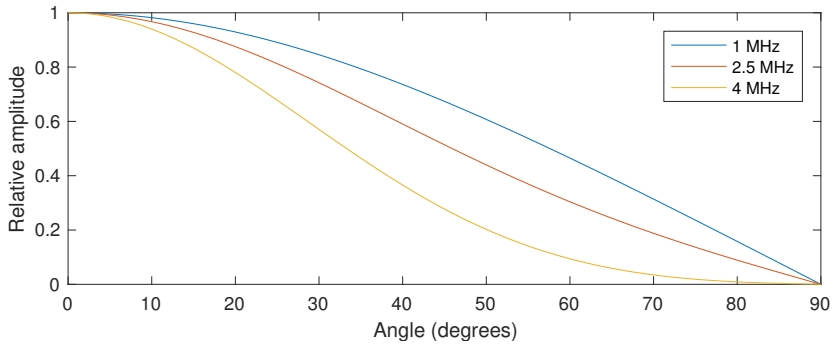

Figure 2.2: The directivity pattern for an element 0.35 mm wide in copper.

$$A_g^a = \sqrt{\frac{1}{R_t + R_r}}, \tag{3}$$

where R_t and R_r are the distances from the transmission and reception elements to the back wall respectively. If the array and back wall are parallel then R_t will equal R_r.

The second type of attenuation is caused by dissipation mechanisms and is dominated by grain scatter. It is defined as $A_s(\omega)$ and is calculated using:

$$A_s(\omega) = e^{-\alpha R}, \tag{4}$$

where α is the frequency-dependant attenuation coefficient and R is the total propagation distance.

The phase change due to wave propagation, $T(\omega)$, (equivalent to a time delay in the time domain) is calculated with:

$$T(\omega) = e^{-ikR}, \tag{5}$$

where k is the wavenumber.

When a longitudinal wave is incident to a boundary between two different materials, its

energy is split between the reflected and the transmitted longitudinal waves and any shear waves which are generated. The proportion that is reflected as a longitudinal wave is defined as the reflection coefficient, from a planar surface, such as a back wall, can be calculated analytically. For a solid-vacuum interface, the formula is:

$$C_r(\phi_i) = \frac{\cos^2(2\phi_s) - \frac{c_s^2}{c_l^2}\sin(2\phi_s)\sin(2\phi_i)}{\cos^2(2\phi_s) + \frac{c_s^2}{c_l^2}\sin(2\phi_s)\sin(2\phi_i)}, \tag{6}$$

where ϕ_i is the angle of incidence at the back wall relative to its normal, ϕ_s is the angle of the reflected shear wave calculated using Snell's law and c_s and c_l are the shear and longitudinal speeds of sound respectively (Tattersall, 1973).

These parameters describe the transformation of a transmitted signal from an element into the received signal so in addition, the frequency spectrum of the input signal, $F_0(\omega)$ is also needed.

The product of all of these factors gives the ultrasonic response from ray path a. However, many of them are common to all of the ray paths so for ease of notation, they are defined as:

$$F_{com}(\omega) = F_0(\omega)D(\phi_t, \omega)D(\phi_r, \omega)A_s(\omega)T(\omega), \tag{7}$$

and the response from ray path a is calculated using:

$$F_a(\omega) = F_{com}(\omega)C_r(\phi_t, \phi_r, \omega)A_g^a. \tag{8}$$

Ray path b: Where as ray path a is the direct reflection off of the back wall, ray path b is the direct reflection off the defect. The main difference in the calculation of the response from these paths is that the defect requires the use of a scattering matrix, $S(\phi_t, \phi_r, \omega)$, rather than a reflection coefficient. The geometric attenuation factor is also modified to:

$$A_g^b = \sqrt{\frac{1}{R_t R_r}}. \tag{9}$$

The ultrasonic response from ray path b is then given by:

$$F_b(\omega) = F_{com}(\omega) S(\phi_t, \phi_r, \omega) A_g^b. \tag{10}$$

Ray paths c & d: Ray paths c and d reflect off both a planar interface and a scatterer, therefore both a reflection coefficient and scattering matrix are required. The geometric attenuation is defined as in (9) but where R_t is equal to the total ray path length before the scatterer and R_r is the total length after the scatterer.

The response of these ray paths is given by:

$$F_c(\omega) = F_{com}(\omega) C_r(\phi) S(\phi_{rs}, \phi_r, \omega) A_g^b, \tag{11}$$

$$F_d(\omega) = F_{com}(\omega) C_r(\phi) S(\phi_t, \phi_{ts}, \omega) A_g^b, \tag{12}$$

where ϕ_{rs} is the angle of incident at the scatterer and ϕ_{ts} is the angle of reflection at the scatterer.

Ray path e This final path interacts with the scatterer twice, therefore two pairs of incident and reflected angles are required for the scattering matrix. $S_1(\phi_t, \phi_{bw}, \omega)$ is for the first interaction and $S_2(\phi_{bw}, \phi_r, \omega)$ the second. The angle of incidence at the back wall will always be equal to the back wall normal for this path and defined as ϕ_{bw}, for this case, the reflection coefficient can be approximated as -1 when the back wall is coupled to air. A_g also requires special attention for this path and is defined as follows:

$$A_g^e = \sqrt{\frac{1}{R_t R_s R_r}}, \tag{13}$$

where R_t is the ray path length between the transmitter and the scatterer, R_s is the ray path length between the first and second interactions with the scatterer (equal to twice the distance between the scattered and the back wall) and R_r is the path length between the scatterer and receiving element.

The response due to the wave propagating along this path is calculated using:

$$F_e(\omega) = -F_{com}(\omega)S_1(\phi_t, \phi_{bw}, \omega)S_2(\phi_{bw}, \phi_r, \omega)A_g^e. \tag{14}$$

The total response for a given transmit-receive pair of elements is then calculated as the sum of the above ray paths:

$$F(\omega) = F_a(\omega) + F_b(\omega) + F_c(\omega) + F_d(\omega) + F_e(\omega), \tag{15}$$

and this process is repeated for all possible transmit-receive pairs of elements to created an FMC data set. To return this data set to the time domain, an inverse Fourier transform is applied,

$$f(t) = \frac{1}{2\pi}\int_{-\infty}^{\infty} F(\omega)e^{i\omega t}d\omega, \tag{16}$$

where $f(t)$ is the FMC data in the time-domain.

2.1.2 Experimental measurements

For the numerical simulation to be accurate, several parameters must be determined experimentally. These are the geometry of the inspection, the material properties of the test sample and couplant if not direct contact and the response from the array.

The geometry of the inspection includes the test specimen's and defect's dimensions, as well

as the array geometry and their relative positions. The material properties which are required include the speed of sound, acoustic impedance (required to calculate the scattering matrix) and frequency dependant attenuation coefficient. The input signal and each element's relative amplitude must also be known which is detailed in section 2.2.1. It is likely that many, if not all, of these parameters can be determined using the defect-free data to which the simulated defect response will be summed. If this is not possible for all of them, only a single additional experimental sample is required from which all of the listed parameters can be calculated.

The speed of sound, v, is easily calculated using a time of flight measurement. Once this is known, the material's density, ρ can be measured, the acoustic impedance, Z is then calculated as follows,

$$Z = \rho v. \tag{17}$$

The most difficult of these to measure is the attenuation caused largely by scattering at grain boundaries. This property is frequency dependant and must be known over the full range of frequencies used in any simulation. However, it is often difficult to measure the attenuation over the full bandwidth of the array therefore extrapolation is often required at either extreme of the frequency range.

Two methods of measuring this attenuation were used, direct contact and immersion.

The direct contact method involves recording the back wall reflection from two samples of the relevant material, each of a different thickness. This experimental setup can be seen in figure 2.3.

The first back wall reflection of each specimen is then as follows:

$$F_1^1(\omega) = F_i(\omega) R e^{-2\alpha(\omega) a_1}, \tag{18}$$

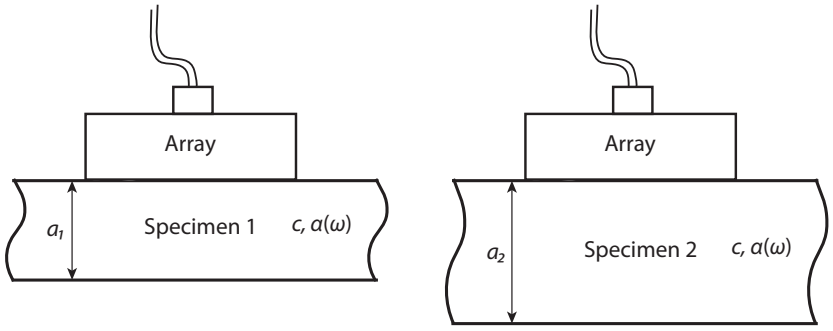

Figure 2.3: Experimental set-up for direct contact attenuation measurements.

$$F_1^2(\omega) = F_i(\omega) R e^{-2\alpha(\omega) a_2}, \tag{19}$$

where $F_1^2(\omega)$ is the first back wall reflection from specimen 2, $F_i(\omega)$ is the input signal from the array, R is the reflection coefficient for a wave incident at the back wall, $\alpha(\omega)$ the attenuation coefficient of the specimen and a_1 the depth of specimen 1. Rearranging gives:

$$\alpha(\omega) = \ln \left| \frac{F_1^1(\omega)}{F_2^1(\omega)} \right| \frac{1}{2(a_2 - a_1)}. \tag{20}$$

This method assumes a plane wave, to account for this, $F_1(\omega)$ is defined as the sum of all transmit-receive pairs of the array to simulate a monolithic transducer which would result in a close approximation to a plane wave. The errors this assumption introduces are very small relative to the total attenuation in the highly attenuative materials which this work considers. As the array size decreases, frequency increases or propagation distance increases, the errors introduced become larger and the assumption may cease be valid for some inspection geometries.

The use of two different samples also requires the coupling to be the same for the measurements from both specimens which requires care during the experimental set up and is extremely difficult to accurately control.

The immersion method can be performed with only one sample using the experimental set-

up showed in figure 2.4. The attenuation can be calculated using the front wall and first back wall reflections, $F_0(\omega)$ and $F_1(\omega)$ respectively;

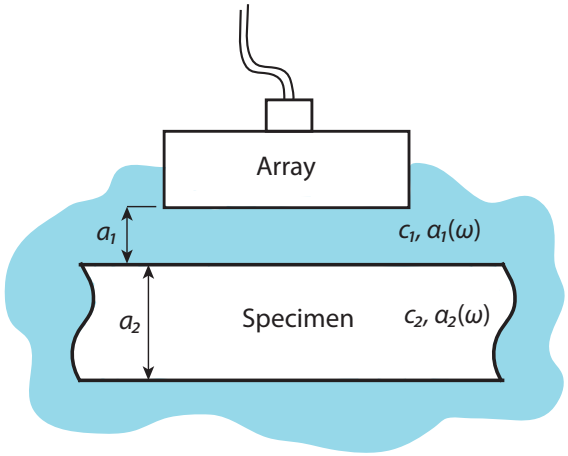

Figure 2.4: Experimental set-up for immersion attenuation measurements.

$$F_0(\omega) = F_i(\omega) R_{12} e^{-2\alpha_1(\omega) a_1}, \tag{21}$$

$$F_1(\omega) = F_i(\omega) T_{12} R_{21} T_{21} e^{-2\alpha_1(\omega) a_1} e^{-2\alpha_2(\omega) a_2}, \tag{22}$$

$$\alpha_2(\omega) = -\frac{1}{2a_2} \ln \left| \frac{F_1(\omega)}{F_0(\omega)} \frac{R_{12}}{T_{12} R_{21} T_{21}} \right|, \tag{23}$$

where R_{12} and T_{12} are the reflection and transmission coefficients from material 1 (water) to material 2 (the specimen), respectively and α_1 is the attenuation coefficient in material 1.

Each of these methods has its own advantages and required assumptions which will dictate which is the most appropriate for a given scenario. The direct contact case requires measurements from either a stepped sample or two samples of different depths which may be limiting in certain circumstances. It is also dependant on the coupling between the array and sample being

consistent across measurements. The immersion method can be performed with only one sample but it requires the reflection and transmission coefficients to be known as well as requiring an immersion tank and precision hardware to allow the accurate alignment of the array with the sample.

2.2 Modelling direct contact

There are two common coupling methods used between the array and the sample, direct contact and immersion. In direct contact inspections, as the name implies, the array is placed directly in contact with the sample with a coupling gel applied to facilitate the transmission of ultrasonic waves. Angled wedges may be used between the array and the sample to alter the area being imaged and to generated shear waves in the sample due to the transmitted longitudinal waves at oblique incidence to the sample. Direct contact has the practical advantage of being easily applied to any part whose surface matches that of the array (usually flat) however care must be taken to achieve consistent coupling between measurements if they are to be directly compared as the thickness of the film of couplant between the array and sample varies depending on the pressure being applied to the array which will alter the amount of energy being transmitted into the array.

Immersion inspections are also commonly performed where the array is positioned a distance away from the sample, either parallel to the surface or inclined at an angle, and the gap is filled by a liquid couplant, usually water. This requires the sample and array to be enclosed in a watertight container which means it is often practically difficult to achieve without specialist hardware unless the part to be inspected is small and easily moved. It does however offer the advantage of allowing for more consistent coupling and allows for the angle between the array and specimen to be easily varied to achieve the same effect as a wedge.

Direct contact inspections were used to validate the superposition technique as they are less complex to model and will therefore present fewer sources of error.

2.2.1 Validating experimentally

To ensure the ray-tracing model has sufficient accuracy to be used in in conjunction with the superposition technique, its results were compared to experimental measurements of defects and back walls at various depths. The experiments were performed on both aluminium and copper samples. These materials were chosen due to aluminium exhibiting very low attenuation at typical ultrasonic frequencies and copper, relatively high grain scatter. The specifications of the array used are listed in table 2.1 and its frequency spectrum is shown in figure 2.5. This was measured from the back wall signal in an aluminium sample. Varying the sample thickness used to calculate the frequency spectrum showed negligible changes in its distribution confirming that there is negligible frequency dependant attenuation in aluminium when imaged at these frequencies.

Array property	Value
Nominal centre frequency	2.5 MHz
Number of elements	64
Element pitch	0.5 mm
Element width	0.35 mm
Element length	15 mm

Table 2.1: Specifications of the array used for validation.

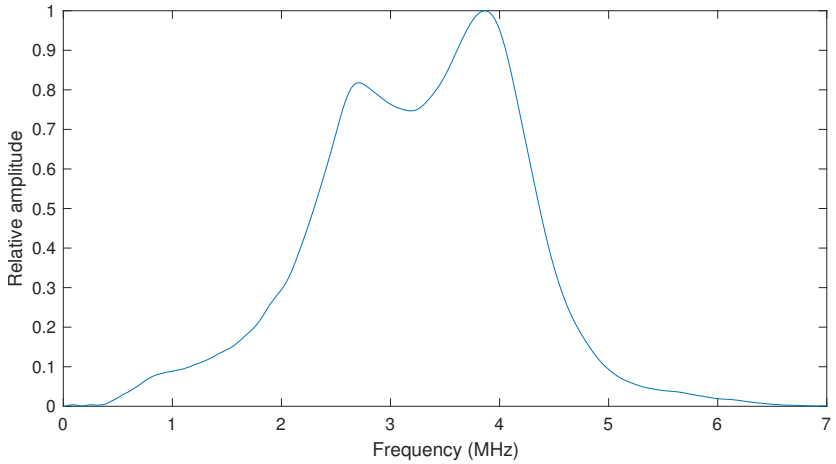

Figure 2.5: Frequency spectrum of the array used for experimental validation.

At frequencies used, the aluminium sample's attenuation was negligible meaning that its effects could be removed from the model. This allowed the underlying physics captured in the model to be tested and verified in its most basic form. Once validated in this form, the complexity of the model can be increased, potentially increasing the accuracy, but also adding additional sources of error.

The initial simulations were run using only the direct ray paths (a and b in figure 2.1) to compare the relative amplitudes of defects at various depths. The test sample consisted of 1.5 mm diameter side-drilled holes located at depths of 20, 40 and 60 mm in a 65 mm deep aluminium specimen. The speed of sound was calculated using the time of flight technique from the back wall and was found to be 6410 m/s. This was calculated from the difference in the time of arrival of multiple back wall echoes to remove the instrument delay.

The results of this initial simulation can be seen in figure 2.6, along with the experimental results for the 40 mm deep hole. Each image is normalised to its highest amplitude pixel, this is common practice to enable a direct comparison between data sets as the absolute values of the array data are subject to variation caused by many factors including the coupling fluid used, pressure on the array, controller settings and even environmental factors.

There are several clear differences in these results: the large area of low intensity signal in the upper region of the experimental image is an artefact from the 'ringing' during and after they have been excited. While the defects appear in the same location, their shape differs and the amplitude of the simulated defect is approximately 3 dB lower than in the experimental image. Finally the back wall has a clear dip in amplitude at its centre on the x-axis in the experimental image which isn't present in the simulated data as well as what appears to be echoes of the back wall just behind the back wall location. It is worth noting that as the images are normalised to their brightest pixel (at the back wall in this case), any error in this pixel will manifest as a DC offset in the remainder of the image. Therefore the image amplitude error at the defect is a combination of the errors in the defect and the back wall.

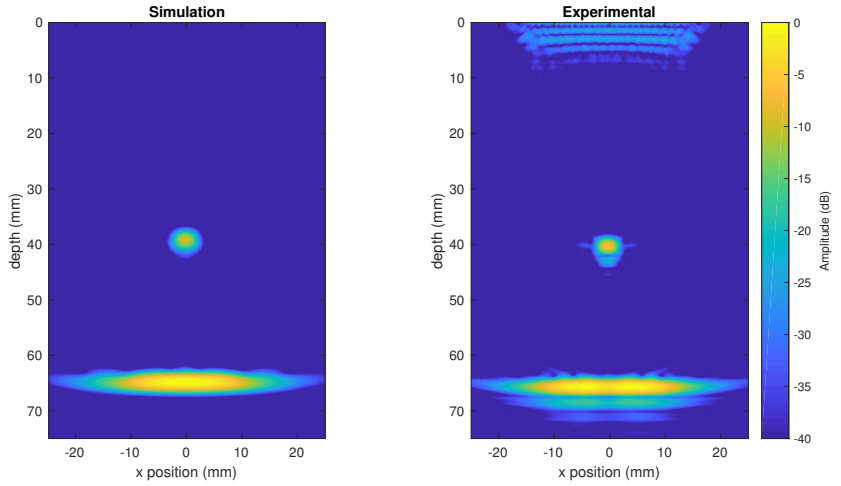

Figure 2.6: TFM images of the result of the ray-tracing model using ray paths a and b for a 1.5 mm diameter side-drilled hole at a depth of 40 mm (left), and the equivalent experimental results (right).

The dip in back wall amplitude at its centre is due to a shadowing effect caused by the defect blocking some of the array's transmission from reaching the back wall. To account for this, ray paths c, d and e from figure 2.1 are included in the simulation. As these ray paths only affect the back wall, figure 2.7 shows a comparison between the model including the secondary ray paths, a-e for the same geometry as in figure 2.6 but cropped to show only the back wall.

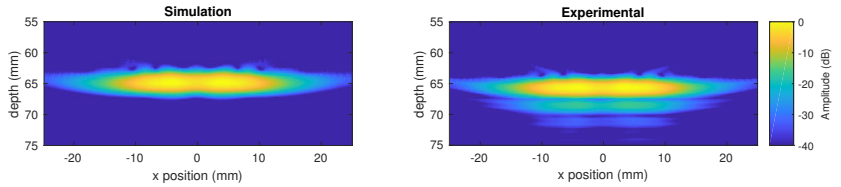

Figure 2.7: TFM images of the result of the ray-tracing model using ray paths a-e cropped to show only the back wall for a 1.5 mm diameter side-drilled hole at a depth of 40 mm (left), and the equivalent experimental results (right).

Figure 2.7 shows that with the addition of these secondary ray paths, the back wall begins to provide a more accurate prediction of the shape of the back wall along with shadowing effects produced by a defect. There are still discrepancies between the results however. The feature at the top of the experimental image is a product of the array elements ringing after being fired which is unnecessary to account for in this work as it is not the result of an interaction with the

sample and is an artefact of the hardware used. Differences can also seen in the regions below and to the sides of the defect and below the back wall which are caused by different input signals being used in the model and the physical array.

To increase the accuracy further and reduce these discrepancies, several experimental variables are added to the model. The most significant of these is matching the input signal of the model to the one produced by the array. The output amplitude of each element may also differ in a physical array, to account for this, the square root of the relative absolute amplitudes of the pulse-echo response from each element can be used to scale the output and reception of each element in the simulation if the array is known to exhibit significant variations between elements. The instrument delay also needs to be accounted for which will defocus the image if left uncorrected. As the sample's geometry and the material's speed of sound are already known, this delay is easily calculated by taking the difference between the time of arrival of the back wall signal as measured by the array and the expected time of arrival calculated from the wave velocity and sample depth.

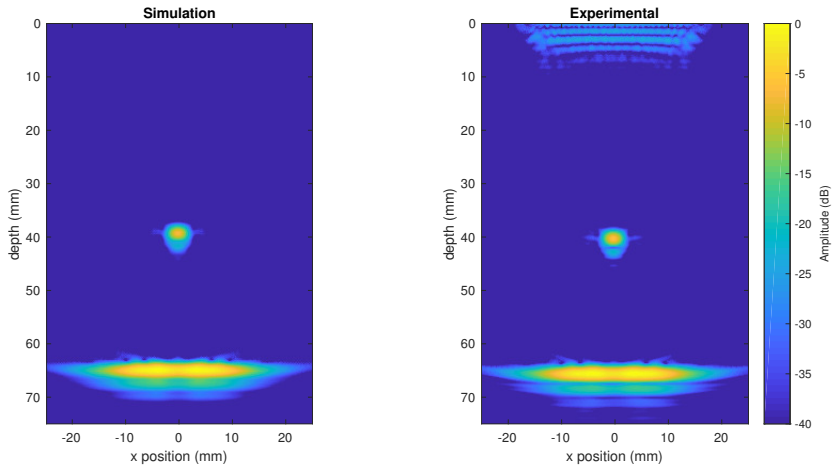

Figure 2.8: TFM images of the result of the ray-tracing model using the experimentally extracted parameters and ray paths *a*-*e* for a 1.5 mm diameter side-drilled hole at a depth of 40 mm (left), and the equivalent experimental results (right).

Results from the simulation including the relevant experimental variables are shown in figure 2.8. These additions cause the simulated image to closely match the experimental data both in

terms of defect and back wall shape as well as amplitude with an error of 0.7 dB at the defect. For a more detailed comparison, cropped images of the main features for different defect depths are shown along with cross sections of their amplitudes in figures 2.9-2.11.

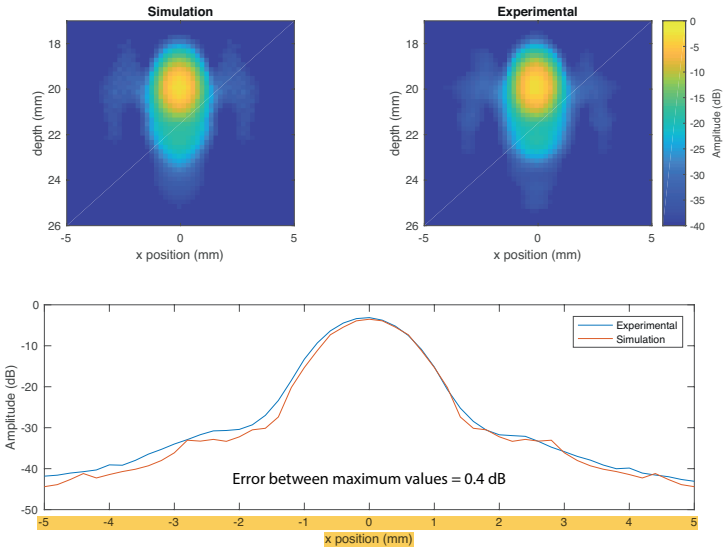

Figure 2.9: TFM images of a 1.5 mm diameter hole located at a depth of 20 mm with data produced by the ray-tracing model (top left) and by experimental measurements (top right) along with plots of a cross section of both images taken at a depth of 20mm (bottom).

These results show very close agreement between experimental results and the ray-tracing model for both the shape and amplitudes of the given defect at various depths.

Comparisons of the back walls for the same geometries are also shown in figures 2.12-2.14

In addition, these results for the back wall show that the ray-tracing method is capable of accurately predicting the amplitude drop in the back wall due to shadowing from a defect. This suggests that this method adequately captures the relevant physics required to describe the propagation of ultrasound in a homogeneous material and its interaction with defects and reflectors.

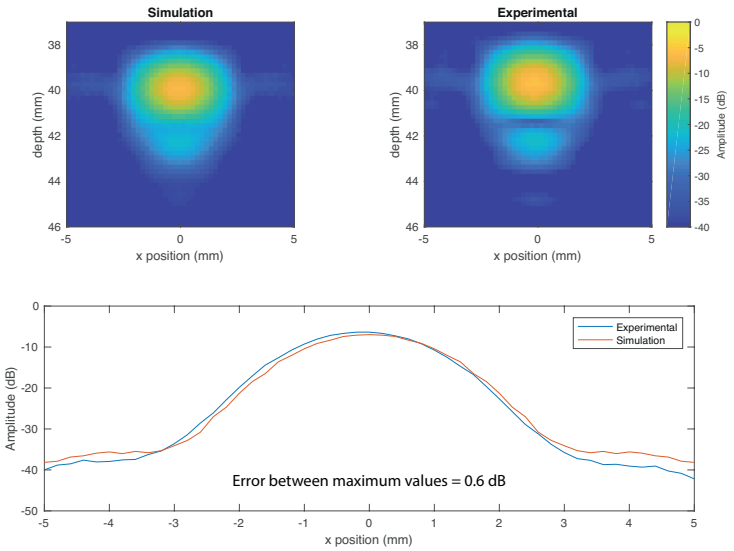

Figure 2.10: TFM images of a 1.5 mm diameter hole located at a depth of 40 mm with data produced by the ray-tracing model (top left) and by experimental measurements (top right) along with plots of a cross section of both images taken at a depth of 40mm (bottom).

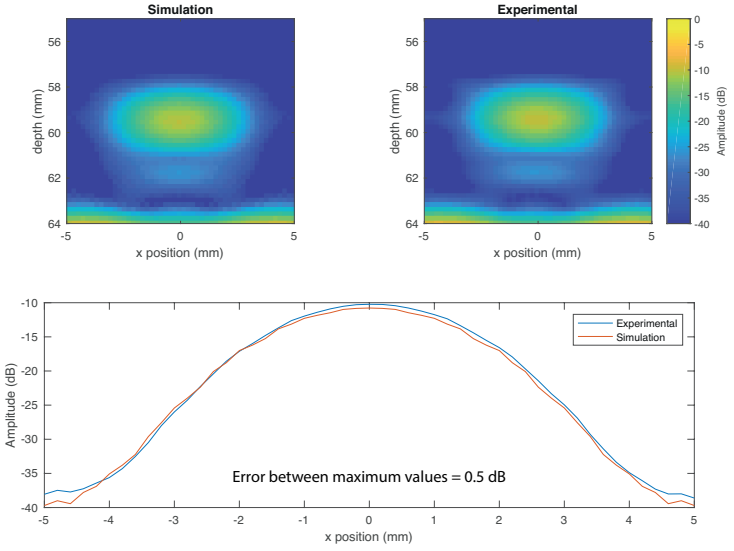

Figure 2.11: TFM images of a 1.5 mm diameter hole located at a depth of 60 mm with data produced by the ray-tracing model (top left) and by experimental measurements (top right) along with plots of a cross section of both images taken at a depth of 60mm (bottom).

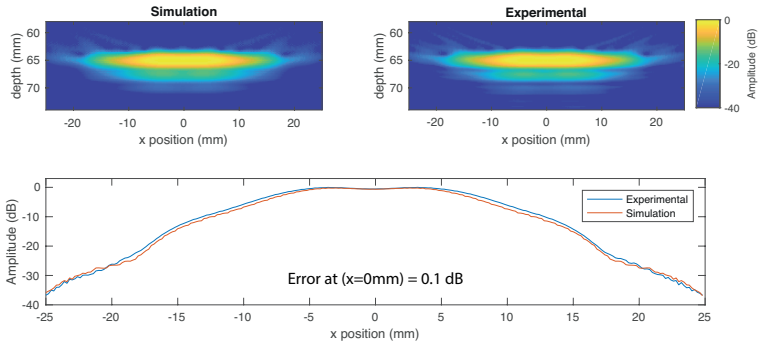

Figure 2.12: TFM images of a back wall at a depth of 65 mm, a 1.5 mm diameter hole located at a depth of 20 mm is causing shadowing effects. Data produced by the ray-tracing model (top left) and by experimental measurements (top right) along with plots of a cross section of both images taken at a depth of 65mm (bottom).

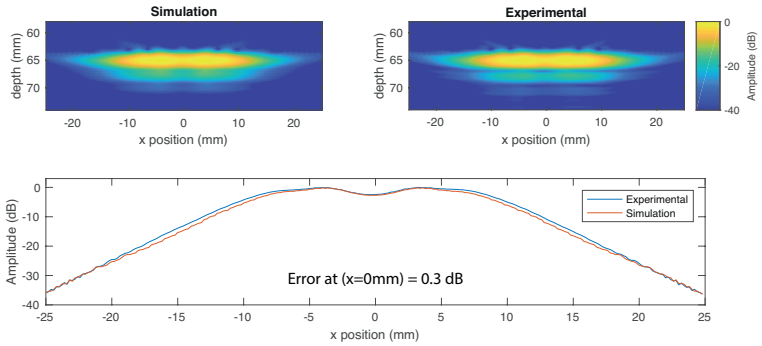

Figure 2.13: TFM images of a back wall at a depth of 65 mm, a 1.5 mm diameter hole located at a depth of 40 mm is causing shadowing effects. Data produced by the ray-tracing model (top left) and by experimental measurements (top right) along with plots of a cross section of both images taken at a depth of 65mm (bottom).

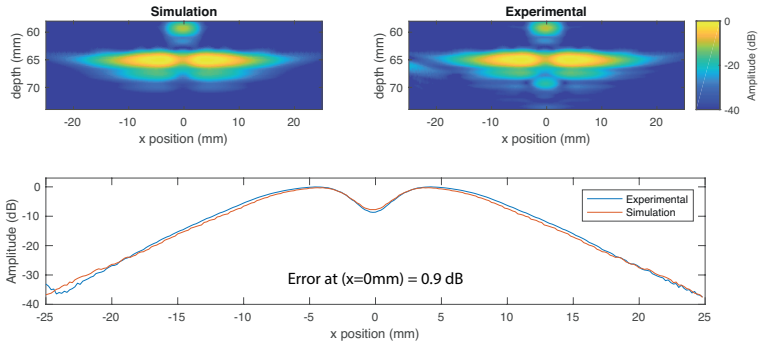

Figure 2.14: TFM images of a back wall at a depth of 65 mm, a 1.5 mm diameter hole located at a depth of 60 mm is causing shadowing effects. Data produced by the ray-tracing model (top left) and by experimental measurements (top right) along with plots of a cross section of both images taken at a depth of 65mm (bottom).

2.2.2 Modelling attenuation

The Results for the ray-tracing model show good agreement with experimental results for aluminium. However, due to its small grain size and low anisotropy, aluminium exhibits negligible attenuation and coherent noise. Many engineering materials will present both of these features when imaged using ultrasound. To ensure that the ray-tracing model is also suitable to simulate defects in these materials, it was compared to experimental results from copper samples. The typical grain size of copper is much larger than that of aluminium and they exhibit significant anisotropy. This means it is likely to be in the stochastic region in figure 1.2 as opposed to the Rayleigh regime of aluminium. The anisotropy of the crystals will cause back scatter at grain boundaries and its associated attenuation.

To be able to model an attenuative material, its frequency dependant attenuation coefficient, $\alpha(\omega)$, must be calculated. For this example, it has been done using both techniques described in section 2.1.2. For the direct contact method, three different back wall depths of 20 mm, 40 mm and 60 mm were used, this allows for the attenuation to be calculated using three different pairs of back wall measurements. The average of these measurements was then taken.

For the immersion method, only a single measurement was taken from a sample of 20 mm thickness. These results are shown in figure 2.15 and it is clear that despite only being comprised of one data set, the immersion method produces results with significantly less variation than even the mean of the contact measurements and are more consistent with the expected quadratic trend (Zhang et al., 2004) over a wider frequency range. For these reasons, the results from the immersion experiment was used for the attenuation values in this work. A quadratic fit was taken for this data and then used to calculate values of α in the ray-tracing model. Figure 2.5 shows that the frequency spectrum of the array includes frequencies outside of the range used to calculate the quadratic fit, by necessity this means that the values for α must be extrapolated outside of this range (1.5 MHz - 4.25 MHz).

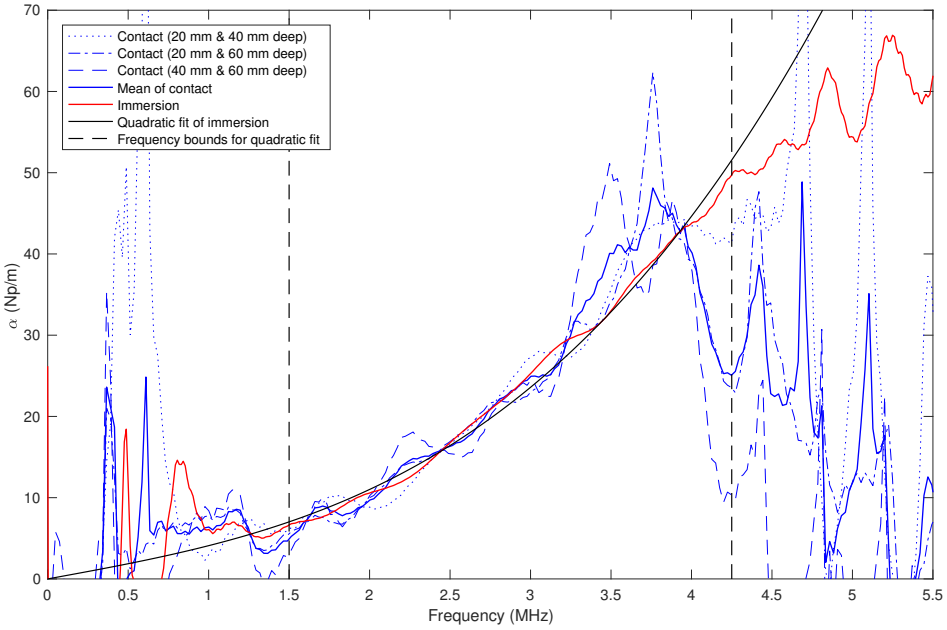

Figure 2.15: Attenuation measurements for copper using three different combinations of back wall depths, their weighted average and the quadratic fit used to determine $\alpha(\omega)$ in the ray-tracing model.

To validate these attenuation values and the ray-tracing model's ability to account for these losses accurately, a validation case similar to the one presented in section 2.2.1 was performed. A copper sample of the same geometry was used. The speed of sound for this sample was measured to be 4695 m/s.

Figure 2.16 shows a comparison between the results of the model and experimental measurements taken from the same geometry. The model does not attempt to simulate the image speckle which can be clearly seen in the experimental results, it does however accurately predict the amplitude and shape of both defects (figures 2.17-2.19) and the back wall (figures 2.20-2.22).

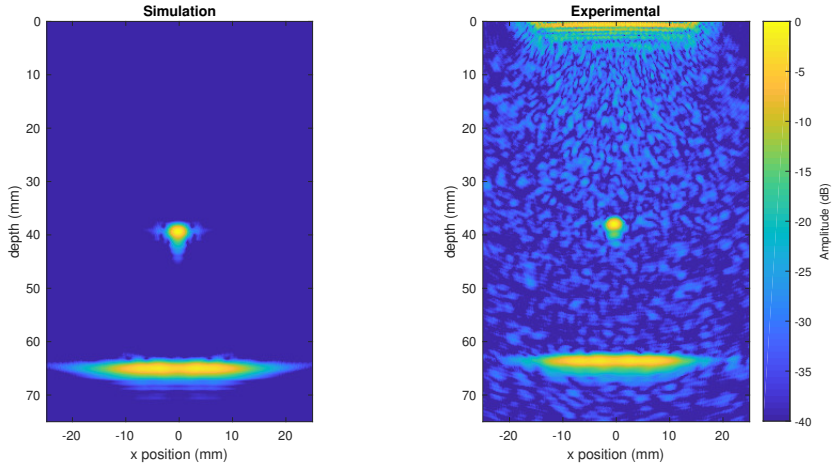

Figure 2.16: TFM images of the result of the ray-tracing model in copper for a 1.5 mm diameter side-drilled hole at a depth of 40 mm (left), and the equivalent experimental results (right).

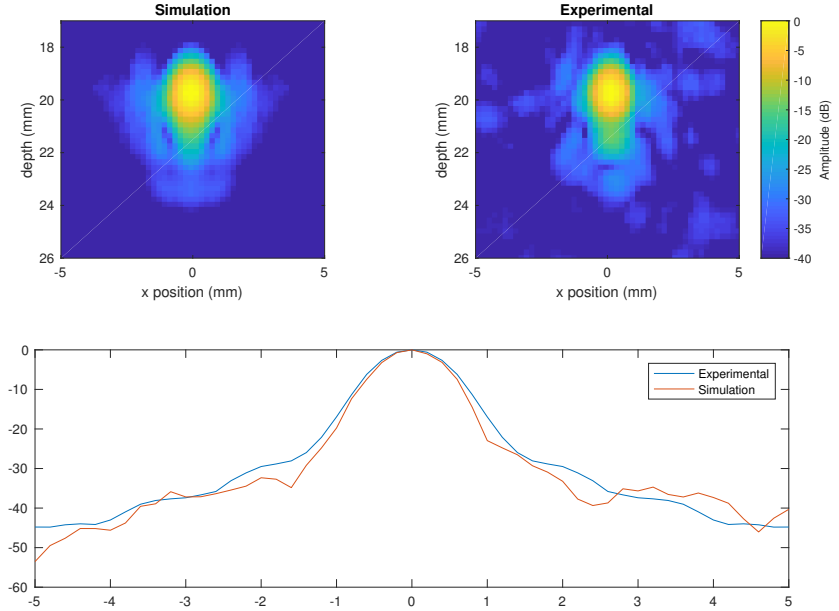

Figure 2.17: TFM images of a 1.5 mm diameter hole located at a depth of 20 mm in a copper sample with data produced by the ray-tracing model (top left) and by experimental measurements (top right) along with plots of a cross section of both images (bottom).

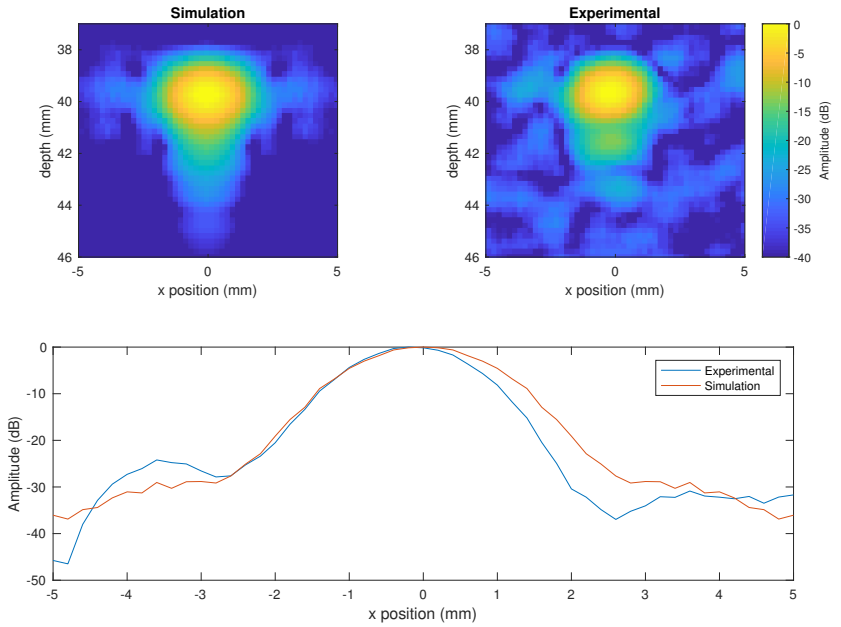

Figure 2.18: TFM images of a 1.5 mm diameter hole located at a depth of 40 mm in a copper sample with data produced by the ray-tracing model (top left) and by experimental measurements (top right) along with plots of a cross section of both images (bottom).

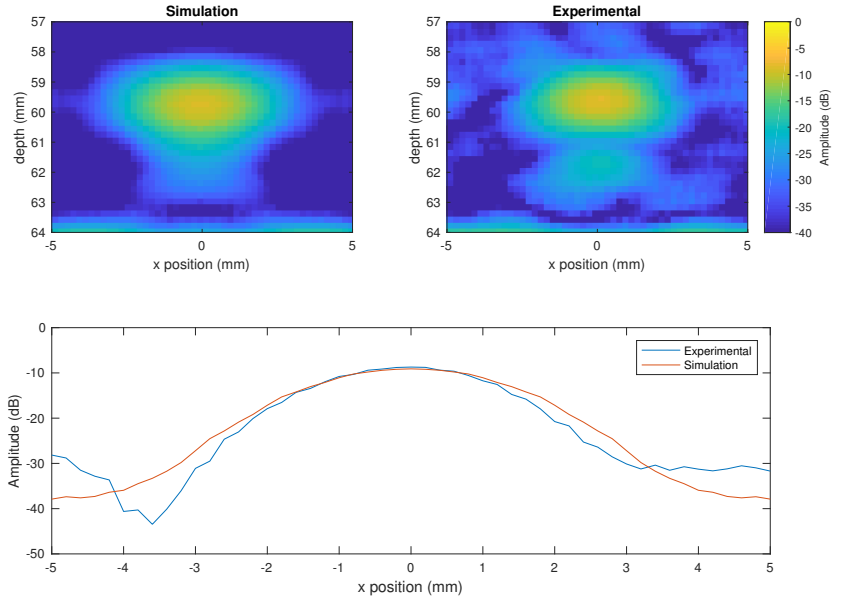

Figure 2.19: TFM images of a 1.5 mm diameter hole located at a depth of 60 mm in a copper sample with data produced by the ray-tracing model (top left) and by experimental measurements (top right) along with plots of a cross section of both images (bottom).

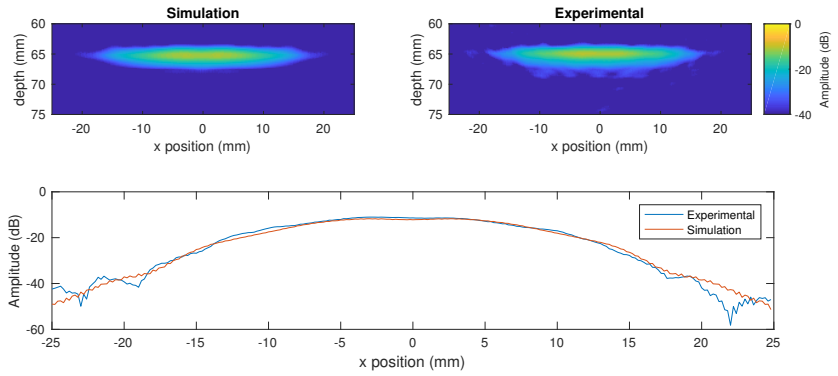

Figure 2.20: TFM images of a back wall in copper at a depth of 65 mm, a 1.5 mm diameter hole located at a depth of 20 mm is causing shadowing effects. Data produced by the ray-tracing model (top left) and by experimental measurements (top right) along with plots of a cross section of both images (bottom).

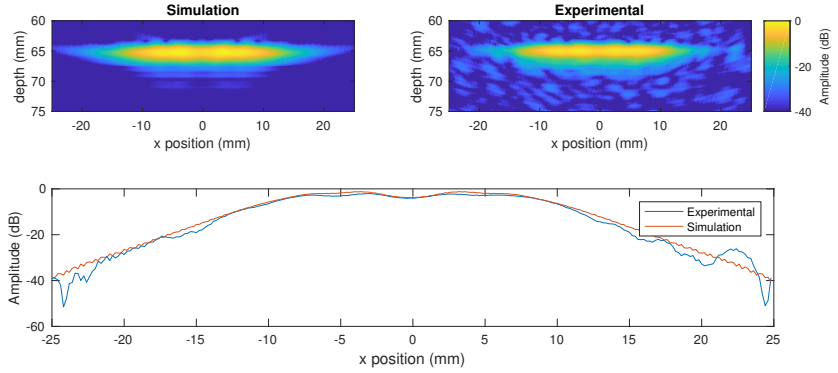

Figure 2.21: TFM images of a back wall in copper at a depth of 65 mm, a 1.5 mm diameter hole located at a depth of 40 mm is causing shadowing effects. Data produced by the ray-tracing model (top left) and by experimental measurements (top right) along with plots of a cross section of both images (bottom).

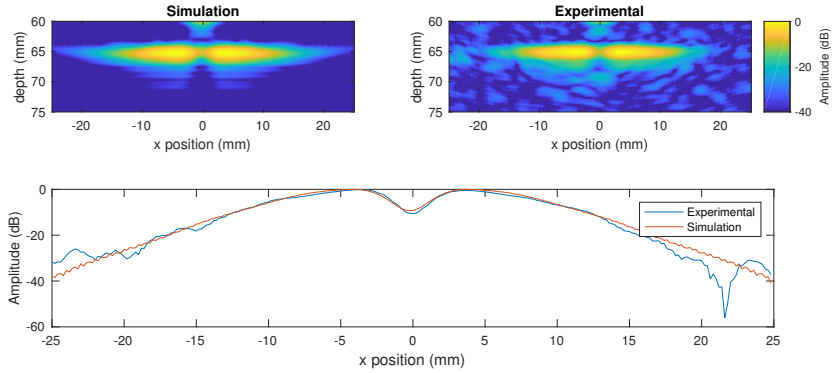

Figure 2.22: TFM images of a back wall in copper at a depth of 65 mm, a 1.5 mm diameter hole located at a depth of 60 mm is causing shadowing effects. Data produced by the ray-tracing model (top left) and by experimental measurements (top right) along with plots of a cross section of both images (bottom).

These results show that the ray-tracing model is successfully capturing the necessary physics to provide accurate simulations of ultrasonic phased array images with respect to amplitude and shape of both defects and planar reflectors. While these results only show the model's accuracy for side-drilled holes, its use of scattering matrices means that the model can be assumed to be accurate for any defect given an accurate scatting matrix is used. The side-drilled hole was used for this example as an analytical solution exists for its scattering matrix, however semi-analytical and finite element techniques exist to calculate the scattering matrix for any defect.

2.3 Limitations of 2D model

While the results presented above show good agreement between the ray-tracing model and experimental results, figure 2.23 shows that errors in the predicted amplitude begin to occur as the defect approaches the array at first becomes noticeable at a depth of 20 mm. While some of these errors, especially for a depth of 5 mm, may be caused by the extreme angles between some array elements and the defect accentuating any errors in, for example, the approximation used for the directivity function, this is also the region where near field effects due to the finite length of the array elements occur.

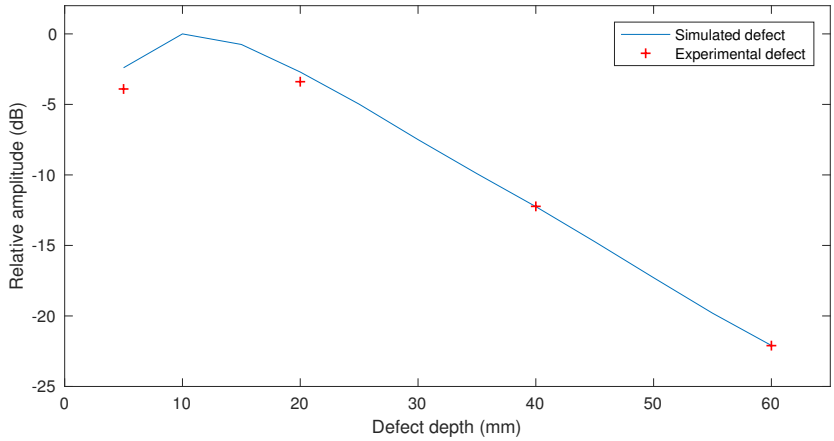

Figure 2.23: TFM image amplitude, as predicted by the ray-tracing model, versus defect depth for a 1.5 mm hole in a copper sample compared to experimental results.

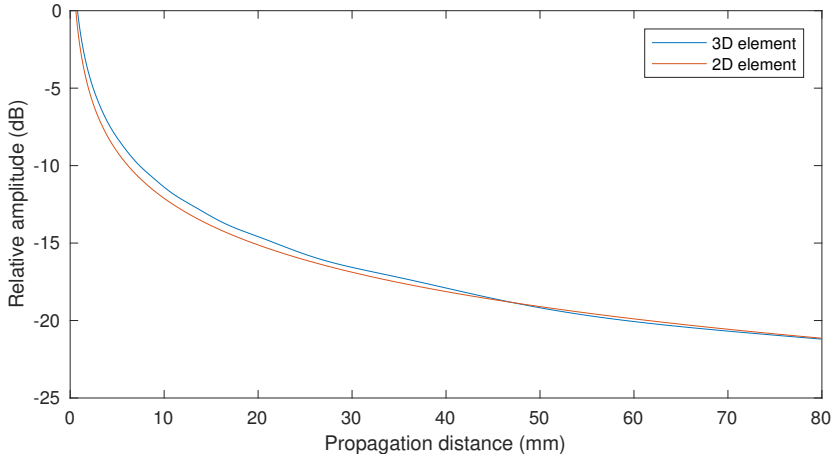

Figure 2.24: Simulated signal amplitude versus propagation distance for a 0.35 mm wide element using a 2D Huygens' model (red) and a 3D Huygens' model (blue).

Figure 2.24 shows the emitted amplitude along a line normal to the surface of the element located over its center. The results show the amplitude predicted by a Huygens' models. A 2D model assuming the element is infinitely long is compared to a 3D model which accounts for the finite length of the element. The results from the 3D model are averaged over the length of the element and the two models have been scaled so that their amplitudes match in the far field. These results show that there is a small, but not insignificant, difference in the predicted amplitude of 0.90 dB at 5 mm, 0.55 dB at 20 mm and 0.23 dB at 40 mm. By comparison, the errors shown in figure 2.23 are 1.50 dB and 0.69 dB for the 5 mm and 20 mm depth defects respectively. This suggests that the errors in the near field of the model are not due to a 2D assumption but to other factors.

Likely contributors to the discrepancies are; an increase in error due to any errors in the calculated attenuation value as a result of the defect being further from the back wall, and the extreme angles between some of the array elements and the defect when they are in close proximity exacerbating any differences between the directivity function used in the ray-tracing model and the true directivity of each of the array's elements. However, even in the extreme case of the defect being just 5 mm from the array, the error is only 1.50 dB which is relatively small in practice and means that this model is sufficiently accurate to use as a method of simulation

to provide data which can be combined with experimental results.

3 The superposition of data sets

Chapter 3 details the principles and methods of the superposition technique. The novelty of the work in the section was the basis of the publication Bloxham et al. (2016).

Assuming that one is operating in a linear regime, the ultrasonic response of an inspection can be represented as the sum of its components. For the superposition technique, we spilt the response into two components; the first is the back wall and the second is the defect response including its associated shadowing effects. As can be seen in equation 15, the result from the ray-tracing model is the sum of each of the individual components simulated, for the superposition technique, we redefine $F(\omega)$ as follows,

$$F(\omega) = F_{bw}(\omega) + F_{defect}(\omega), \tag{24}$$

where

$$F_{bw}(\omega) = F_a(\omega), \tag{25}$$

and

$$F_{defect}(\omega) = F_b(\omega) + F_c(\omega) + F_d(\omega) + F_e(\omega). \tag{26}$$

If $F_{bw}(\omega)$ is determined by experimental measurements from a defect free sample, it will include the material's associated image speckle as well as other artefacts caused by the geometry of the sample. $F_{defect}(\omega)$ can then be calculated using the ray-tracing model and the sum of these two components will be the equivalent to the simulated defect being present in the experimental sample. This is shown graphically in figure 3.1.

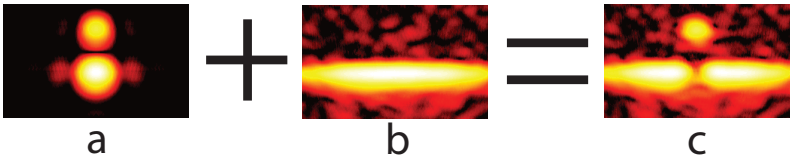

Figure 3.1: The superposition (c) of a noise-free simulated defect and shadowing effects (a) with an experimentally measured back wall (b).

While the ray tracing model does include the attenuative losses due to grain scatter, it does not model the back scattered signals that this causes. These back scattered signals are detected by the array and result in the speckle that is observed in the resultant images.

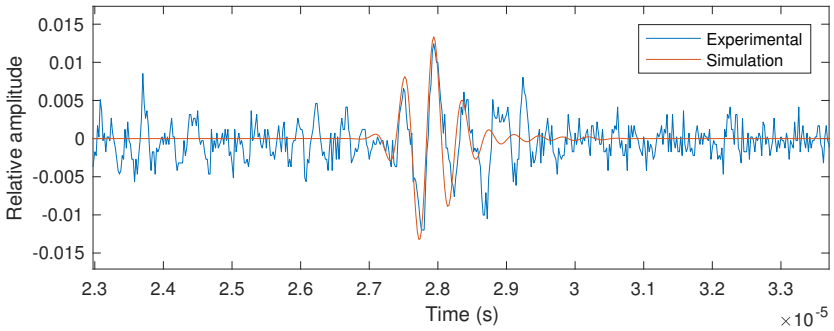

Figure 3.2: Time-traces of experimental and simulated pulse-echo responses from a single element of a back wall at a depth of 65 mm in a copper sample.

Figure 3.2 shows example pulse-echo responses for a back wall in the copper sample measured experimentally and simulated. It is clear that despite accurately predicting the amplitude and shape of the back wall signal, there is a large amount of noise in the experimental signal due to grain scatter which isn't present in the simulated signal. This means that the resultant image produced by the superposition technique will have image speckle identical to the defect-free case measured experimentally. In reality, the introduction of a defect can be expected to alter the observed speckle pattern in the region it is shadowing, but as long as the underlying statistics of this noise is not altered then this effect will not be significant.

3.1 Modelling considerations

When combining independent data sets, the result is sensitive to any errors in in the signal's shape, amplitude and phase. This is especially true for back wall shadowing effects whose is 180° out of phase with the back wall causing the two signals to interfere destructively. This phase difference is equivalent to only 10 time points for a 2.5 MHz signal sampled at 50 MHz and changes what is often one of the strongest signals present in the defect-free experimental data set (the back wall) to one of relatively low amplitude so the effect an error has on image amplitude is significant. Figure 3.3 shows the shadowing and back wall signals and their phase difference using simulated data for a 1.5 mm diameter side-drilled hole located 5 mm in front of the back wall of a 65 mm deep sample. The data shown is the pulse-echo response of an element centred over a defect. Figure 3.4 shows the maximum amplitude of the Hilbert transform of the combined response of the back wall and shadowing effect for the same signals with varying signal alignment errors. One time point is equal to $2\text{x}10^{-8}$s.

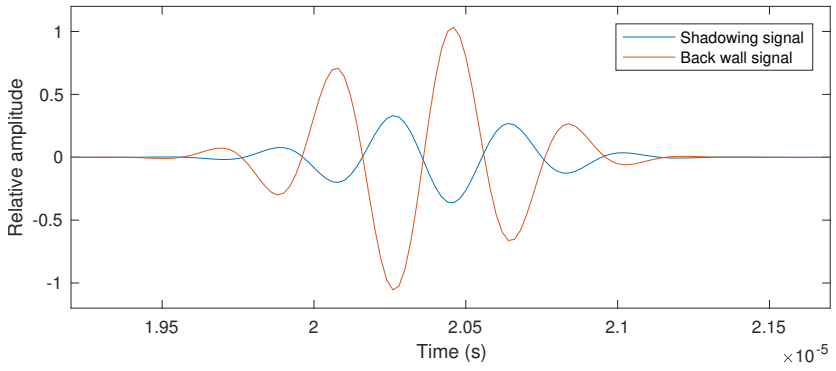

Figure 3.3: A simulated back wall signal (ray path *a*) and the simulated shadowing effects (ray paths *c*, *d* & *e*) from a 1.5 mm hole located 5 mm above the back wall.

These results show that for this example, a phase error equivalent to three time points results in a signal amplitude error of approximately 25%. In addition, any error in the shape or frequency spectrum of the signal will alter the effects of the destructive interference further reducing the models accuracy.

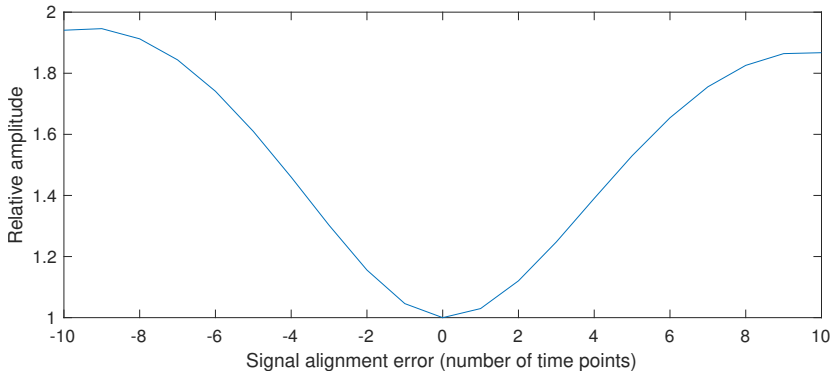

Figure 3.4: The variation in amplitude at the back wall caused by signal misalignment (equivalent to phase error) from the pulse-echo response of an element located directly above a 1.5 mm hole positioned 5 mm above the back wall.

While accurately predicting a defect's image amplitude and position is likely to be the primary use of this model, the nature of most imaging techniques means that this can be achieved with much wider tolerances on the signal's amplitude, phase and frequency spectrum than the shadowing effects. For example, a 90°phase difference in a copper sample results in a position error of less than 0.5 mm for a defect, however for a shadowing effect it would cause an amplitude error significant enough to potentially double the back wall signal amplitude. For these reasons, this work has a focus on predicting accurate shadowing effects despite it generally being of less significance than defect predictions for the practical applications of a model such as the one proposed.

3.1.1 Extracting the input signal

To achieve the required accuracy, it is therefore preferable, whenever possible, to extract the input signal for the model directly from the data set to which it is to be combined. If it is extracted from an alternative data set, additional potential sources of error will be introduced such as variations in the coupling and the temperature of both the array and sample. When extracting this signal, ideally the mean of only the pulse-echo responses will be used as this ensures that the array's input signal amplitude and frequency spectrum is captured as accurately

as possible. The nature of the inspections that this technique will be applied to however, means that this is likely to result in a very low SNR signal. Alternatively, the mean of all transmit-receive pairs of elements (approximately equivalent to the array acting as a planar source) can be used to significantly increase the SNR at the expense of losing the input signal's amplitude as well as introducing a slight shift in the frequency spectrum (2% reduction for the configuration previously discussion in this subsection). This is due to the non-pulse-echo ray paths being obliquely incident to the back wall which introduces a frequency dependence to the reflection coefficient, as well as lowering its absolute value. The increased ray path length also results in greater frequency dependant attenuation lowering its amplitude further. While attempts can be made to match the amplitude and frequency to the true input signal by back propagating the response from each transmit-receive element pair before averaging, this introduces several frequency dependant variables and was not found to provide satisfactory results.

The solution used was to use the pulse-echo response from a sub-aperture made of up of the nominal pulse-echo element and a number of that element's nearest neighbours on each side. The number of nearest-neighbours is effectively the radius of the sub-aperture measured in the number of elements. However, this is limited due to the finite size of the array. For example, if element 2 was used with 4 nearest neighbours, it would include elements 3-6 on one side, but only element 1 on the opposite side as there are no more elements available. 63 elements is equal to the full array regardless of which element is selected.

With the exception of attenuation, the variables which define the wave propagation are only frequency dependant when the wave is obliquely incident to an interface. Therefore provided that the elements used are sufficiently close and back wall sufficiently far away, the small angle approximation means that there is negligible frequency or amplitude variation between the pulse-echo response and the response received on an element in close proximity to the transmitting element. The precise number of nearest neighbours which can be used is dependant on the geometry of the array and sample as well as the material properties and array frequency.

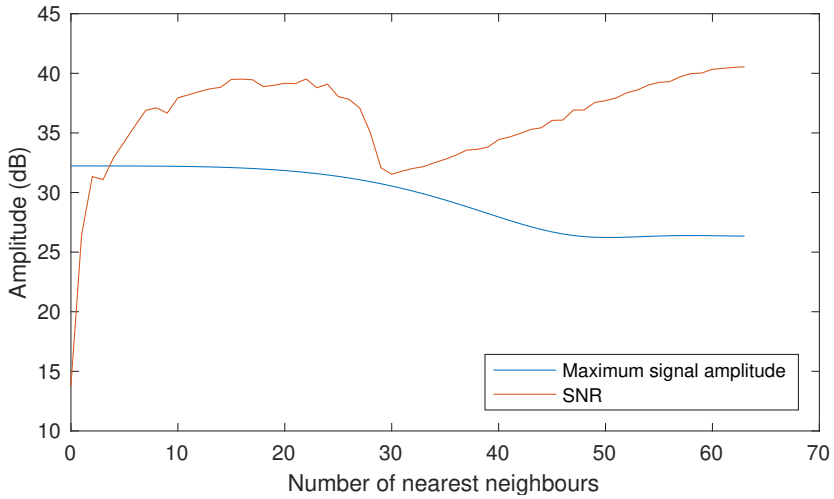

Figure 3.5: The effect using nearest neighbours has on the SNR and amplitude of the extracted input signal from experimental data.

Figure 3.5 shows how the maximum signal amplitude of a back wall for a simulated noise-free data set varies with the number of nearest neighbours used in the sub-aperture. It also shows the SNR of the response from this sub-aperture from a representative high noise sample.

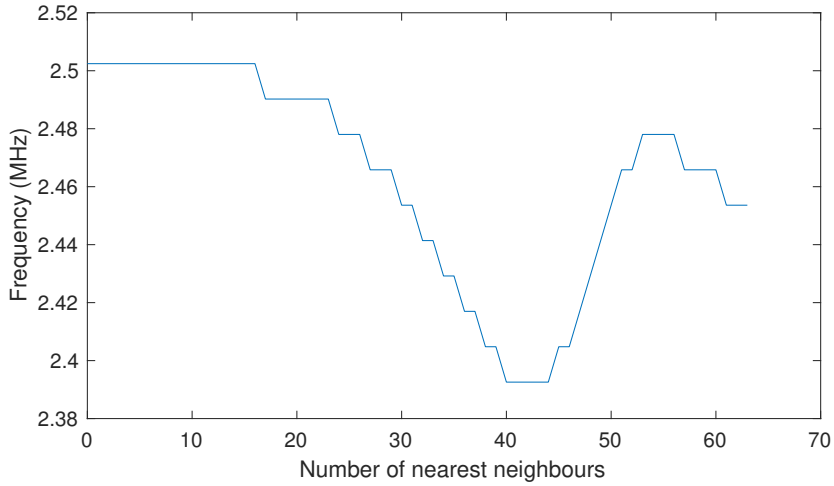

Figure 3.6: The effect nearest neighbours has on the centre frequency of the extracted input signal from experimental data.

Figure 3.6 shows how the centre frequency of the signal varies with the number of nearest neighbours used in the sub-aperture, the stair-casing effect is due to the binning nature of

FFTs. It is clear from figures 3.5 and 3.6 that using a small number of nearest neighbours has a negligible effect on the calculated input signal. While the absolute values shown in these graphs will vary with different geometries, arrays and materials, the trends they show remain valid so long as the geometry and array specifications are not significantly different. Using these results, the number of nearest neighbours to use was chosen at 3. For the case shown, this gave an improvement in SNR from 14 dB to 31 dB with a negligible penalty to the signal amplitude or frequency. While the penalty is still minimal for a much larger number of nearest neighbours in this case, it may not be for other inspections so a very conservative number was used.

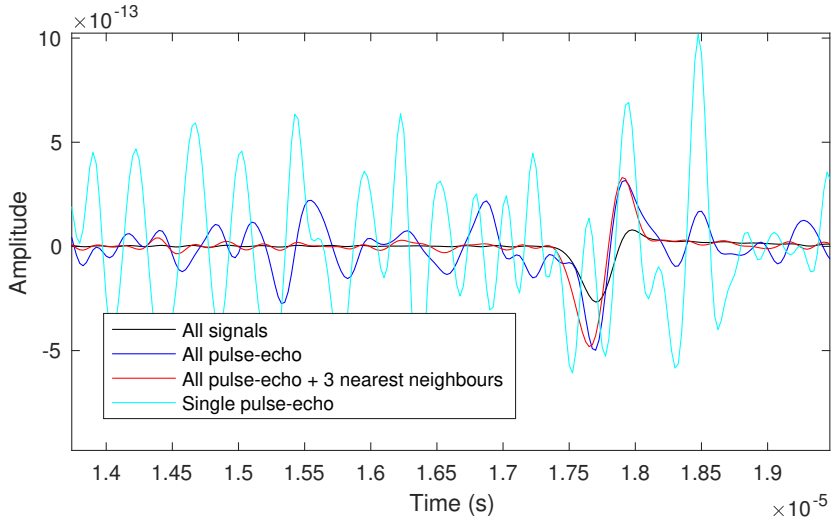

Figure 3.7: The effect using nearest neighbours has on the time-trace from which the input signal is extracted.

Figure 3.7 shows the mean of various combinations of time traces from the FMC data set used to calculate the SNR in figure 3.5. The back wall signal begins at approximately 17.5μs. The mean of the full data set shows an excellent SNR, however it also shows significant amplitude differences to the pulse-echo based means. Both the mean of only the pulse-echo signals and the response from a sub-aperture using three nearest neighbours show well matched and clearly defined back wall signals, however without using a sub-aperture, the noise amplitude of the pulse-echo average is comparable to back wall signal meaning that it would be difficult to locate without prior knowledge of its position. Also included is a single pulse-echo for reference.

Once the appropriate mean of the FMC data has been taken, the signal is windowed to isolate the back wall response from the noise in the signal. To do this, a Tukey window, $w_t(t)$, as defined in equation 27 is used.

$$w_t(t) = \begin{cases} 0, & t < t_s \\ \frac{1+cos(\frac{2\pi}{r}[t-t_s-t_p\frac{r}{2}])}{2}, & t_s \leq t < t_s + t_p\frac{r}{2} \\ 1, & t_s + t_p\frac{r}{2} \leq t < t_e - t_p\frac{r}{2} \\ \frac{1+cos(\frac{2\pi}{r}[t-t_e+t_p\frac{r}{2}])}{2}, & t_e - t_p\frac{r}{2} \leq t \leq t_e \\ 0, & t > t_e, \end{cases} \tag{27}$$

where t_s and t_e are the start and end times of the signal of interest respectively and $t_p = t_e - t_s$. This Tukey window, with parameter r, is equal to unity during the signal of interest and is tapered by a cosine wave at the extremes of this region. The length of each taper is defined as $\frac{r}{2}$ multiplied by the length of the region of interest. For this work, a value of 0.25 was used for r. Due to there being a time delay between time $t = 0$ and the input pulse being emitted, the start of the input signal will occur some time after t_s. It is important to choose a value of r such that the true start of the input signal begins after time $t_s + t_p\frac{r}{2}$ so that the shape of the input signal is not affected by the windowing function. Because of this delay introduced by the array controller, t_p must be increased by a minimum of an amount equal to this delay plus the length of one taper in the windowing function. This is to ensure that the Tukey window is equal to one over the whole length of the input signal and the tapers are only applied to noise to ensure a zero amplitude start and end to the signal. t_s is calculated from the known thickness and speed of sound of the sample and t_p must be determined from experimental measurements.

Once windowed, the signal can then be back propagated in the frequency domain to give the input signal for the ray tracing model as follows:

$$F_0(\omega) = \frac{F_{bw}(\omega)}{A_g^a A_s(\omega) T(\omega)}, \tag{28}$$

where $F_{bw}(\omega)$ is the windowed signal.

This input signal is now ready to be used in the forward ray-tracing model to simulate the defect and shadowing effects with the correct amplitude and phase to be directly summed with the defect-free experimental data set.

If it is not possible to extract the input signal from the experimental data set, it is still possible to apply this technique and achieve results of sufficient accuracy. To do this, the input signal is extracted from an experimental data set using the same array and controller and a sample ideally of the same material and, where possible, of a thickness approximately equal to the depth of the region of interest in the experimental sample. This is because by back propagating the back wall signal to use as the input signal and then forward propagating it using the same parameters, any errors in the forward model become a function of the difference in ray path lengths between the simulated path and the pulse-echo path from which the input signal was measured.

The input signal is extracted from this experimental data set in the same manor as described above, however, after being used in the ray tracing model, it will not have the correct amplitude and phase required to be summed directly with the experimental data set. To correct for this, it must first be used to simulate the defect-free experimental geometry, the results from this can then be used to calculate the scale factor and phase shift which need to be applied to make the input signal produce results which accurately match the experimental data. This corrected input signal can then be used to simulate the defect and its shadowing effects with the correct amplitude and phase to be summed directly with the experimental data set.

3.2 Superposition process

For clarity, the full process for simulating data using the superposition technique is described below.

1. Measure the material properties.
    - Attenuation coefficient.
    - Speed of sound.
    - Density.
2. Measure the inspection geometry.
3. Collect defect-free experimental FMC data set.
4. Extract back wall signal from defect-free data set if possible.
    - If not possible:
        (a) Extract back wall signal from alternative sample of the same material.
        (b) Simulate the defect-free sample's geometry.
        (c) Calculate and apply scale factor and phase shift required to match the model's result to the experimental results.
5. Simulate defect response and shadowing effects for relevant defect type and location but excluding the back wall.
6. Sum the simulated defect response with experimental defect-free data set.

The result of this process is an FMC data set representative of a known defect at a known location within a defect-free physical sample. While the method, as it is presented, has limits on the defects which can be simulated, these limits are a result of the analytical model being used and could be overcome by the use of an alternative, potentially numerical, model which does not have the same constraints.

4 Validity of superposition

This chapter makes practical use of the method described in the previous chapter and compares its results to data acquired experimentally to test its validity and accuracy as a new method of simulating ultrasonic imaging array data. Many of the following results are reproduced from data used in Bloxham et al. (2016).

The proposed method of superimposing an analytically calculated defect response with experimentally measured back wall signal is based on a single scattering assumption. While this assumption has shown to be true in scenarios where there is 'weak' scattering (Margetan et al., 1993), it is not clearly defined where this assumption ceases to be valid. The results of the technique are therefore compared to experimental results in a high noise scenario.

4.1 Experimental validation

To validate the technique experimentally, the copper sample described in section 2.2.2 was used. This sample provided back walls located at depths of 20, 40, 60 and 65 mm and 1.5 mm diameter side-drilled holes at depths of 5, 20, 40 and 60 mm in front of a back wall at a depth of 65 mm. Copper was chosen as a suitable material because by varying the array centre frequency between 2.5 MHz and 8 MHz, the attenuation and speckle varies from relatively little (14 dB drop in 6 cm thick sample) to almost complete attenuation (220 dB drop at the same thickness) in the sample used, this allows for the level of image speckle to be varied using a single sample by changing the array or filter frequency. Figure 4.1 shows TFM images for the same data set filtered using various centre frequencies with a 1 MHz half-bandwidth. A centre frequency of 3.25 MHz with a half-bandwidth of 1.75 MHz was chosen to provide an high level of image speckle while still enabling all of the defects to be clearly imaged.

Experimental measurements were made in a direct contact configuration using a 64 element, 2.5 MHz centre frequency array described in table 2.1 and were compared to results simulated

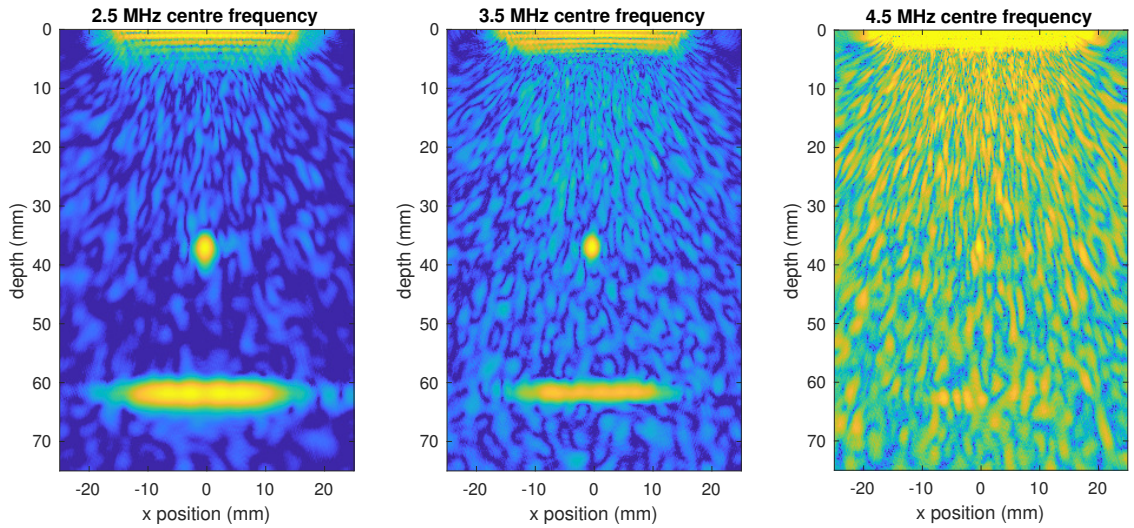

Figure 4.1: TFM images showing how the level of speckle and SNR of the main features varies with filter centre frequency.

using the superposition technique for each of the reflectors in the sample. The attenuation coefficient, as calculated in 2.2.2, was used and the defect-free experimental measurements required for the superposition technique were extracted from the same sample. TFM images of the data sets were used as the means of comparison.

Figures 4.2-4.5 show a comparison between TFM images of the simulated data and the experimental data defect depths of 5, 20, 40 and 60 mm. The images are normalised to the brightest pixel in the image which causes the effect that any error in the defect amplitude manifests as a DC offset in the rest of the image. By looking at the back wall and speckle amplitudes in figures 4.2 and 4.3, there is a noticeable difference in amplitudes between the model and experimental data. The difference in back wall amplitudes in figure 4.2 is 1.28 dB and 1.08 dB in figure 4.3. While it is difficult to identify the exact causes of these errors, it is unlikely to be due to the defects superposition with image speckle due to the high SNR of these images. The amplitude of the image speckle for both cases is approximately -32 dB, the most extreme effect this could have on a signal of the defects amplitude is 0.25 dB.

The likely source for these errors is a combination of inaccuracies in the model's parameters

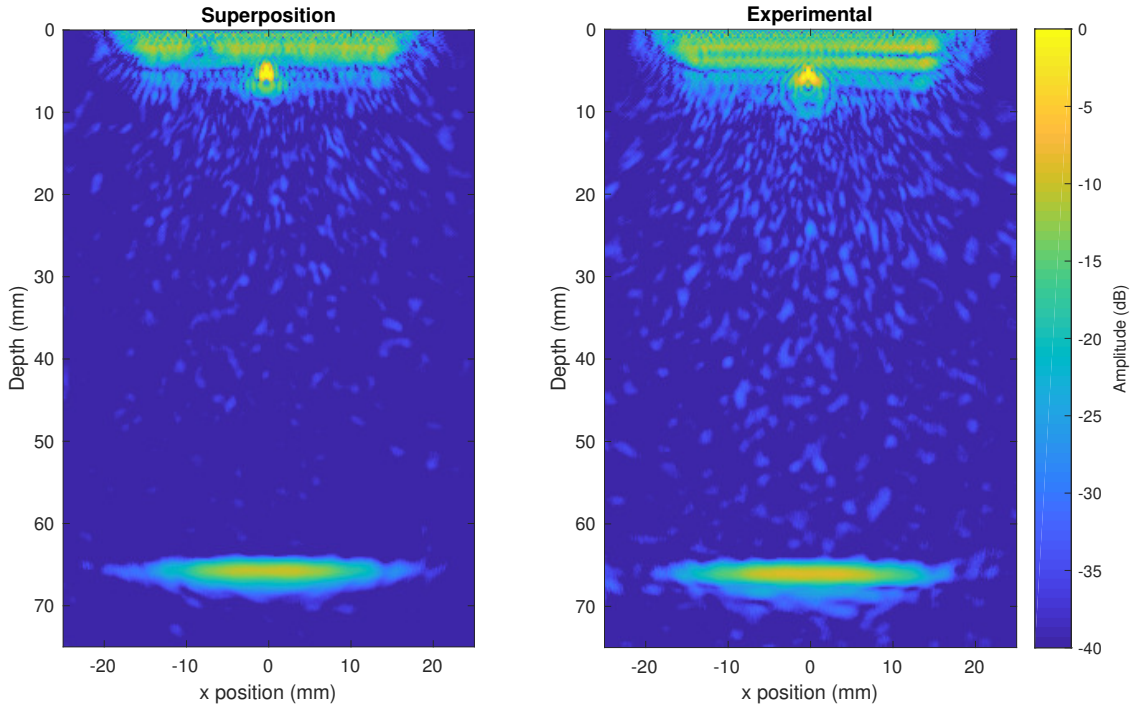

Figure 4.2: TFM images for a 1.5 mm (0.8 λ) diameter hole located 5 mm from the array and 60 mm from the back wall simulated using the superposition technique (left) and experimental results (right). The array used has a nominal centre frequency of 2.5 MHz and has been filtered at a frequency of 3.25 with a half bandwidth of 1.75 MHz.

and near-field effects caused by the array element's finite length. As discussed in the previous chapter, due to back propagating the back wall signal to use as an input signal, and then forward propagating it using the same parameters, any errors which would usually scale with propagation distance, now scale with the difference in propagation distance between the ray path in question and the back wall pulse-echo ray path distance. Both of the defects in question are some distance from the back wall with significantly shorter ray paths. This means that the back wall signal is being amplified using extrapolated attenuation values at the higher frequencies. In addition, for the defect at a depth of 5 mm, there are large angles between some array elements and the defect, this will accentuate any errors in the approximation used for the directivity function. However, these errors are all related to the modelling method being used to simulate the defect response and are not inherent errors of the superposition technique.

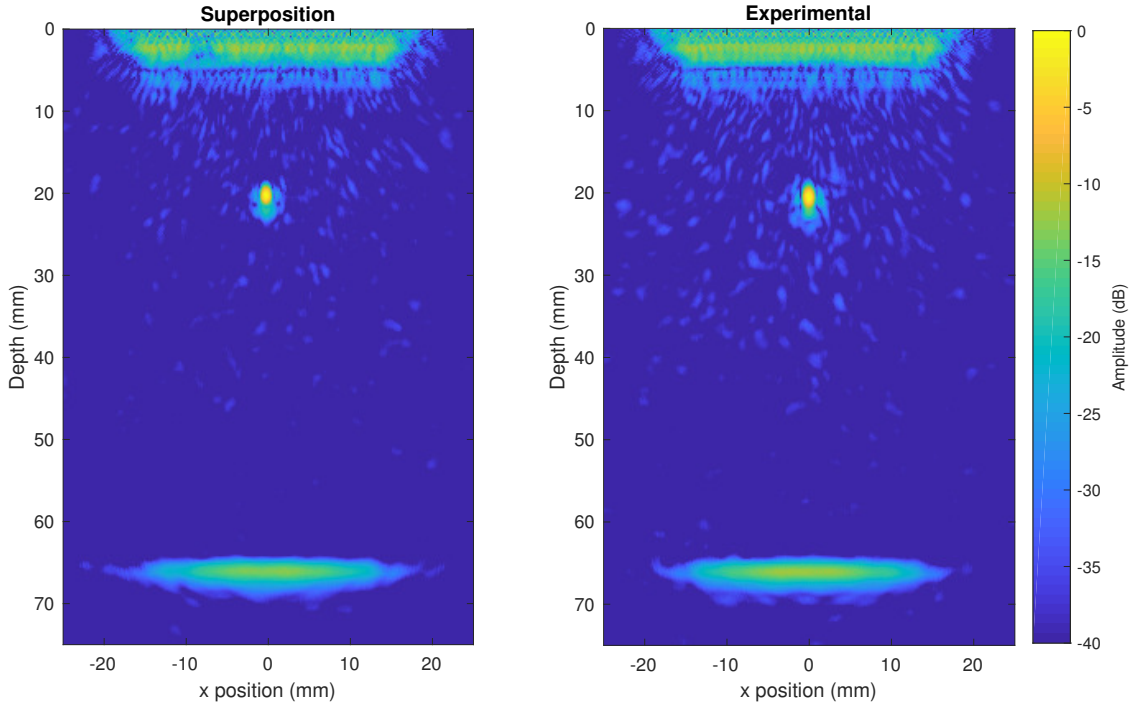

Figure 4.3: TFM images for a 1.5 mm (0.8 λ) diameter hole located 20 mm from the array and 40 mm from the back wall simulated using the superposition technique (left) and experimental results (right). The array used has a nominal centre frequency of 2.5 MHz and has been filtered at a frequency of 3.25 with a half bandwidth of 1.75 MHz.

Figures 4.4 and 4.5 show excellent visual agreement in terms of defect amplitude and shape, and the back wall amplitude and shadowing effects between the superposition technique and the experimental results shown. The difference in back wall amplitudes shown in figure 4.4 is 0.16 dB and 0.67 dB between the defects in figure 4.5. Defects at these depths are outside the region of any significant near field effects caused by the element's finite length and any potential errors introduced by inaccurate attenuation measurements will be reduced. For these reasons, these defects can be considered a better test of the superposition technique as the errors associated with the modelling technique are greatly reduced.

The results presented so far have all had the array positioned directly over the defect, this is an idealistic scenario and while many defects will be imaged in this way once they have been located, it is also important that the model produces accurate results for defects which are not

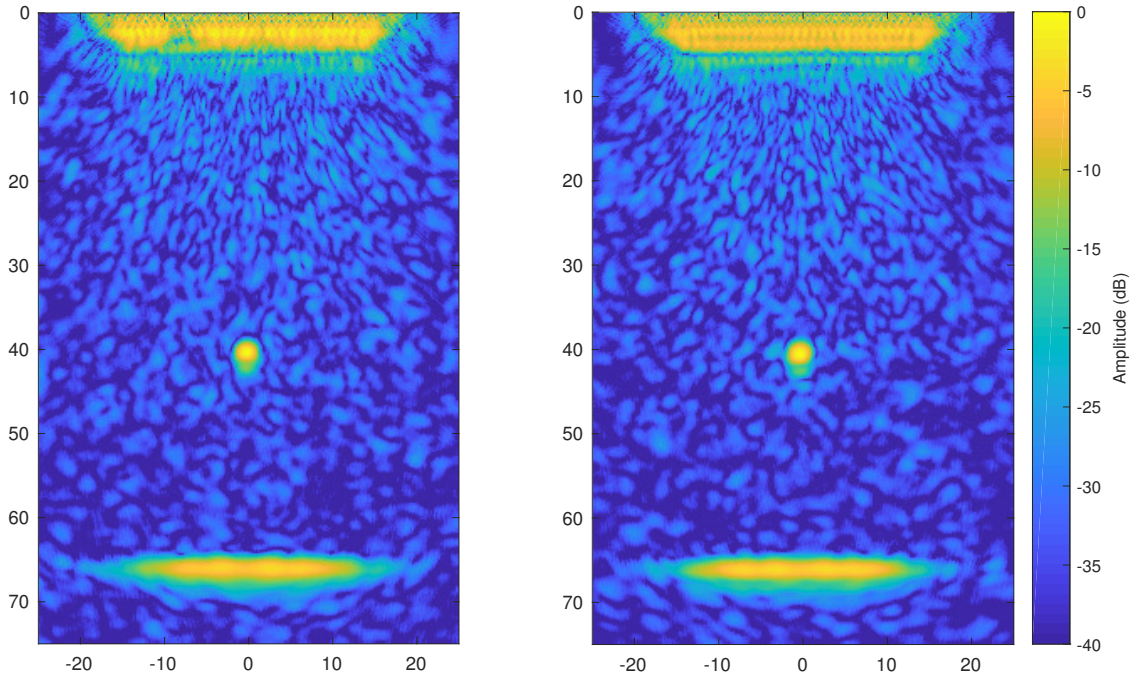

Figure 4.4: TFM images for a 1.5 mm (0.8 λ) diameter hole located 40 mm from the array and 25mm from the back wall simulated using the superposition technique (left) and experimental results (right). The array used has a nominal centre frequency of 2.5 MHz and has been filtered at a frequency of 3.25 with a half bandwidth of 1.75 MHz.

along the centre axis of the array. Figure 4.6 shows results for a 1.5 mm side-drilled hole at a depth of 40 mm and approximately 25 mm away from the central axis of the array in the x-dimension. Figure 4.7 shows similar results but at a depth of 60 mm and 20 mm off-axis. These simulations produced results of with a similar accuracy to the previous results suggesting there is no loss of accuracy with off-axis defects. The results shown in 4.6 gave a 0.44 dB difference in defect amplitude between the model and experimental results while there was a 0.12 dB error for the results presented in 4.7.

Due to the random nature of noise present in this data, it can expected that there will be some variation in amplitude between any nominally identical data sets, whether measured experimentally or simulated. Because of this, the superposition model was run with multiple experimental defect-free data sets to analyse how the range of results produced by the model compared with the experimental data set containing the defect. This was only done for defects

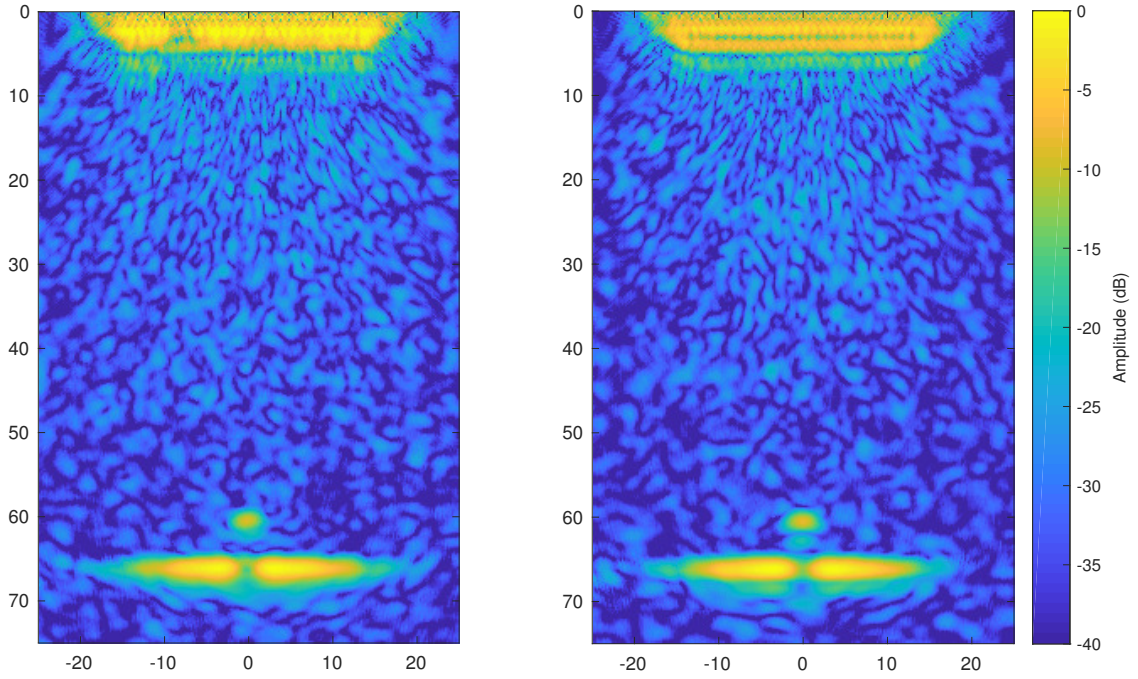

Figure 4.5: TFM images for a 1.5 mm (0.8 λ) diameter hole located 60 mm from the array and 5 mm from the back wall simulated using the superposition technique (left) and experimental results (right). The array used has a nominal centre frequency of 2.5 MHz and has been filtered at a frequency of 3.25 with a half bandwidth of 1.75 MHz.

at depths of 40 mm and 60 mm to remove any uncertainty associated errors in the ray-tracing model in the near field of the array.

Figure 4.8 shows the results of the superposition technique calculated using 20 independent defect-free data sets as well as a single experimental data set for a 1.5 mm side-drilled hole located at a depth of 40 mm. The results shown is a cross section of the TFM image taken at both the centre of the defect and the centre of the back wall. Figure 4.9 shows the same results for the same defect located at a depth of 60 mm.

The images used for the data presented in figures 4.8 and 4.9 are normalised to the point of maximum amplitude in that image. The absolute amplitude of this point is subject to variations due to noise, as this point is always equal to 0 dB in the image, these variations have the effect of changing the amplitude at every other point in the image by an equal amount, on a linear

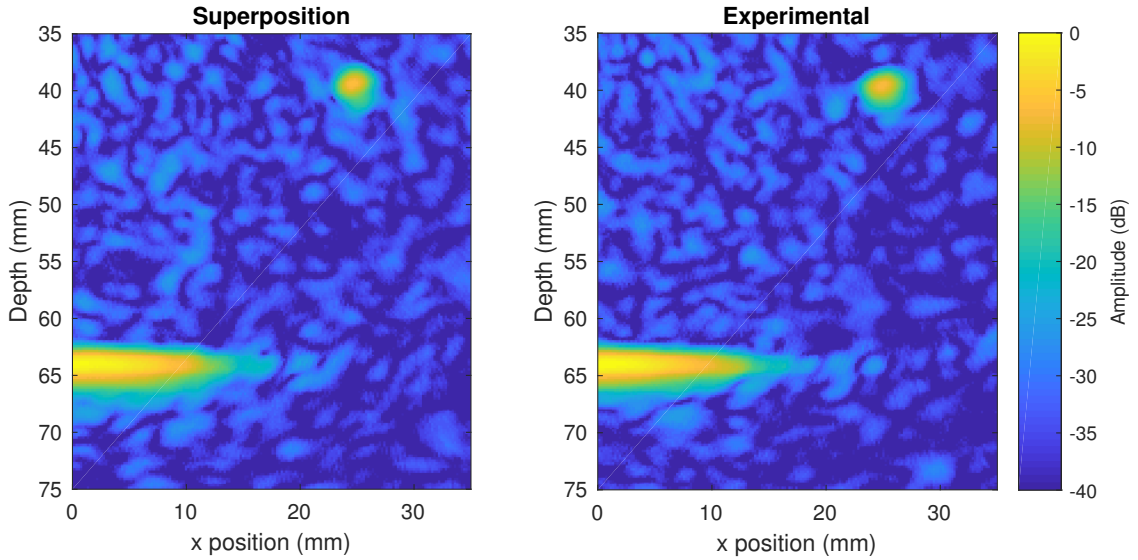

Figure 4.6: TFM images for a 1.5 mm (0.8 λ) diameter hole located at a depth of 40 mm and approximately 25 mm offset from the centre of the array simulated using the superposition technique (left) and experimental results (right). The array used has a nominal centre frequency of 2.5 MHz and has been filtered at a frequency of 3.25 with a half bandwidth of 1.75 MHz.

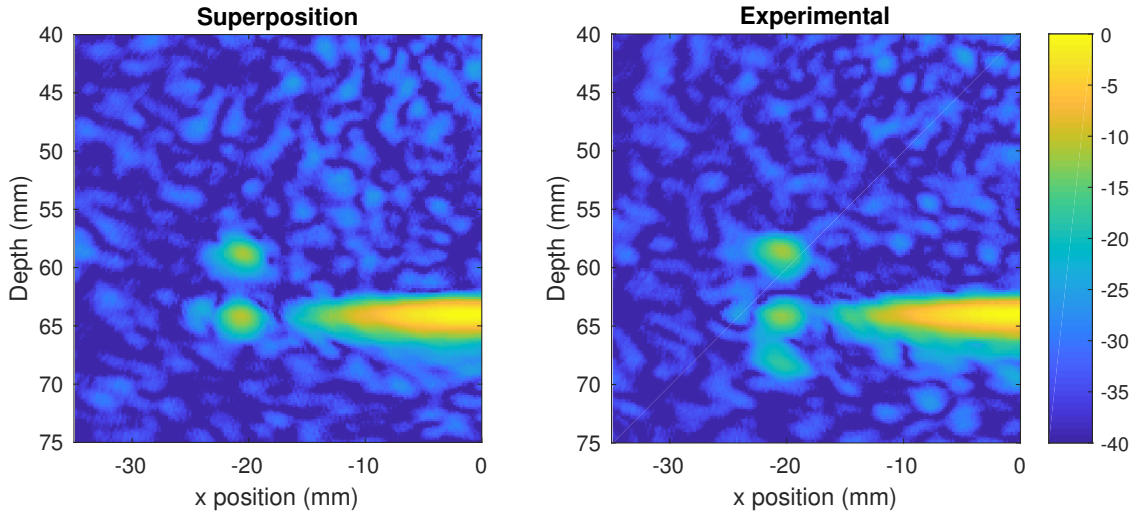

Figure 4.7: TFM images for a 1.5 mm (0.8 λ) diameter hole located at a depth of 60 mm and approximately 20 mm offset from the centre of the array simulated using the superposition technique (left) and experimental results (right). The array used has a nominal centre frequency of 2.5 MHz and has been filtered at a frequency of 3.25 with a half bandwidth of 1.75 MHz.

scale. This effect is best seen in figure 4.8a. This shows very good agreement for the defect shape between approximately x-positions -2 mm and 2 mm (outside of this range the response

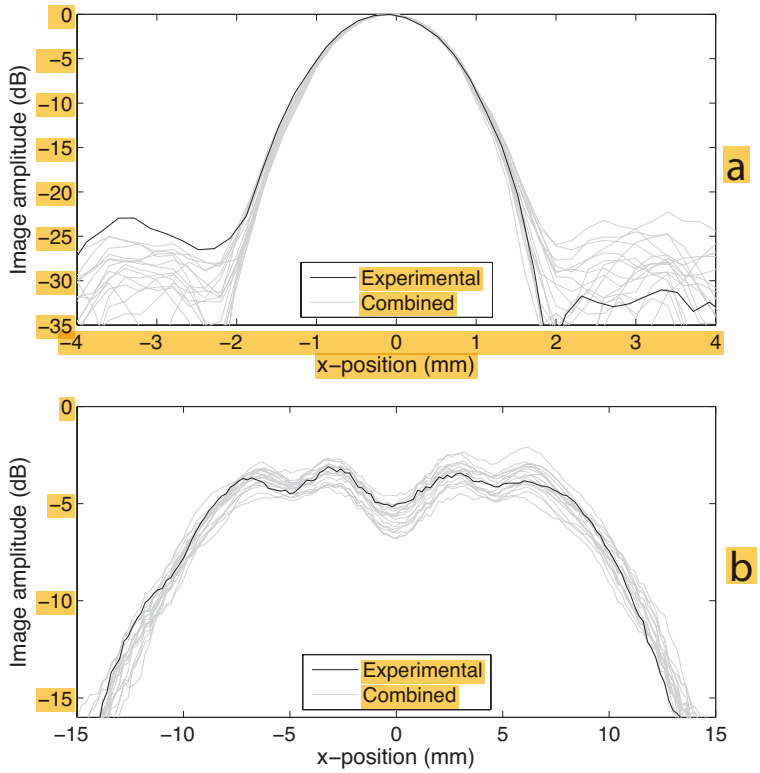

Figure 4.8: Image amplitude cross sections of a 1.5 mm (0.8 λ) diameter hole located 25 mm from the back wall and 40 mm from the array: (a) at the depth of the hole; (b) at the depth of the back wall. Experimental measurements from a sample containing a physical hole are shown in black and results from multiple defect-free experimental measurements combined with modelled data from a hole are shown in grey.

is dominated by noise so large variations are expected) and identical maximum amplitudes of 0 dB as, for this case, the rest of the image is normalised to the centre of this defect. The model results for the back wall amplitudes shown in figure 4.8b show variations covering a range of 1.5 dB, this is due to the compounded effects of the noise associated with the point of maximum amplitude (uniform linear shift for whole back wall) and noise local to the back wall (different for each point in the image). The experimental result shown in the same figure has a similar shape and amplitude within the range of those predicted by the model suggesting the model

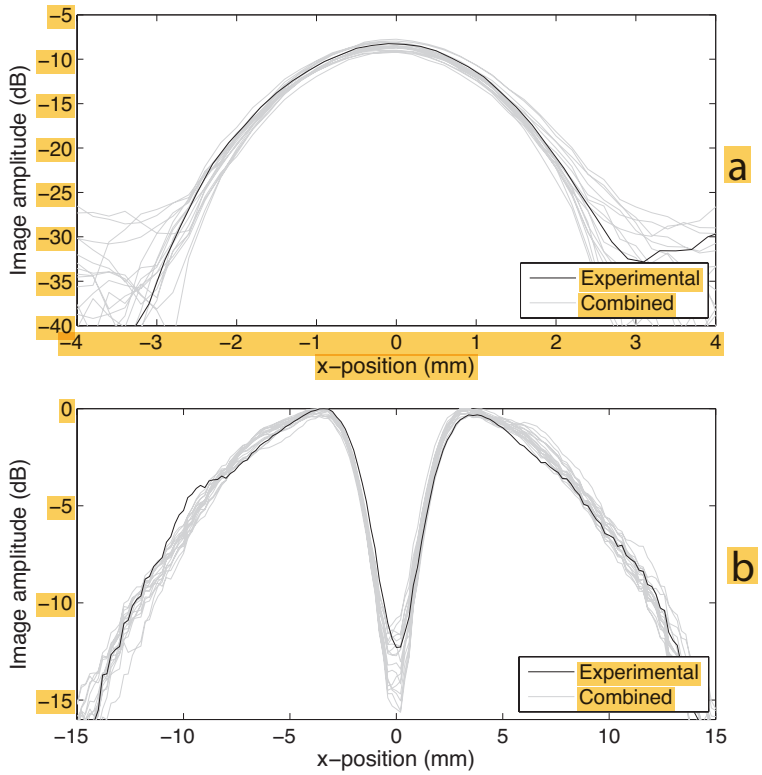

Figure 4.9: Image amplitude cross sections of a 1.5 mm (0.8 λ) diameter hole located 5 mm from the back wall and 60 mm from the array: (a) at the depth of the hole; (b) at the depth of the back wall. Experimental measurements from a sample containing a physical hole are shown in black and results from multiple defect-free experimental measurements combined with modelled data from a hole are shown in grey.

provides realistic results.

Figure 4.9 presents similar results for a defect located 60 mm away from the array and 5 mm in front of the back wall. The two major differences between this inspection and the one presented in figure 4.8 are that the defect has a lower SNR (approximately 15 dB) and the multiple scattering effects which cause the back wall shadowing are much stronger. The lower SNR of the defect means that the linearly random fluctuations due to noise can be expected to have a greater influence on the defect amplitude on a log scale. The observed variation was

1.8 dB. There are also large variations seen in the back wall amplitude at its centre where the shadowing effects occur. This is likely due to the sensitivity of interference between the back wall and its shadowing effects, on which noise may have an effect more significant than would be expected at any other point in the image.

These results have shown that the superposition technique is capable of accurately simulating defect responses in a noisy sample by combining the defect-free experimental response of the sample with that of an analytically calculated defect. Defects over the full depth of the sample were predicted with reasonable accuracy, differences of up to 1.3 dB were seen between the simulated and experimental results at defect depths of 5 mm and 20 mm. However the results presented in figure 2.23 raise questions about the ray-tracing model's suitability at these depths. At depths for which the ray-tracing model has been shown to be accurate, its superposition with experimental data was found, on average, to give high levels of accuracy. While, for the 20 different realisations of noise used, the image amplitudes varied by 1.5 dB and 1.8 dB for the 40 mm and 60 mm deep defects respectively, their average amplitude errors were just 0.3 dB in both cases. Without further data sets from samples containing true defects, it is not possible to determine if the spread of values predicted by the superposition model is caused by an error in the model or if it is representative of the real variations one could expect in experimental data.

5 Limits of validity

The previous chapter showed that the superposition technique is capable of providing results with a high level of accuracy, however, it also predicted that the results would vary for nominally identical geometries depending on the grain structure. The limited range of available experimental data meant that determining if the range of predicted results was representative of reality or not was not possible. Further data sets with true defects present are needed to study this variation so finite element techniques were used to create this data. This chapter's novel work is also presented in Bloxham et al. (2018).

In addition to the varying range of results seen previously, this technique also requires the assumption that the superposition of the response with a defect-free sample with an analytically calculated defect response is identical to the response of the same sample containing the same defect. The experimental results suggested empirically that this was a valid assumption, however, in reality, the addition of a defect will include shadowing effects on grains in the region behind the defect which are not accounted for in the model. It must therefore be determined if this change is of significance. Due to the random nature of this noise, the absolute changes in the image speckle which will occur, are not of significance provided that the underlying statistics remain unchanged.

To study both of these effects, it is necessary to collect FMC data sets from a sample with and without a defect present while maintaining the same grain structure. The change in noise in the region which is shadowed from the array by the defect can then be examined. While this is theoretically achievable using experimental methods by taking measurements before and after a defect has been introduced, it would require maintaining the precise array location as well matching all other environmental factors between measurements which would be difficult to achieve practically. The machining required to add the defect would also alter the local metallurgy adding further uncertainty to the results. Numerical methods would also facilitate the creation of a much larger and varied data pool without introducing the additional uncertainties

associated with experimental methods hence the decision to use a finite element model.

5.1 FE modelling

FE models have been used extensively to model ultrasonic propagation and have been shown to give a high degree of accuracy (Lord et al., 1990; Moser et al., 1999; Drozdz, 2008). By modelling individual grains in the sample, it is also possible to accurately simulate grain scatter (Van Pamel et al., 2017). These models can then be run with and without a defect while maintaining an otherwise identical grain structure to better understand the effect the addition of a defect has on image speckle.

In addition, the experimental validation case was only able to compare the model's results to one data set for each defect location and while the simulated results suggested that the defect and back wall image amplitudes would vary for different realisations of noise, this could not be verified with the experimental data available.

The defect chosen for the experimental validation also gave results with a relatively high SNR. This was suitable for a general validation case, however, if this technique is to be used to simulate defects at the limit of detectability, it must be shown to be accurate at this limit which was not explicitly achieved by the experimental validation case.

The use of an FE model would allow for both multiple realisations of noise for each defect as well as wider range of defect SNRs to be simulated.

5.1.1 Grain modelling

For the FE model to produce results representative of a real noisy material, the grain structure used within the model must be realistic within the constraints of a 2D model. The grain boundaries seen in a 2D slice of a 3D material are not a true representation of the distribution of grain

sizes in the material as many of them will be sliced through a plane which does not expose their characteristic dimensions. However, the purpose of this FE model is not to accurately simulate a realistic material but rather to accurately study wave propagation in a typical high noise material. Using Voronoi diagrams (Aurenhammer, 1991) is a common technique for simulating grain structures in polycrystalline materials (Ghosh et al., 1997; Kocks et al., 2000) including for the purposes of modelling ultrasonic propagation within the material (Van Pamel et al., 2017; Ghoshal and Turner, 2009). To create a randomised map of grain boundaries using this method, initially a grid of equally spaced nodes is created with a node spacing equal to the required mean grain size. Each seed is then shifted a random amount in each dimension following a zero-mean Gaussian distribution with a standard deviation equal to the defined spread parameter. To create a Voronoi diagram from these nodes, a convex polygon is drawn surrounding each node defining the region of the diagram which is closest to the enclosed node. An example diagram with the same grain size distribution as used in the model can be seen in figure 5.1.

Once the grain geometry has been defined, each grain can be given a random orientation in 3D and then the relevant material properties can be applied.

For the results presented here, the following grain and material parameters were used (Green and Green, 1973):

Property	Value
Mean grain size	100 µm
Grain spread parameter	200 µm
E_{11}	168.6 GPa
E_{12}	121.4 GPa
E_{44}	75.4 GPa
Anisotropy factor	3.19
ρ	8960 kg/m^3

Table 5.1: Material and grain properties including the calculated anisotropy factor (Zener and Siegel, 1949).

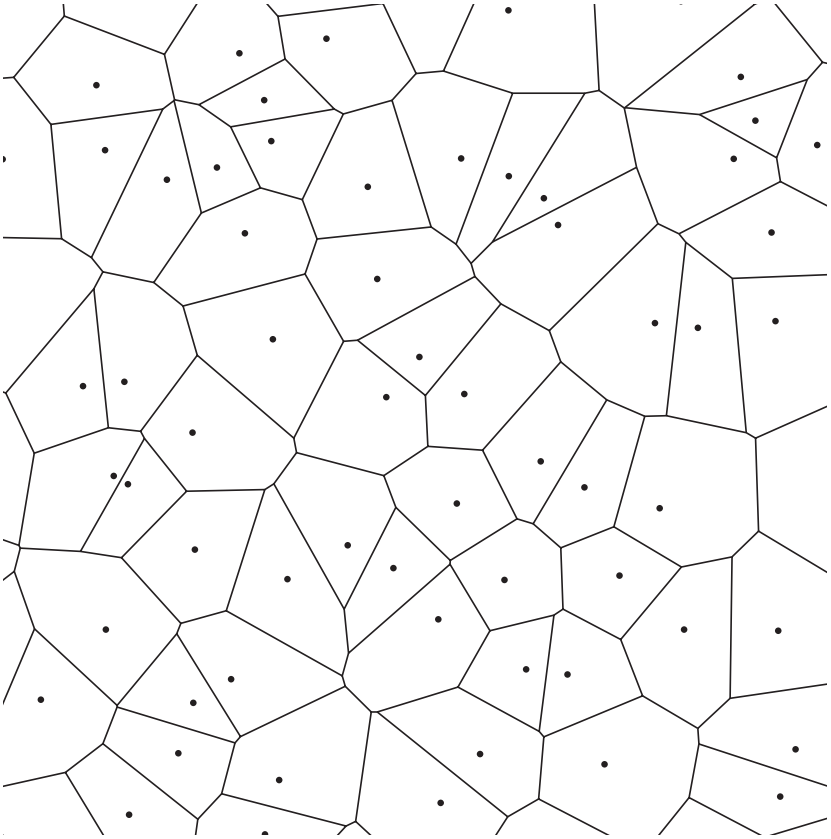

Figure 5.1: An example Voronoi diagram used to simulate the grain boundaries of a polycrystalline material.

5.1.2 Meshing

There were two main approaches considered for meshing the grain geometry for the FE model, structured and unstructured meshes.

In a structured mesh, the model's geometry is modified to fit a predefined mesh of elements, this is usually of the form of a regular grid. The effect this would have on the given model geometry is to modify the straight edges of the grain boundaries into a sawtooth shape so that the grain boundary would be coincident with a continuous line of connected mesh elements. While this modification means the geometry is no longer representative of a realistic grain structure, provided that the elements are sufficiently small, the variations in the grain boundaries will be

very small relative to the propagating wavelength meaning that it will have a negligible effect on the ultrasonic response.

In an unstructured mesh, the elements are matched to the model's geometry. This allows for even complex geometries to be modelled accurately, however, it requires undesirably small elements to be able to achieve this. As the maximum stable time step of the solver is determined by the smallest element size, this results in the simulation running impractically slowly. An example of both structured and unstructured meshes is shown in figure 5.2. Because of this, and due to the fact that it is not strictly necessary to simulate the exact grain structure produced by the Voronoi diagram, just one which is representative of a realistic material, structured meshes were used in this work.

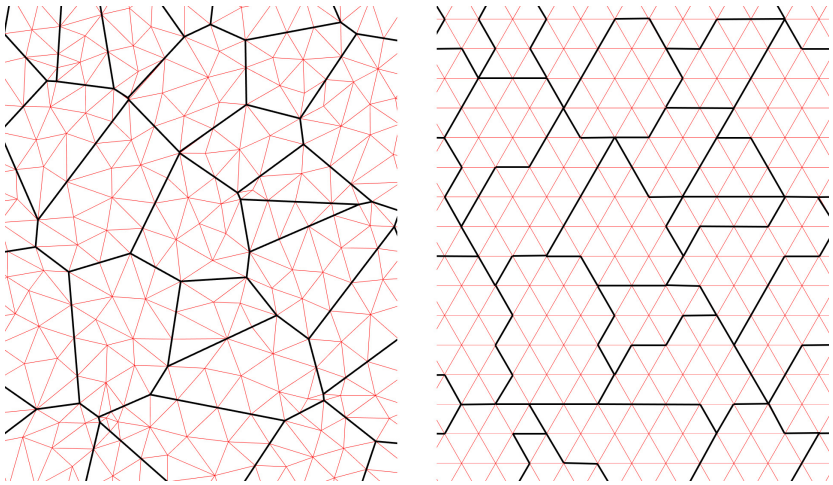

Figure 5.2: Comparison between an unstructured mesh (left) and structured mesh (right). Mesh element boundaries are shown in red while the grain boundaries are shown in black. The element size has been exaggerated for clarity.

Triangular elements with an edge length of 30 µm were used in the mesh, this equates to approximately 60 elements per wavelength and an average of 26 elements per grain. An example of a true mesh used is seen in figure 5.3.

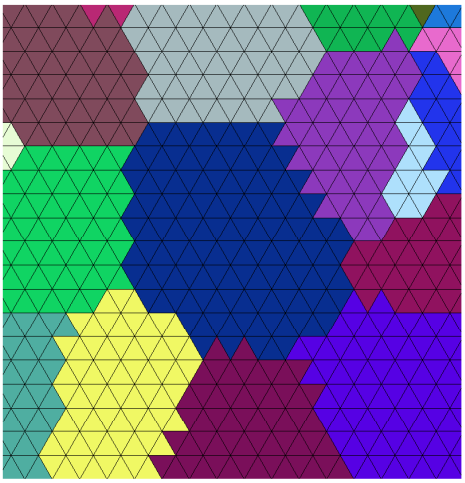

Figure 5.3: Example of the stair-casing effect at the true mesh density.

5.1.3 The finite element model

The continued advancement in computing hardware has significantly reduced the computing time required to perform full time domain FE simulations of ultrasonic wave propagation for useful sample volumes. The most significant development in recent years has been the utilisation of the parallel process capabilities of Graphics Processing Units (GPUs), the use of which has been shown to reduce the processing time by 1-2 orders of magnitude (Huthwaite, 2014). Pogo (www.pogo-fea.com), an open-source FE solver, takes advantage of this technology and was used as the solver for this study.

The geometry used for these models was a 40 mm deep sample with the centre of the defect located at a depth of 20 mm. The sample width was set to 80 mm to ensure any reflections from the edge of the sample arrived after the signals of interest, this can be seen in the schematic in figure 5.4. Defects were added by removing appropriate elements from the mesh to leave a void in the shape of the defect.

To acquire an FMC data set from this model, the same process a physical array uses is

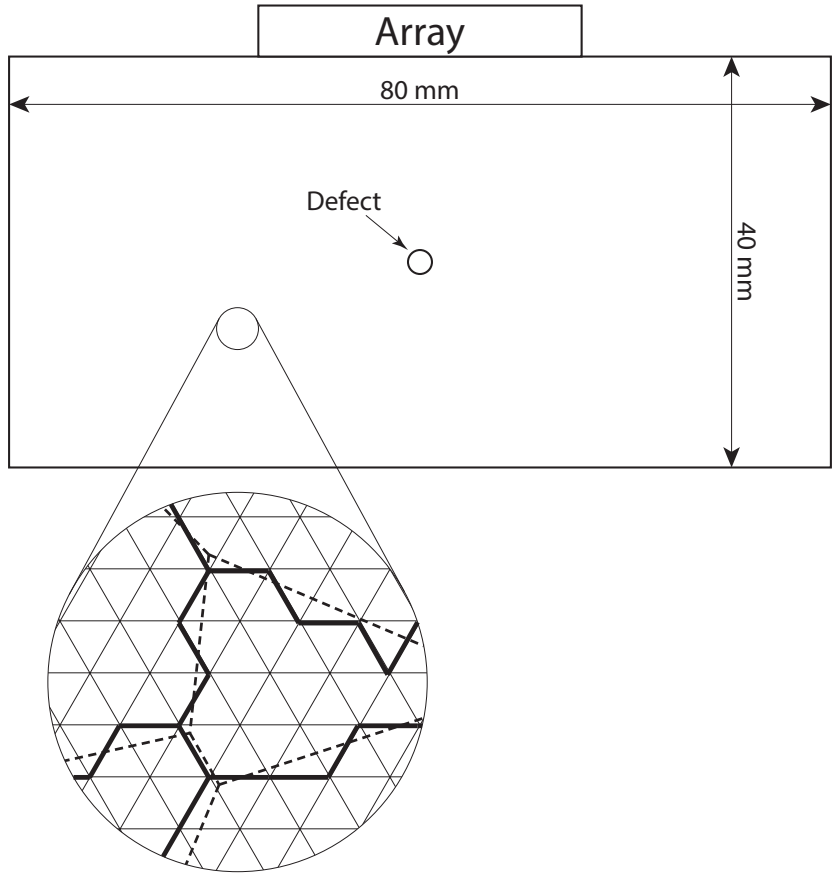

Figure 5.4: The FE model's geometry.

followed. The vertical displacement at nodes on the top edge of the model, corresponding to the location of an arrays piezoelectric elements (6 nodes per element), are monitored while a vertical force is applied to the nodes representing a single element of the array to excite a wideband ultrasonic pulse. The vertical displacements of the nodes representing each element in the array are summed to give the response of that element. This process is repeated for all elements to create the response from all transmit-receive element pairs. The array geometry used is the same as that in the experimental validation case with the same centre frequency of 2.5 MHz, however, a single cycled Gaussian windowed pulse was used to achieve a wider frequency spectrum than that used in the experimental measurements.

The model was initially run with no defect and for side-drilled holes of diameter 0.5 mm, 2

mm and 5 mm, and horizontal cracks of length 2 mm and 5mm. For each of these cases, the model was run using 30 different realisations of random grain structures. The superposition technique was then applied to the defect-free results and a direct comparison could be made between those and the FE results with the defect present.

Despite the improvements in computing hardware, this is still a computationally expensive process. When run on an Nvidia K600 GPU, each run of this model requires approximately 15 minutes to complete and for a 64 element array, each FMC data set requires 64 runs. This process must be done for each of the 30 grain structures being modelled which leads to a total run time of approximately three weeks per defect.

5.1.4 Superposition with the FE model

To apply the superposition technique to the FE model's results, the defect-free results can largely be treated as a standard experimental data set and the process outlined in section 4.1 can be followed. The only major exception is that to calculate the attenuation coefficient, neither technique described in section 2.2.2 can be followed as only the direct contact response from a single sample is available. Further simulations could be performed to acquire data from a different thickness of material, however, as the FE model assumes a vacuum interface at its boundary, there are no losses to the environment during the back wall reflection, or to the array during the front wall reflection. Because of this, the second back wall reflection is equivalent to the first back wall reflection from a sample of twice the thickness and can be treated as such for the purposes of calculating attenuation. To achieve higher accuracy for the attenuation measurement, and to reduce any uncertainty associated with it, the mean signal from all 30 defect-free data sets was used, these results can be seen in figure 5.5. Increasing the number of data sets used for the attenuation calculation, it has allowed α to be determined experimentally over almost the full range of frequencies present in the received signal, therefore little extrapolation is required.

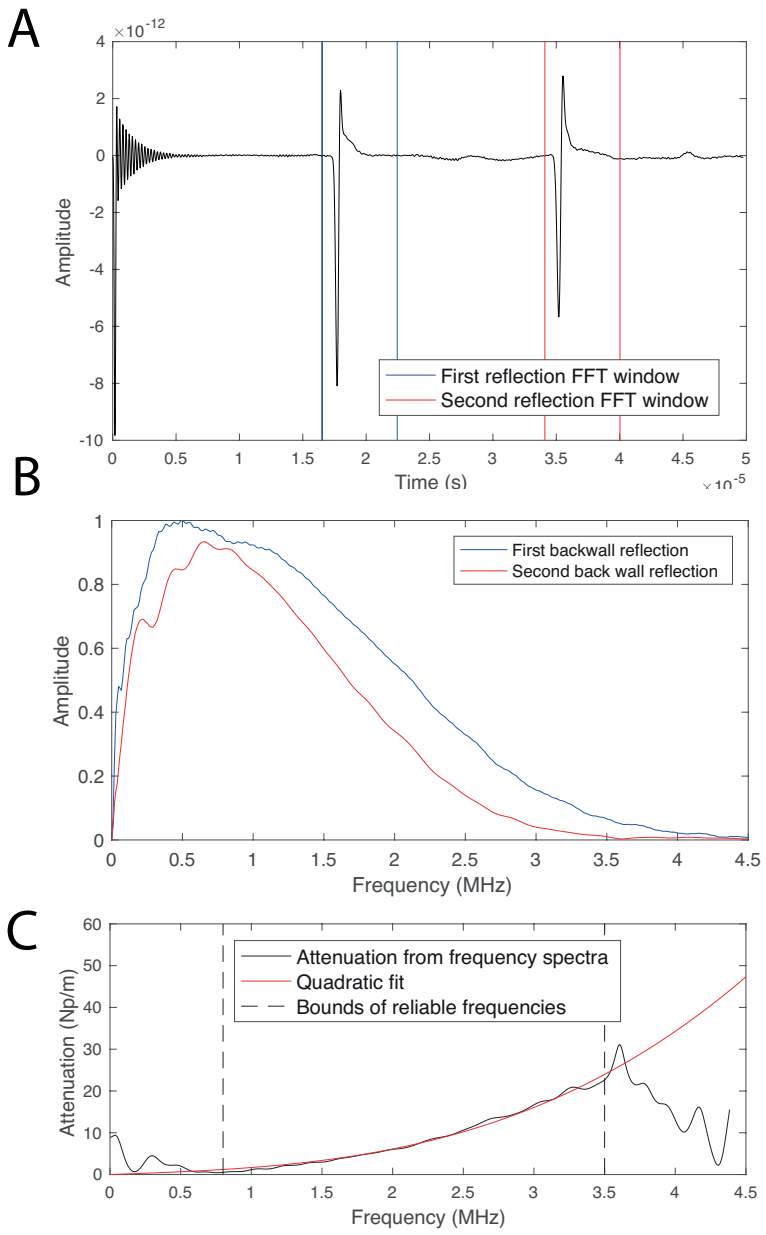

Figure 5.5: Sum of the time traces from all transmit-receive pairs of the array averaged over multiple realisations and the relevant windows for the Fourier transform for the first two back wall reflections (A), the normalised frequency spectra of these reflections (B) and the frequency dependant attenuation coefficient calculated from these spectra (C).

5.2 Results

Figure 5.6 shows images created using the TFM. In the first column, the data is filtered with a 2.5 MHz centre frequency Gaussian filter with a half bandwidth (defined as the point where the amplitude of the filter drops to -40 dB) of 2.5 MHz before imaging. In the other columns the data is filtered with 0.5 MHz half bandwidth Gaussian filters at the centre frequencies stated. Row A shows images from one realisation of the defect-free case from the FE model, row B shows the analytically calculated defect and shadowing responses for a 0.5 mm side-drilled hole, row C shows the superposition of the results from rows A & B, row D shows the FE model with a 0.5 mm side-drilled hole for the same realisation of grains as in row A. Finally row E shows the difference between rows A & D. The equivalent results for the 2 mm and 5 mm side-drilled holes and the 2 mm and 5 mm cracks are shown in figures 5.7-5.10 respectively.

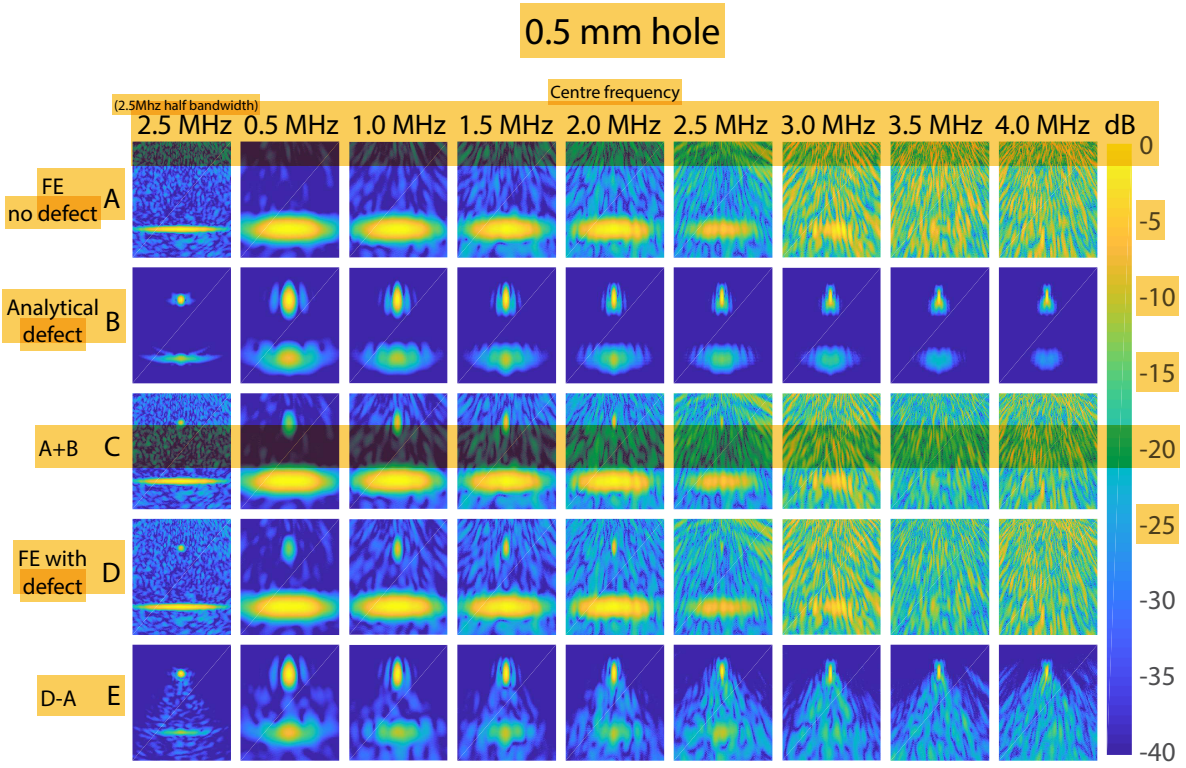

Figure 5.6: TFM images at various frequencies of FE defect-free case (A), the analytically calculated defect response and shadowing effects for a 0.5 mm hole (B), the superposition of A & B (C), FE model with defect present (D) and the difference between A & D (E) . All images are filtered at the labelled centre frequency with a half bandwidth of 0.5 MHz except the 2.5 MHz full bandwidth column which has a 2.5 MHz half bandwidth.

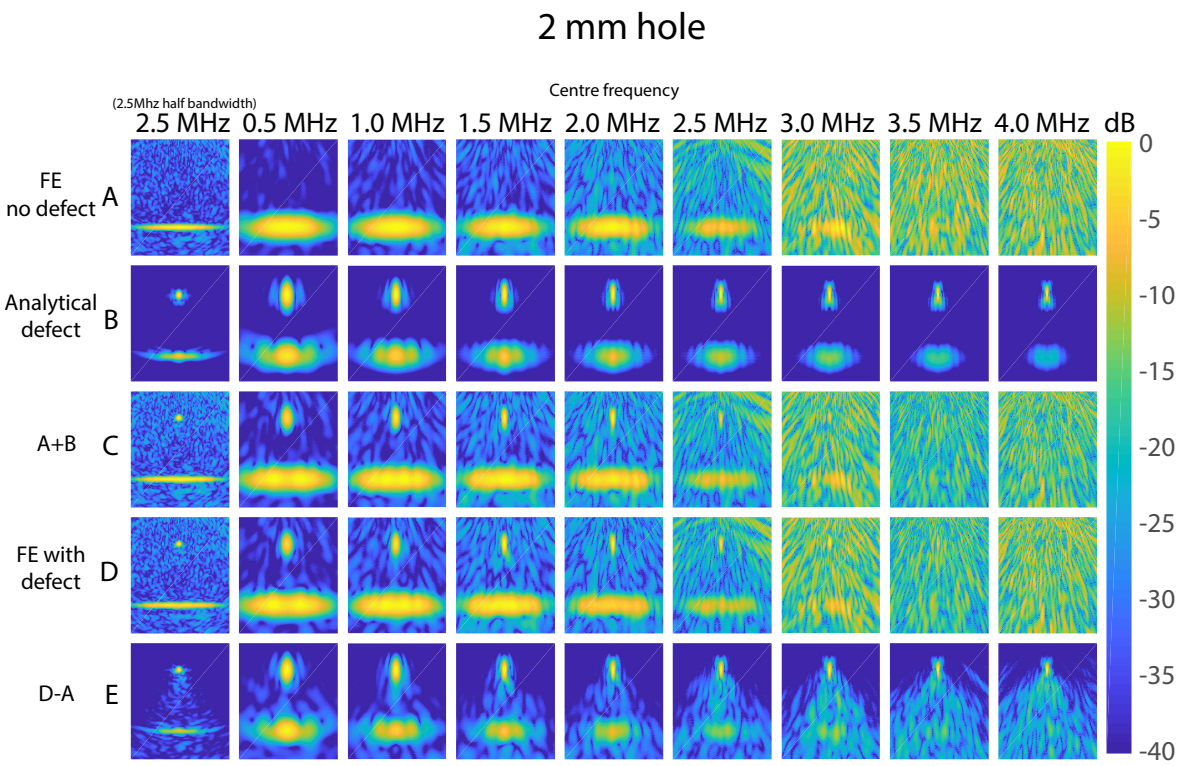

Figure 5.7: TFM images at various frequencies of FE defect-free case (A), the analytically calculated defect response and shadowing effects for a 2 mm hole (B), the superposition of A & B (C), FE model with defect present (D) and the difference between A & D (E) . All images are filtered at the labelled centre frequency with a half bandwidth of 0.5 MHz except the 2.5 MHz full bandwidth column which has a 2.5 MHz half bandwidth.

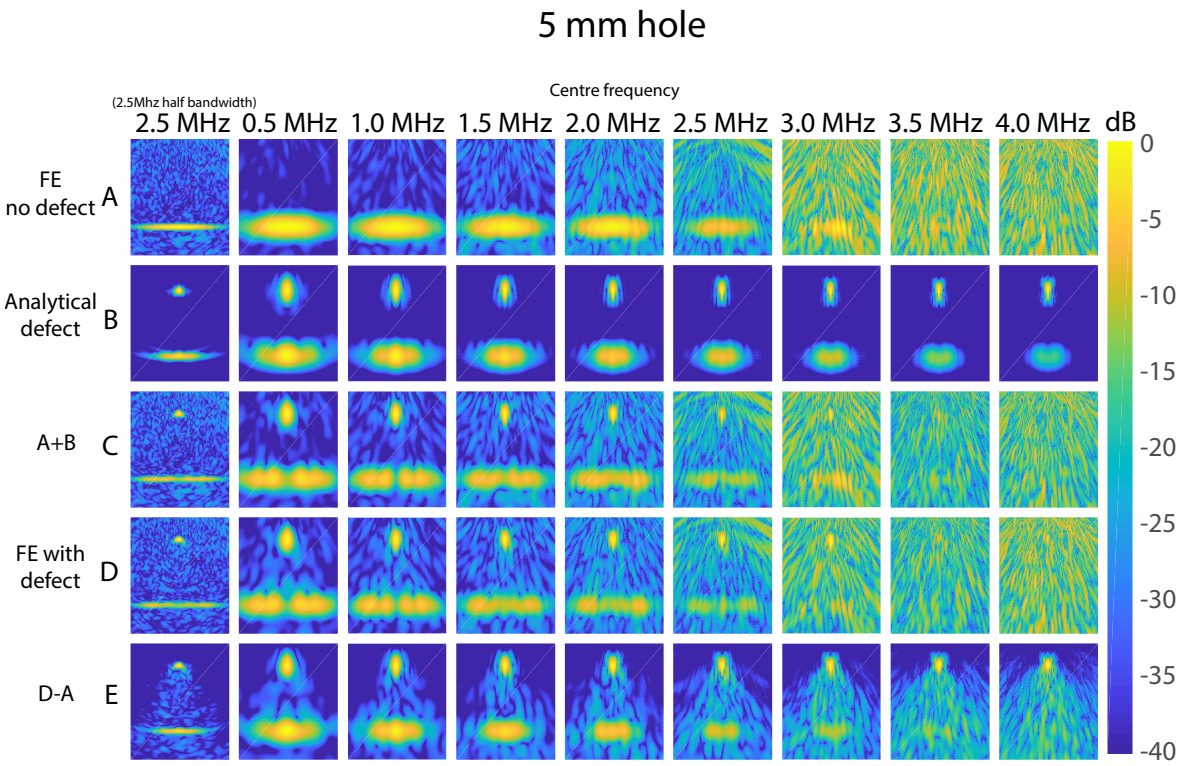

Figure 5.8: TFM images at various frequencies of FE defect-free case (A), the analytically calculated defect response and shadowing effects for a 5 mm hole (B), the superposition of A & B (C), FE model with defect present (D) and the difference between A & D (E) . All images are filtered at the labelled centre frequency with a half bandwidth of 0.5 MHz except the 2.5 MHz full bandwidth column which has a 2.5 MHz half bandwidth.

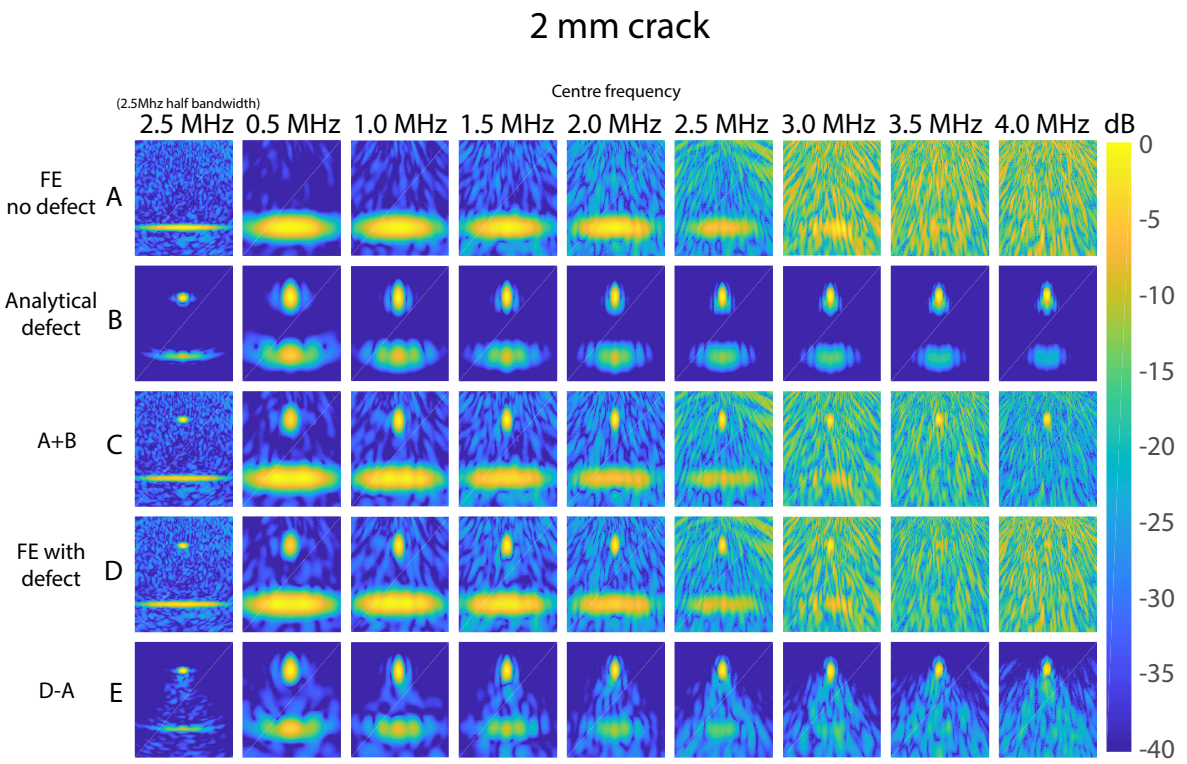

Figure 5.9: TFM images at various frequencies of FE defect-free case (A), the analytically calculated defect response and shadowing effects for a 2 mm crack (B), the superposition of A & B (C), FE model with defect present (D) and the difference between A & D (E) . All images are filtered at the labelled centre frequency with a half bandwidth of 0.5 MHz except the 2.5 MHz full bandwidth column which has a 2.5 MHz half bandwidth.

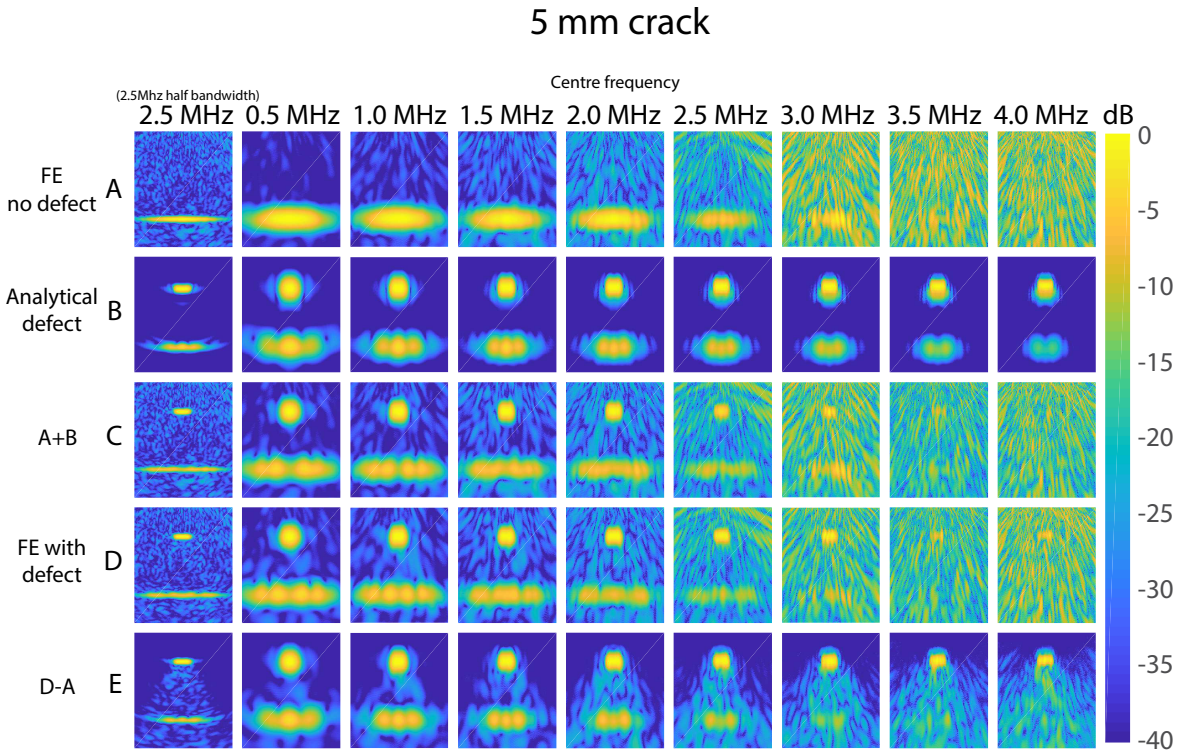

Figure 5.10: TFM images at various frequencies of FE defect-free case (A), the analytically calculated defect response and shadowing effects for a 5 mm crack (B), the superposition of A & B (C), FE model with defect present (D) and the difference between A & D (E) . All images are filtered at the labelled centre frequency with a half bandwidth of 0.5 MHz except the 2.5 MHz full bandwidth column which has a 2.5 MHz half bandwidth.

Initially focusing on the first column, comparing rows C & D in the figures 5.6-5.10, it can be seen that the superposition model gives results which broadly show good agreement between the FE model results for all of the presented defects when filtered over a wide bandwidth as is typical in an industrial setting. The defect amplitudes and shapes are well matched in all cases but the back walls start showing signs of errors as the defect size increases with the 5 mm crack showing a noticeable difference in amplitude where the shadowing occurs. These multiple scattering effects present the biggest difficulty in simulating accurately, especially when the level of shadowing is large such as this case. However these are also the cases where there is generally less need for a high degree of accuracy due to the defect being clearly visible.

The subsequent columns show the same data filtered with a narrow 0.5 MHz half-bandwidth at increasing center frequencies. It is clear in all cases that at centre frequencies of 3.5 MHz and above the noise dominates the response. For the 0.5 mm and 2 mm holes, there are no discernible features in the images and for the remainder of the defects, the defect response itself can be seen but locating it would be difficult without prior knowledge and there is no sign of the back wall. As the frequency is increased, the level of backscatter increases along with multiple scattering effects between grains which leads to a severe increase in the noise observed in the image. Information on the defect is still contained within all of the image as proved by its response still being visible in row E at these frequencies, however its amplitude is below that of the noise and so may not be visible.

When the narrow filter is applied with a centre frequency of 3.0 MHz, figures 5.6-5.10 show broad agreement, with some amplitude errors, between the simulated results and FE model. The back wall in the defect-free sample is however still heavily masked by noise. The superposition technique is dependant on being able to extract a back wall signal from the defect-free data set. At this frequency and higher it is reasonable to expect that the superposition technique will struggle to provide accurate results due to difficulties in extracting an accurate back wall signal. The images produced at these frequencies exhibit such a high level of noise that it is unlikely that they would be of use in an NDE environment.

Below these frequencies the simulated results show good agreement with the FE results for all of defects for the realisation of noise shown. Wilcox et al. (2011) showed that the onset of significant multiple scattering effects begin at approximately the frequency of maximum SNR. The results in figures 5.6-5.10 show that the model remains accurate beyond this frequency and into the multiple scattering regime. This suggests that the singly-scattered response of the defect remain prevalent even when multiple scattering is strong.

While much of the multiple scattering effects between grains is contained in the defect-free response, multiple scattering between the defects and grains is not. An assumption of the superposition technique is that the defect response and shadowing effect calculated using a scattering matrix is identical to the change in the image caused by introducing a physical defect to the sample. If this assumption was true, rows B & E in figures 5.6-5.10 would be identical. As can be seen, the defect and shadowing results response are generally well matched, however, row E shows large amount of image speckle for all defects which is not present in the analytical model's results in row B. This is caused by multiple scattering between the defect and grains. Effectively, the defect is shadowing a region of grains from the array and this leads to the speckle behind the defect predicted by the superposition technique being different to the speckle observed in the full FE model. However, for practical purposes it can only be considered an error if this alters the speckle statistics in this region as the precise speckle pattern is naturally random in nature.

5.3 Measuring variations in noise

While row E in figures 5.7-5.10 show the region of the images where there is a difference in image speckle, the response from the defect and back wall affect a much larger portion of the image than can be seen on the 40 dB scale of those images. Figure 5.11 shows the analytical model results for a 5 mm side drilled hole at a filter centre frequency of 1 MHz. Artefacts from the defect and back wall can be seen to have an effect over an entire region where there is a different in image

speckle. Therefore any errors in, predominantly the defect, but also the back wall depending on where the measurment is taken, will manifest as an increased error in the RMS noise value. This is compounded at lower frequencies as the responses cover a larger area spatially so these artefacts extend further into the bounded region. Additionally, at these frequencies, the true RMS noise value is relatively low so these artefacts will have a more significant impact on the results. To minimise the effect this has, noise measurements were taken from the area least affected by the artefacts, shown bounded in red in figure 5.11. While this area is small relative to the wavelength and speckle correlation length, the convergence study seen in figure 5.12 shows that the RMS noise level in this region has converged by averaging over 30 realisations.

The pixel amplitudes of the image speckle follows a Rayleigh distribution (Goodman, 2007) which is a function of a single variable proportional to their RMS amplitude so this value can be used to characterise the speckle. Figure 5.13 shows the RMS of the noise in the region behind the defect in the superposition model subtracted from the RMS noise from the FE model calculated in the same manner. The results were averaged over 30 realisations of noise and calculated for all the defects discussed in this section.

Figure 5.13 shows how the calculated RMS noise error is relatively high at lower frequencies and for larger defects but soon drops off to under 1 dB for the smaller defects as the frequency increases and the defect and back wall artefacts have a smaller influence.

While these results do suggest significant errors in the RMS noise value, the absolute values of the noise is significantly higher at higher frequencies as shown in figure 5.14. This means that when imaging is performed using a wider bandwidth filter, such as those typical of an NDE inspection, the overall RMS error is dominated by the errors at the higher end of the frequency spectrum.

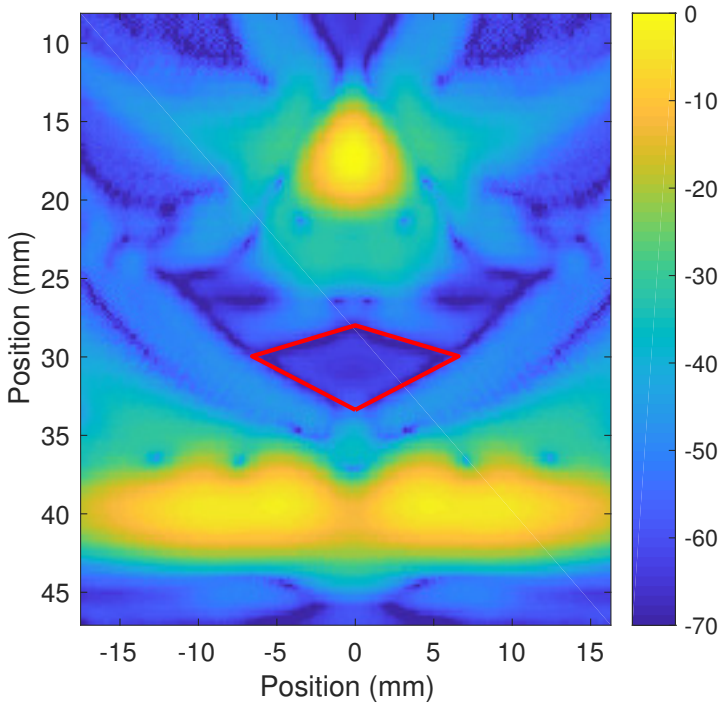

Figure 5.11: Image of a 5 mm side-drilled hole with the region used to calculate the RMS noise value shown in red.

5.4 Establishing frequency limits

To gain a more quantitative understanding of the limit at which the superposition technique is valid, the results filtered over a narrow bandwidth were studied for all 30 noise realisations. This allows the accuracy of the model to be investigated as the SNR drops and to determine over what range the superposition technique is valid. This analysis was performed to allow an understanding of the range of expected image amplitudes from nominally identical experimental data sets, for which the FE results are analogous, and how this range compares to the range predicted by the superposition technique.

From these results, the mean and standard deviation of the image amplitude was calculated for various features. These features are; the maximum amplitude of the defect; the mean

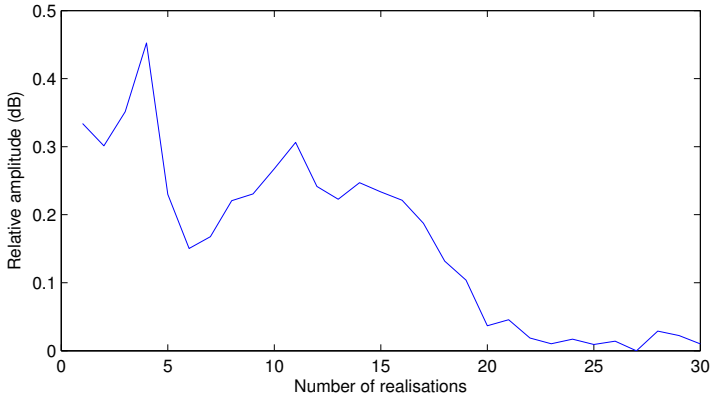

Figure 5.12: RMS noise level versus the number of realisations averaged when measured at the region shown in figure 5.11 using the full bandwidth of the array.

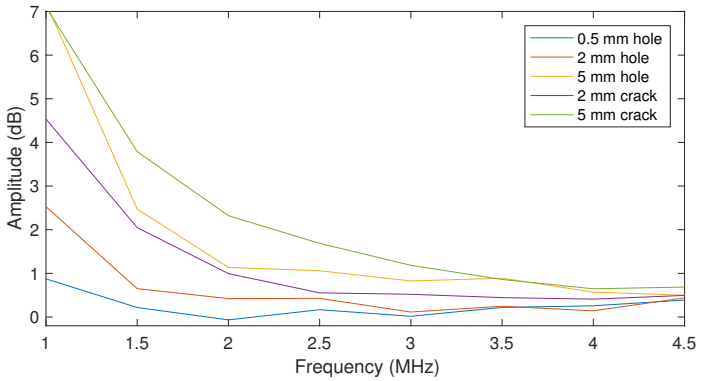

Figure 5.13: RMS noise error in region behind defect.

amplitude along a line 10 mm long, parallel to the back wall and located in the centre of the back wall; and the RMS noise measured in the region behind the defect. This was done for the superposition model and the FE model as a function of frequency for side-drilled holes of size 0.5 mm, 2 mm and 5 mm in figure 5.15 and for 2 mm and 5 mm horizontal cracks in figure 5.16.

These results show that the superposition technique provides an accurate prediction for defect image amplitude and RMS noise level for all defects simulated. Additionally, back wall shadowing effects are, in general, reproduced accurately but some discrepancies are seen for some of the larger defects (2 mm hole, 5 mm crack & hole) over a limited frequency range at the lower end of the spectrum. At the higher end of the frequency spectrum, the superposition technique

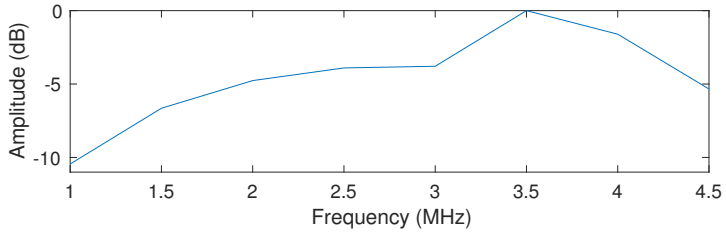

Figure 5.14: Normalised amplitude of the RMS noise in the defect-free case at different frequencies.

Error in:	Defect	RMS noise	Back wall shadowing
0.5 mm hole	-0.02 dB	-0.07 dB	-0.15 dB
2.0 mm hole	0.20 dB	0.15 dB	-0.20 dB
5.0 mm hole	0.05 dB	2.23 dB	-0.88 dB
2.0 mm crack	0.33 dB	0.52 dB	-0.19 dB
5.0 mm crack	0.34 dB	1.40 dB	0.06 dB

Table 5.2: Wide-bandwidth mean image amplitude errors.

shows a significantly wider spread of defect image amplitudes between different realisations of noise than the range observed in the FE results. When viewed in isolation, these errors are not insignificant, however, when the data is filtered over a bandwidth more typical of an NDT inspection, there is little discrepancy. Table 5.2 shows the mean image amplitude difference between the FE model and superposition model when filtered at a centre frequency and half-bandwidth equal to 2.0 MHz. Figure 5.5B shows that there is negligible frequency content in the received signals above 4 MHz which is why a filter ranging from 0-4 MHz was chosen.

The mean differences in image amplitudes show that the superposition technique gives very accurate results for the defect responses and shadowing effects. It also shows that there is a negligible difference in the RMS noise of the affected region behind the defect for all but the largest defects whose errors are of the order of 2 dB.

While the results seen in figures 5.15 and 5.16 show that the superposition model ceases to be a reliable approximation to the true response as frequency increases, the upper frequencies presented give a SNR in the image sufficiently low that the image would be deemed unusable

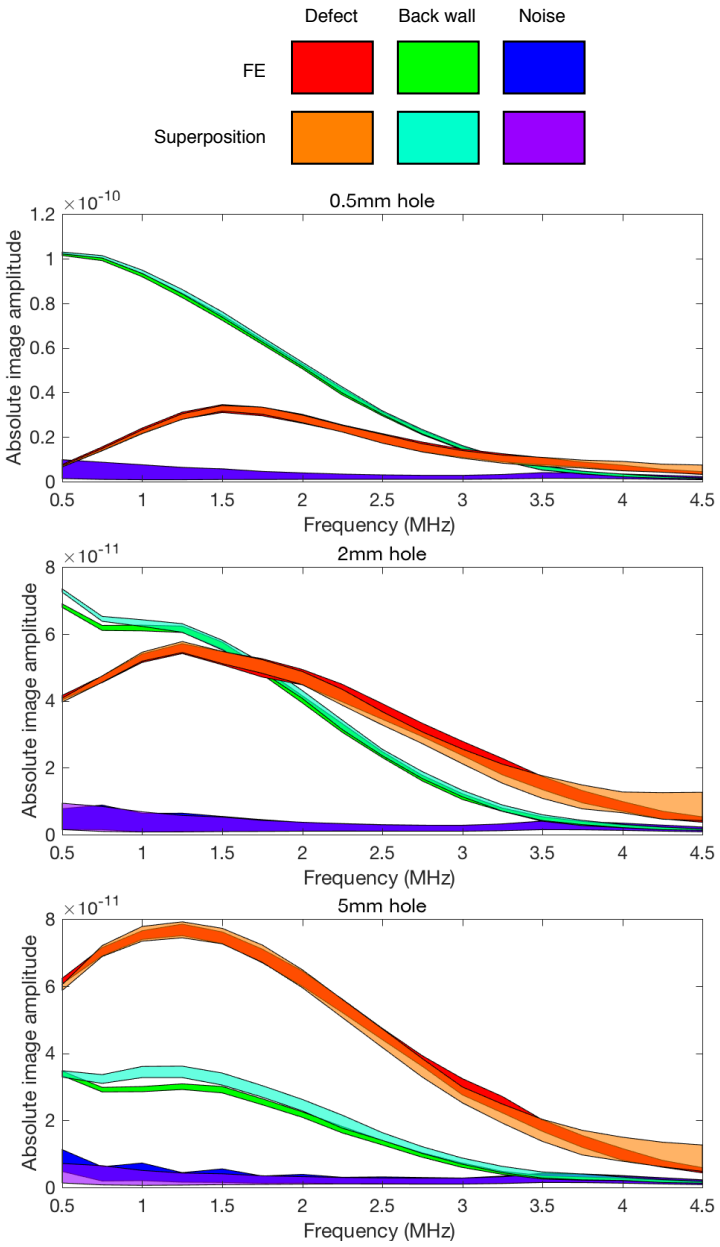

Figure 5.15: Comparisons between FE and superposition model images amplitudes measured at the defect and back wall for various size holes and the RMS noise value in the region behind the defect. The lines are centred on the mean over the 30 realisations of noise with the line width representing two standard deviations. The filter half-bandwidth is 0.5 MHz.

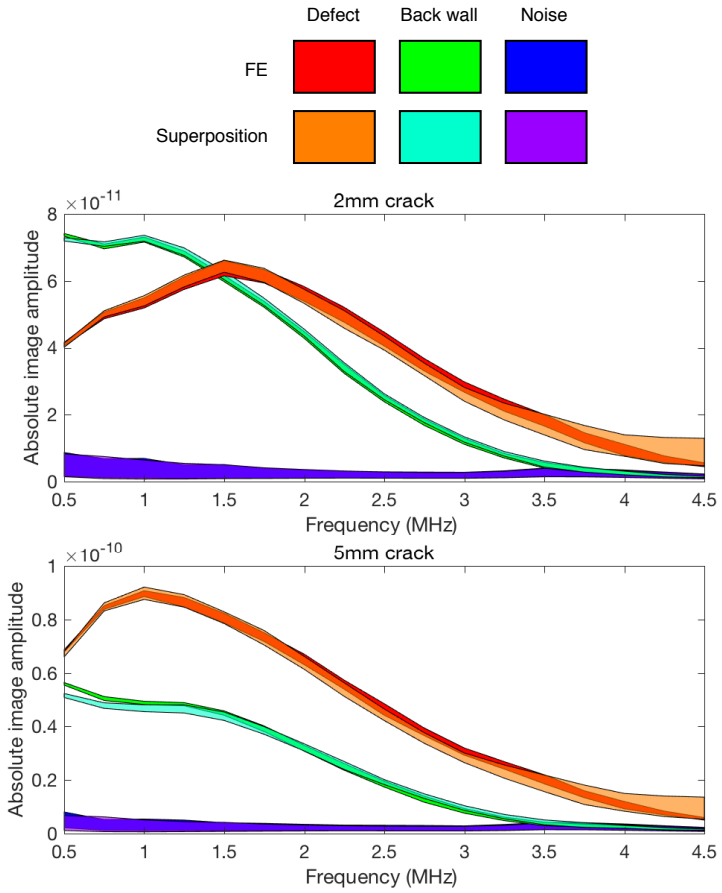

Figure 5.16: Comparisons between FE and superposition model images amplitudes measured at the defect and back wall for various size cracks and the RMS noise value in the region behind the defect. The lines are centred on the mean over the 30 realisations of noise with the line width representing two standard deviations. The filter half-bandwidth is 0.5 MHz.

due to the lack of visibility of any of the major features. For this reason it is necessary to define the frequency range of interest over which it is suitable to perform the inspection if the aim is to detect a given defect. This is done by considering the mean SNR of the defects, once the SNR drops below a certain level, it becomes impossible to achieve an adequate probability of detection without incurring a high number of false alarms as it becomes more likely that image speckle will have an amplitude comparable to that of the defect.

The SNR, calculated as the ratio between the maximum amplitude of the target and the RMS noise value, was evaluated for all of the defects and for the back wall in the defect-free case. The RMS noise value was calculated from the noise at the same position as the defect in the defect-free FE model images and was averaged over all 30 realisations. The results are shown in figure 5.17.

It is common practice to set a threshold amplitude, over which any pixel in the image can be considered a defect. For this work, the threshold level has been set at 12.5 dB above the RMS noise value and this can also be seen in figure 5.17. This has been calculated to give a false call ratio of 1 in 1000 for the given image size and assuming the image pixel amplitude due to speckle follows a Rayleigh distribution. This threshold level is arbitrary for this work and is much higher than the common industrial standard of 6 dB. However, due to the high level of noise in these images, a threshold of 6 dB would likely lead to multiple false calls per image as many of the individual speckles are greater than 6 dB above the RMS value.

The results in figure 5.17 show that the SNR falls below the threshold value at between approximately 3.2 and 4.0 MHz for the various defects and back wall. These frequencies can be considered as the limits of detectability for the given defect as at higher frequencies, the inspection is unable to detect the defect without exceeding the acceptable false call ratio criterion. These frequencies also correlate approximately with where the back wall image amplitudes become comparable with the RMS noise amplitude seen in figures 5.15 and 5.16. Below these frequencies, the superposition technique provides results that are on average accurate to within

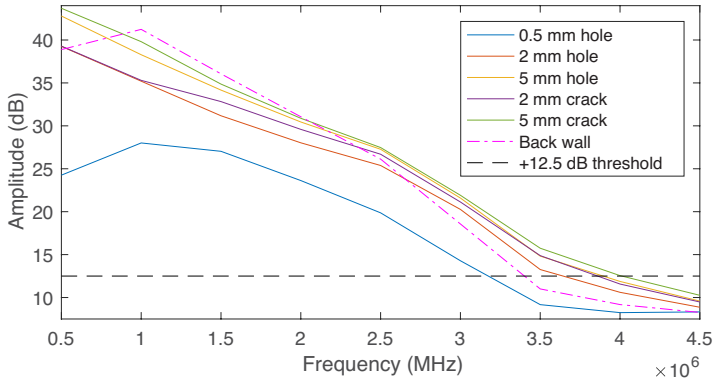

Figure 5.17: SNR of defects and back wall. The filter half-bandwidth for the images from which the data is taken is 0.5 MHz.

1 dB.

Above these frequencies, figures 5.15 and 5.16 show that there is a significantly increased variation in predicted image amplitudes. The superposition technique is believed to fail at higher frequencies because it becomes impossible to reliably extract an input signal from the back wall to use in the analytical defect model, rather than a failure in the superposition assumption itself. This is because the back wall amplitude falls within the expected range of the noise amplitude and so any extracted input signal will be dominated by noise and have little correlation to the signal produced by the array or in this case, simulated array.

5.5 Defects at the limit of detectability

While figures 5.6-5.10 show that the superposition technique provides accurate results for the defects presented, the defects considered are all sufficiently large that they are significantly over the threshold value when imaged at a suitable frequency and can only be brought to the limit of detectability by de-optimising the imaging process. To get a true representation of how the superposition model performs for defects near the limit of what is detectable, its results were compared to the FE model for the smallest side-drilled hole which consistently produced image

amplitudes greater than the threshold value. To determine the size of this hole, the sensitivity to defects of the inspection was maximised by use of an optimised standard Gaussian filter (defined as where the half-bandwidth is equal to the centre frequency). The superposition technique was then used to estimate the smallest hole diameter which would produce an image amplitude marginally greater than the +12.5 dB threshold, this was calculated to be 0.14 mm. This defect was then simulated using the FE model and the results compared.

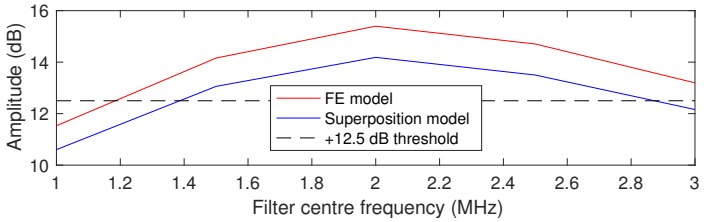

Figure 5.18: Mean of 30 realisations of SNR of a 0.14 mm side-drilled hole simulated using the FE model and superposition technique. The filter is a standard Gaussian filter with a half bandwidth equal to the centre frequency.

Figure 5.18 shows how the SNR of this defect varies with the filter frequency used for both the FE model and superposition technique. A 2.0 MHz filter gave the highest SNR for both models and was therefore chosen as the optimum frequency.

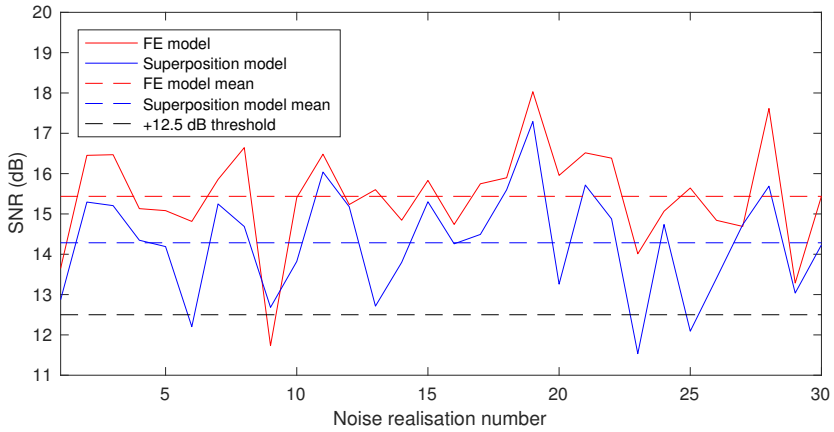

Figure 5.19: SNR for each of the 30 realisations of the FE model and superposition model for a 0.14 mm side-drilled hole. The filter is a standard Gaussian filter with a half bandwidth and centre frequency of 2 MHz.

Figure 5.19 shows the SNR of this defect filtered with the optimum filter for each of the

noise realisations. The mean result produced by the superposition technique is approximately 1 dB lower that the mean amplitude predicted by the FE model. The results in figure 5.19 show that there is a significant variation in image amplitude between noise realisations for both sets of results and some individual results from both models fall below the threshold value. However, this 1 dB mean error appears to be a systematic error in the model rather than as a result of random noise. There are several potential causes for this error, the defect amplitude could have errors due to discretisation of the defect in the FE model due to the nature of the mesh which is discussed in more detail shortly. Errors in the calculated RMS noise value may also be present due to the shadowing of the grains by the defect in the FE model which does not occur in the superposition model. The variations observed between noise realisations is also greater in the superposition model, a trend which was also seen for the larger defects studied.

Figure 5.20 shows the equivalent to figures 5.6-5.10 for a 0.14 mm side-drilled hole but with the first column filtered with the chosen optimum standard filter. Figure 5.20 (and 5.6-5.10) was created using noise realisation number 13 which shows one of the largest variations between FE and superposition model for this defect. The results in the first column of figure 5.20 show that the image amplitude of the defect is only just visually discernible from the noise. However, despite representing one of the largest variations between models, the two results do still show good visual agreement. When imaged over a narrow bandwidth, it is not be possible to confidently identify the defect. This confirms that the defect is indeed at the limit of what is detectable in this inspection.

One likely source of error which will affect this defect more than the larger defects is another consequence of using a structured mesh. Due to the fixed triangular grid of nodes used for the mesh, it is not possible to perfectly describe a round boundary for a side-drilled hole. With larger defects, a very good approximation can be achieved, but for a defect of this size, by necessity, the void left in the mesh to represent the defect is hexagonal rather than a close approximation to circular. To determine if this is the cause of the error, the scattering matrix of the defect could be extracted from the FE model and compared to the scattering matrix used

in the superposition model. If there is a discrepancy, the FE scattering matrix could be used within the superposition model and if this was the cause, the new results should show closer agreement.

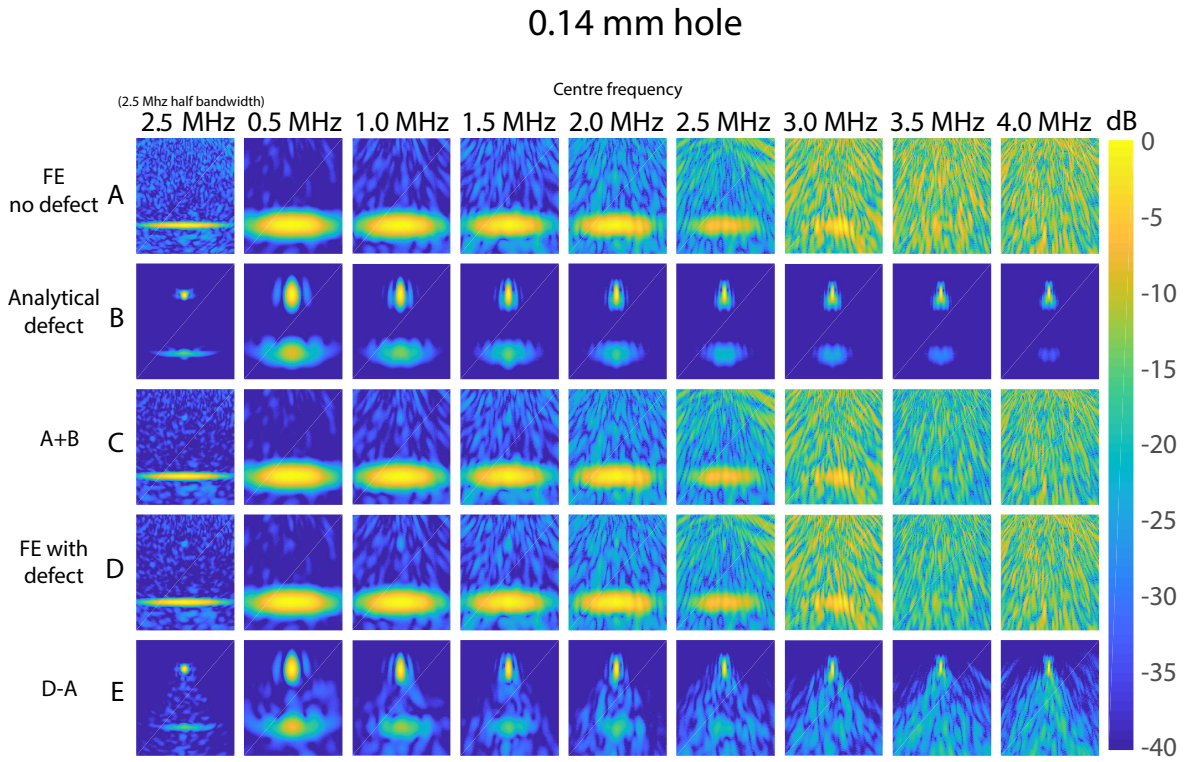

Figure 5.20: TFM images at various frequencies of FE defect-free case (A), the analytically calculated defect response and shadowing effects for a 0.14 mm hole (B), the superposition of A & B (C), FE model with defect present (D) and the difference between A & D (E) . All images are filtered at the labelled centre frequency with a half bandwidth of 0.5 MHz except the 2.5 MHz full bandwidth column which has a 2.5 MHz half bandwidth.

6 Applications of the technique

The key advantage this technique offers over the currently established modelling techniques is the efficiency with which it can be used to simulate large quantities of data with accurate SNR values. This enables statistical studies on an inspection's sensitivity to defects to be performed much more easily. Such studies are a vital part of the acceptance procedures for implementing new NDE inspections. Traditionally these studies have been performed using experimental data but this approach poses several challenges. Physical samples with real defects are generally not readily available, and if they are, determining the exact nature and size of the defect is non-trivial. Samples can be made with defects artificially introduced however these are expensive to produce which therefore limits the achievable sample size .

These analyses are commonly done in the form of a Probability of Detection (POD) study (Rummel, 1998), usually expressed as a graph of defect size versus the probability of detection which accounts for both human factors in performing the inspection, and the detectability of the defect with the given inspection method. For the reasons discussed above, there is a trend in industry towards using Modal-Assisted Probability of Detection (MAPOD) (Knopp et al., 2007; Smith et al., 2007; Dominguez et al., 2014) to reduce the volume of experimental samples required. However, to date, these studies have been limited to low noise inspections and often single element transducers due to the difficulties in modelling more complex inspections. The ability to expand these methods to samples with high levels of structural noise is of obvious practical benefit.

Receiver Operator Curves (ROCs) are another common method used to analyse an inspection procedure (Nockemann et al., 1991). These curves plot the likelihood of making a false positive call against making a true positive call as a detection threshold level is varied. To calculate these curves, the distribution of the expected defect response and noise level is required. The noise level is relatively easy to acquire from experimental samples but the difficulty of empirically calculating defect response distributions for the full range of defects needed could be greatly

reduced or even entirely removed by utilising the superposition technique.

The proposed technique also allows detailed studies of an inspection's sensitivity to different defects. As an example, if one wanted to gain an understanding of an inspection's sensitivity to the angle of a straight crack in a high noise sample, it could be done empirically by creating multiple samples with cracks at varying angles. However, many samples would have to be made for each crack angle to produce statistically significant results. The superposition technique allows this to be done without the need for multiple defects to be machined. Here, a 1 mm crack is simulated using a semi-analytical scattering matrix (Glushkov et al., 2006), it is located 5 mm above the back wall of a 65 mm deep copper sample. The array used is the same as detailed in 2.1. Figure 6.1 shows TFM images cropped to the back wall and defect for various angles of this crack for a single noise realisation. These results were combined with 20 independent defect-free experimental data sets to provide the data on which a statistical study could be based. As the crack rotates from horizontal, its amplitude in the image decreases. At a certain angle, the amplitude drops below the level of the image noise and becomes indistinguishable from the speckle, this can be seen to occur between figures 6.1c and 6.1d.

A threshold amplitude of the RMS noise +12 dB was chosen to determine if any point in the image is a defect. The choice of this threshold is arbitrary and depends on external factors for a particular inspection which typically involve balancing the costs of false positives (false calls) with detection sensitivity. The effect of the threshold on false call rate can be estimated: if the image grain noise is assumed to have a Rayleigh distribution (the expected amplitude distribution for fully-developed speckle) and to have a spatial correlation length of one wavelength (1.9 mm) then a threshold 12 dB above the RMS level is expected to result in a 0.46% false call rate assuming a 50 mm wide image of the full depth of the sample.

Figure 6.2 shows how this threshold level compares to the image amplitude for the crack at a range of angles. The minimum defect amplitude was calculated at a 97.5% confidence level, using this, it can be seen that this defect falls under the threshold value at a crack angle of

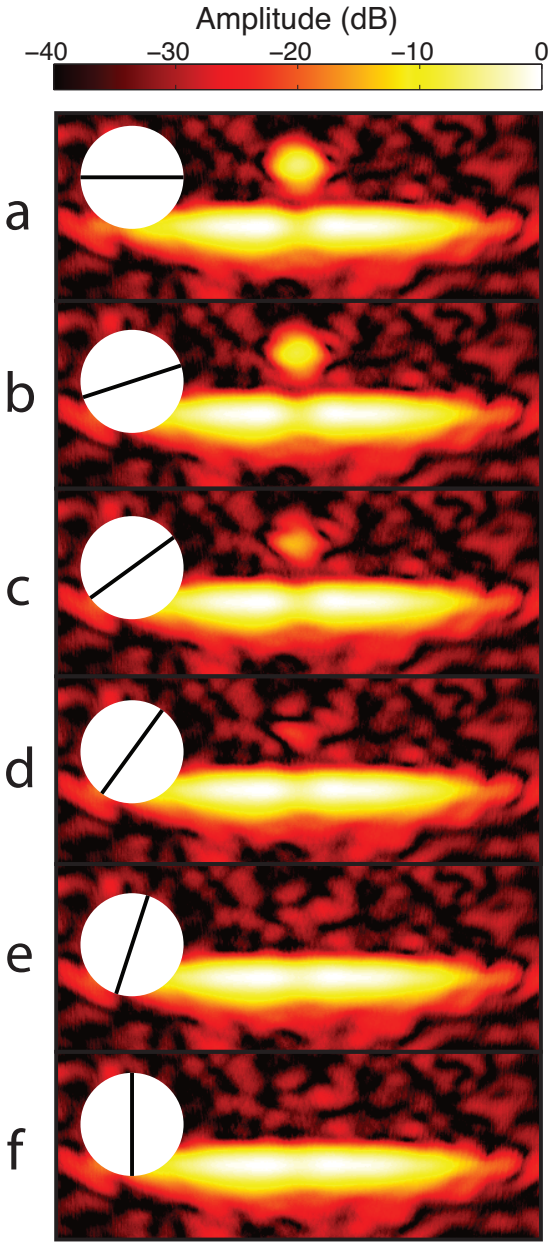

Figure 6.1: TFM images for a 1 mm (0.8 λ) crack located 5 mm from the back wall of a 65 mm deep specimen inclined at 0°(a), 18°(b), 36°(c), 54°(d), 72°(e) and 90°(f) anti-clockwise from horizontal with a crack angle schematic inset.

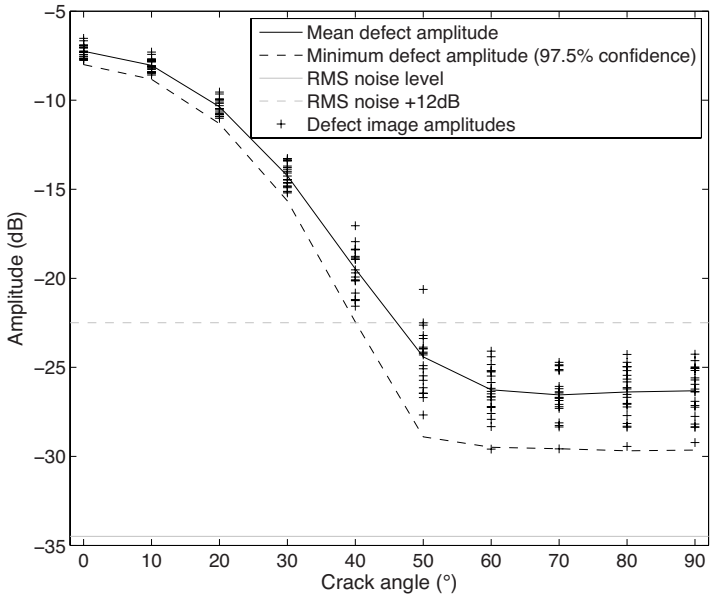

Figure 6.2: Defect image amplitude vs crack angle for a 1 mm crack located 5 mm from the back wall of a 65 mm deep copper sample.

greater than 40°. If the distribution of expected crack angles in the sample is known then it is possible to calculate the probability of a crack of this size being detected if examining only the defect. However, by analysing the back wall amplitude, it can be seen that shadowing effects cause a statistically significant amplitude drop for the full range of crack angles, these results can be seen in figure 6.3.

These inspection and defect parameters were chosen arbitrarily as one example of the insights into an inspection that the superposition technique can achieve. Using the same set of defect-free data, it is possible to create a similar analysis for any defect using the appropriate scattering matrix. By repeating this process for a range of defects over all positions in the image, it is possible to build a map of what defects are detectable in a given position to verify that the inspection is capable of detecting any defect of a critical size.

While the case shown here is an arbitrary one, the technique offers the potential to be

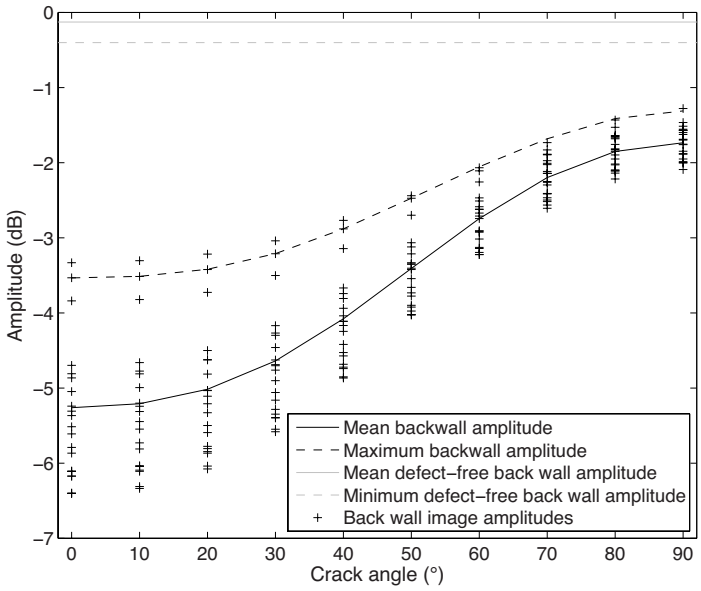

Figure 6.3: Back wall image amplitude vs crack angle for a 1 mm crack located 5 mm from the back wall of a 65 mm deep copper sample. The minimum defect-free back wall amplitude is calculated at a 99.9% confidence level and the maximum back wall amplitude is calculated at the 97.5% confidence level.

applied in a wide range of applications beyond the scope of what it was initially intended for. Simulating large volumes of realistic imaging data efficiently is not only of use in validating inspections such as was the need for BAE, but also in many other areas, both in research and industry. For example, it could provide images to train and test NDE operators in analysing phased array images or be used to test and develop cutting-edge imaging algorithms.

In its current form, the technique is fundamentally limited to scenarios in which the geometry of the sample is known accurately and there is a well defined back wall reflection in the experimental data. There has been a strong focus in this work on back wall shadowing effects, however, this was primarily as a means of rigorously testing the technique. For many inspections, the defect response is of much greater concern than the back wall. Achieving accurate defect amplitudes with the superposition technique is more tolerant of errors in the calculated input signal which may be more challenging to extract in industrial settings where the front and back

walls of the sample may not be cleanly machined, flat or suffer from corrosion and deformations. While careful experimental validation would be required, using simulations with only ray path b from figure 2.1 may be sufficient in many applications where the back wall shadowing effects are not of primary concern, this is especially true for off-axis defects such as those shown in figure 4.6 where no shadowing of the back wall occurs (though artefacts of multiple scattering between the defect and back wall may still exist as in figure 4.7).

7 Conclusions

The main aim of the work presented in this thesis was to develop a model capable of accurately simulating ultrasonic imaging data efficiently such that it could be used to simulate large quantities of data in a reasonable time frame. By using experimentally captured data for the aspects of the model which are traditionally challenging to simulate, the coherent noise, the model was kept computationally efficient and the run time was determined almost exclusively by the time taken to simulate the defect response.

The method, termed the superposition technique, has been shown to have the ability to accurately and reliably simulate defects over a full range of SNR values. It has been validated experimentally using a 64 element, 2.5 MHz array in both aluminium and copper samples containing 1.5 mm diameter side-drilled holes at various depths. The image amplitudes predicted by the model closely matched experimental results, both for defects directly below the array, and for ones located off-axis. When simulating defects close to the array (depths in the region of 5 mm), the model showed errors of up to 1.3 dB, most likely due to the extreme angles between the array elements near the extremes of the array and the defect. Defects outside of this region (depths of 20 mm and greater) were simulated using 20 different noise realisations and all of the results predicted image amplitudes within 1 dB of the experimental results and were on average 0.3 dB different.

The superposition results were also validated against a full time-domain FE model. Results for side-drilled holes of diameters 0.5 mm, 2 mm and 5 mm, and horizontal cracks of 2 mm and 5 mm length were simulated. There was an average discrepancy of 0.34 dB between models. Results from the FE model for a 0.14 mm side-drilled hole, whose amplitude was just greater than the noise level, showed an increased mean error of approximately 1 dB, likely due to the inability of the mesh used to approximate circular voids at this scale. However, this level of error is acceptable in typical NDE environments.

The results of the FE models also showed that while multiple scattering between the defect and grains wasn't accounted for in the model, it had a negligible effect for all but the largest defects, 5 mm cracks and holes, which had errors of the order of 2 dB.

While it can be expected that the defect response amplitude of a given inspection will vary between noise realisations, It was found that the variations between realisations of the superposition model were slightly, but consistently larger, the reasons for this remain unclear.

The technique was shown to be reliable both in predominantly single scattering regimes and when there were high levels of multiple scattering which allows it to be accurate for inspections with high levels of noise and defects with low SNR. When combined with the ray-tracing method to simulate the defect response, it is also extremely efficient, running on a standard computer, simulations took under 30 seconds to produce a full FMC data set if using an analytically calculated scattering matrix.

This model has be shown to provide very accurate results but in all cases it was done using specimens with parallel and flat front and back walls and only included longitudinal waves. The inclusion of other wave modes does not require any fundamental changes to the model, just the inclusion of the appropriate ray paths and their relevant velocities. Dealing with samples with corroded or non-flat faces however, will make extracting the input signal with the method described in section 3.1.1 challenging or impossible. The input signal can be estimated using an alternate sample but the cause of the difficulties in extracting the input signal would also lead to challenges in accurately modelling the shadowing effects. In many practical cases, only the direct reflection from the defect is of major importance so the challenges that may be encountered in simulating the shadowing effects in more complex inspections may not preclude the use of this technique.

7.1 Future work

There are two main avenues to explore for future work in relation to the superposition technique. The first is to further develop the model to expand the scenarios in which it can be used and the second is to apply the technique to supplement other areas of research and industry.

The work presented in this thesis has been focused on direct contact inspections, while these are common in industry, oblique incidence inspections using either wedges or in immersion are also commonly used both in industry and research. The next logical step for furthering the capabilities of the model would be to apply it alongside an oblique incidence ray-tracing model and to include the associated shear wave ray paths to validate the technique for a wider range of inspections. I do not foresee any fundamental issues in the use of this technique with an oblique ray-tracing model, the predominant new challenges I suspect will be encountered are initially developing an oblique model of sufficient accuracy, such models already exist, their accuracy will just require rigorous testing when used in combination with the superposition technique. In implementing this model, I also predict that extracting the required experimental parameters will pose a non-trivial challenge.

Following this, the next major step to establishing this technique in industry would be to analyse a real industrial inspection by using this technique to create the data required to produce an ROC curve and compare it to the results of an ROC curve generated using traditional methods, both in terms of accuracy and cost.

As well as assisting in the validation of more complex inspections, there are many active areas of research in NDE which could benefit from large volumes of accurate data in noisy materials that this technique is capable of producing. One such example is in the development of new imaging algorithms aiding in quantifying the benefits of multi-mode imaging (Zhang et al., 2010; Budyn et al., 2018) as well as optimising data fusion algorithms (Liu et al., 2007).

While this model was created with the intention of validating new inspections, the ability to

create large volumes of realistic imaging data has much wider reaching applications. One of the most exciting of these potential applications is in using it to build training data sets for machine and deep learning algorithms. The scale of the data sets required for this means that they are not economical to create using experimental methods. These techniques are already being applied with great success in medical imaging (Greenspan et al., 2016; Erickson et al., 2017) and the same improvements would be of huge benefit to the NDE industry. From accurately filtering out any defect-free images (which comprise the majority of datasets in practice) so that the NDE operator only needs to analyse the potential failures to reduce their workload and fatigue, to potentially being able to identify and characterise defects to a higher accuracy than is currently possible by any means.

References

Allen, J. L. (1964). "Array antennas: New applications for an old technique". In: *IEEE spectrum* 1.11, pp. 115–130.

Aurenhammer, F. (1991). "Voronoi diagrams - a survey of a fundamental geometric data structure". In: *Computing Surveys* 23, pp. 345–405. ISSN: 0360-0300.

Bai, X. et al. (2018). "Finite element modeling of grain size effects on the ultrasonic microstructural noise backscattering in polycrystalline materials". In: *Ultrasonics* 87, pp. 182–202. ISSN: 0041-624X. DOI: 10.1016/j.ultras.2018.02.008. URL: http://dx.doi.org/10.1016/j.ultras.2018.02.008.

Bamber, J. C. and R. J. Dickinson (1980). "Ultrasonic B-scanning - a computer simulation". In: *Physics In Medicine and Biology* 25, pp. 463–479. ISSN: 0031-9155.

Barber, T. S. (2017). "Phased array inspection of small-bore pipe welds". PhD thesis. University of Bristol.

Ben-Menahem, A. and S. J. Singh (2012). *Seismic waves and sources*. Springer Science & Business Media.

Berlincourt, D. (1971). "Piezoelectric crystals and ceramics". In: *Ultrasonic transducer materials*. Springer, pp. 63–124.

Bradfield, G (1954). "Improvements in ultrasonic flaw detection". In: *Journal of the British Institution of Radio Engineers* 14.7, pp. 303–308.

Budyn, N. et al. (2018). "Sensitivity images for multi-view ultrasonic array inspection". In: DOI: 10.1063/1.5031558. URL: http://dx.doi.org/10.1063/1.5031558.

Budyn, N. et al. (2019). "A Model for Multiview Ultrasonic Array Inspection of Small Two-Dimensional Defects". In: *IEEE Transactions on Ultrasonics, Ferroelectrics, and Frequency Control* 66.6, pp. 1129–1139. ISSN: 1525-8955. DOI: 10.1109/tuffc.2019.2909988. URL: http://dx.doi.org/10.1109/TUFFC.2019.2909988.

Cohen, F. (1992). "Modeling of ultrasound speckle with application in flaw detection in metals". In: *IEEE Transactions on Signal Processing* 40.3, pp. 624–632. ISSN: 1053-587X. DOI: 10.1109/78.120805. URL: http://dx.doi.org/10.1109/78.120805.

Derin, H. et al. (1990). "Modeling and segmentation of speckled images using complex data". In: *IEEE Transactions on Geoscience and Remote Sensing* 28.1, pp. 76–87. ISSN: 0196-2892. DOI: 10.1109/36.45748. URL: http://dx.doi.org/10.1109/36.45748.

Dobson, J. and P. Cawley (2016). "Independent Component Analysis for Improved Defect Detection in Guided Wave Monitoring". In: *Proceedings of the Ieee* 104, pp. 1620–1631. ISSN: 0018-9219. DOI: 10.1109/JPROC.2015.2451218.

Dominguez, N., F. Reverdy, and F. Jenson (2014). "POD evaluation using simulation: A phased array UT case on a complex geometry part". In: DOI: 10.1063/1.4865073. URL: http://dx.doi.org/10.1063/1.4865073.

Drozdz, M. B. (2008). "Efficient finite element modelling of ultrasound waves in elastic media". PhD thesis. Imperial College London.

Erickson, B. J. et al. (2017). "Machine Learning for Medical Imaging". In: *RadioGraphics* 37.2, pp. 505–515. ISSN: 1527-1323. DOI: 10.1148/rg.2017160130. URL: http://dx.doi.org/10.1148/rg.2017160130.

Felice, M. V. et al. (2015). "Optimization of ultrasonic array inspections using an efficient hybrid model and real crack shapes". In: DOI: 10.1063/1.4914704. URL: http://dx.doi.org/10.1063/1.4914704.

Ghosh, S., Z. Nowak, and K. Lee (1997). "Tessellation-based computational methods for the characterization and analysis of heterogeneous microstructures". In: *Composites Science and Technology* 57, pp. 1187–1210. ISSN: 0266-3538.

Ghoshal, G. and J. A. Turner (2009). "Numerical Model of Longitudinal Wave Scattering in Polycrystals". In: *IEEE Transactions On Ultrasonics Ferroelectrics and Frequency Control* 56, pp. 1419–1428. ISSN: 0885-3010. DOI: 10.1109/TUFFC.2009.1197.

Glushkov, E. et al. (2006). "An analytically based computer model for surface measurements in ultrasonic crack detection". In: *Wave Motion* 43, pp. 458–473. ISSN: 0165-2125. DOI: 10.1016/j.wavemoti.2006.03.002.

Goodman, J. W. (2007). "Statistical properties of laser speckle patterns". In: *Topics in Applied Physics*. Springer Berlin Heidelberg, pp. 9–75. DOI: 10.1007/bfb0111436. URL: https://doi.org/10.1007/bfb0111436.

Green, R. E. and R. E. Green (1973). *Ultrasonic investigation of mechanical properties*. Vol. 3. Academic Press New York.

Greenspan, H., B. van Ginneken, and R. M. Summers (2016). "Guest Editorial Deep Learning in Medical Imaging: Overview and Future Promise of an Exciting New Technique". In: *IEEE Transactions on Medical Imaging* 35.5, pp. 1153–1159. ISSN: 1558-254X. DOI: 10.1109/tmi.2016.2553401. URL: http://dx.doi.org/10.1109/TMI.2016.2553401.

Hasegawa, T. and K. Yosioka (1969). "Acoustic-radiation force on a solid elastic sphere". In: *The Journal of the Acoustical Society of America* 46.5B, pp. 1139–1143.

Hellier, C. and M. Shakinovsky (2001). *Handbook of nondestructive evaluation*. Vol. 10. Mcgraw-hill New York.

Holmes, C., B. W. Drinkwater, and P. D. Wilcox (2005). "Post-processing of the full matrix of ultrasonic transmit-receive array data for non-destructive evaluation". In: *NDT & E International* 38, pp. 701–711. ISSN: 0963-8695. DOI: 10.1016/j.ndteint.2005.04.002.

Howry, D. H. (1957). "Techniques used in ultrasonic visualization of soft tissues". In: *Ultrasound in biology and medicine*, pp. 49–65.

Hunter, A. J., B. W. Drinkwater, and P. D. Wilcox (2010). "Autofocusing ultrasonic imagery for non-destructive testing and evaluation of specimens with complicated geometries". In: *NDT & E International* 43.2, pp. 78–85. ISSN: 0963-8695. DOI: 10.1016/j.ndteint.2009.09.001. URL: http://dx.doi.org/10.1016/j.ndteint.2009.09.001.

Huntington, H. B. (1950). "On ultrasonic scattering by polycrystals". In: *Journal of the Acoustical Society of America* 22, pp. 362–364. ISSN: 0001-4966.

Huthwaite, P. (2014). "Accelerated finite element elastodynamic simulations using the GPU". In: *Journal of Computational Physics* 257, pp. 687–707. ISSN: 0021-9991. DOI: 10.1016/j.jcp.2013.10.017.

Iakovleva, E. et al. (2014). "Multi-Mode TFM Imaging with Artifacts Filtering Using CIVA UT Forwards Models". In: *40th Annual Review of Progress In Quantitative Nondestructive Evaluation: Incorporating the 10Th International Conference On Barkhausen Noise and Micromagnetic Testing, Vols 33A & 33B* 1581, pp. 72–79. ISSN: 0094-243X. DOI: 10.1063/1.4864804.

Iyer, S. R., S. K. Sinha, and A. J. Schokker (2005). "Ultrasonic C-scan imaging of post-tensioned concrete bridge structures for detection of corrosion and voids". In: *Computer-Aided Civil and Infrastructure Engineering* 20.2, pp. 79–94.

Knopp, J. S. et al. (2007). "Investigation of a model-assisted approach to probability of detection evaluation". In: *Review of Progress In Quantitative Nondestructive Evaluation, Vols 26A and 26B* 894, pp. 1775–1782. ISSN: 0094-243X.

Kocks, F., C. Tomé, and H.-R. Wenk (2000). *Texture and Anisotropy. Preferred Orientations in Polycrystals and Their Effect on Material Properties*. Cambridge University Press. ISBN: 052179420X.

Liu, Q. and H. Wirdelius (2007). "A 2D model of ultrasonic wave propagation in an anisotropic weld". In: *NDT & E International* 40.3, pp. 229–238. ISSN: 0963-8695. DOI: 10.1016/j.ndteint.2006.10.004. URL: http://dx.doi.org/10.1016/j.ndteint.2006.10.004.

Liu, Z. et al. (2007). "Survey: State of the Art in NDE Data Fusion Techniques". In: *IEEE Transactions on Instrumentation and Measurement* 56.6, pp. 2435–2451. ISSN: 0018-9456. DOI: 10.1109/tim.2007.908139. URL: http://dx.doi.org/10.1109/TIM.2007.908139.

Lord, W., R. Ludwig, and Z. You (1990). "Developments in ultrasonic modeling with finite element analysis". In: *Journal of Nondestructive Evaluation* 9.2-3, pp. 129–143. DOI: 10.1007/bf00566389. URL: https://doi.org/10.1007/bf00566389.

Ludwig, R. and W. Lord (1988). "A finite-element formulation for the study of ultrasonic NDT systems". In: *IEEE transactions on ultrasonics, ferroelectrics, and frequency control* 35.6, pp. 809–820.

Margetan, F., R. Thompson, and I. Yalda-Mooshabad (1993). "Modeling Ultrasonic Microstructural Noise in Titanium Alloys". English. In: *Review of Progress in Quantitative Nondestructive Evaluation*. Ed. by D. Thompson and D. Chimenti, pp. 1735–1742.

Mason, W. P. and H. J. McSkimin (1948). "Energy losses of sound waves in metals due to scattering and diffusion". In: *Journal of Applied Physics* 19, pp. 940–946. ISSN: 0021-8979.

Miller, G. F. and H. Pursey (1954). "The field and radiation impedance of mechanical radiators on the free surface of a semi-infinite isotropic solid". In: *Proceedings of the Royal Society of London Series A-Mathematical and Physical Sciences* 223, pp. 521–541.

Moser, F., L. J. Jacobs, and J. M. Qu (1999). "Modeling elastic wave propagation in waveguides with the finite element method". In: *NDT & E International* 32, pp. 225–234. ISSN: 0963-8695.

Nockemann, C., H. Heidt, and N. Thomsen (1991). "Reliability in NDT: ROC study of radiographic weld inspections". In: *NDT & E International* 24.5, pp. 235–245. ISSN: 0963-8695. DOI: 10.1016/0963-8695(91)90372-a. URL: http://dx.doi.org/10.1016/0963-8695(91)90372-A.

Papadakis, E. P. (1963). "Rayleigh and Stochastic Scattering of Ultrasonic Waves in Steel". In: *Journal of Applied Physics* 34.2, pp. 265–269. ISSN: 1089-7550. DOI: 10.1063/1.1702596. URL: http://dx.doi.org/10.1063/1.1702596.

Rayleigh, J. W.S. B. (1896). *The theory of sound*. Vol. 2. Macmillan.

Rummel, W. D. (1998). "Probability of Detection as a quantitative measure of nondestructive testing end-to-end process capabilities". In: *Materials Evaluation* 56.1, p. 29.

Růžek, R., R. Lohonka, and J. Jironč (2006). "Ultrasonic C-Scan and shearography NDI techniques evaluation of impact defects identification". In: *NDT & E International* 39.2, pp. 132–142. ISSN: 0963-8695. DOI: 10.1016/j.ndteint.2005.07.012. URL: http://dx.doi.org/10.1016/j.ndteint.2005.07.012.

Schmerr, L. W. (1998). *Fundamentals of Ultrasonic Non-Destructive Evaluation – A modelling approach*. New York: Plenum Press.

Shahjahan, S. et al. (2014). "A random matrix approach to detect defects in a strongly scattering polycrystal: How the memory effect can help overcome multiple scattering". In: *Applied Physics Letters* 104.23, p. 234105. ISSN: 1077-3118. DOI: 10.1063/1.4882421. URL: http://dx.doi.org/10.1063/1.4882421.

Smith, K. et al. (2007). "Model-Assisted Probability of Detection Validation for Immersion Ultrasonic Application". In: *AIP Conference Proceedings*. ISSN: 0094-243X. DOI: 10.1063/1.2718184. URL: http://dx.doi.org/10.1063/1.2718184.

Sokolov, S. (1929). "On the problem of the propagation of ultrasonic oscillations in various bodies". In: *Elek Nachr Tech* 6.454-460, p. 92.

Somer, J. C. (1968). "Electronic sector scanning for ultrasonic diagnosis". In: *Ultrasonics* 6, pp. 153–&. ISSN: 0041-624X.

Stanke, F. E. and G. S. Kino (1984). "A unified theory for elastic wave propagation in polycrystalline materials". In: *The Journal of the Acoustical Society of America* 75.3, pp. 665–681. ISSN: 0001-4966. DOI: 10.1121/1.390577. URL: http://dx.doi.org/10.1121/1.390577.

Tattersall, H. G. (1973). "Ultrasonic pulse-echo technique as applied to adhesion testing". In: *Journal of Physics D-Applied Physics* 6, pp. 819–832. ISSN: 0022-3727.

Thompson, R. B. et al. (2009). "Recent advances in model-assisted probability of detection". In:

Thompson, R. and T. Gray (1986). "Use of ultrasonic models in the design and validation of new NDE techniques". In: *Philosophical Transactions of the Royal Society of London. Series A, Mathematical and Physical Sciences* 320.1554, pp. 329–340.

Van Pamel, A. et al. (2017). "Finite-element modelling of elastic wave propagation and scattering within heterogeneous media". In: *Proceedings of the Royal Society A-Mathematical Physical and Engineering Sciences* 473. ISSN: 1364-5021. DOI: 10.1098/rspa.2016.0738.

Varatharajulu, V. and Y. H. Pao (1976). "Scattering matrix for elastic-waves. 1. Theory". In: *Journal of the Acoustical Society of America* 60, pp. 556–566. ISSN: 0001-4966.

Welsby, V. G. and J. Dunn (1963). "A high-resolution electronic sector-scanning sonar". In: *Radio and Electronic Engineer* 26.3, pp. 205–208.

White, R. M. (1958). "Elastic wave scattering at a cylindrical discontinuity in a solid". In: *Journal of the Acoustical Society of America* 30, pp. 771–785. ISSN: 0001-4966.

Whittaker, V. (1972). "A review of non-destructive measurement of flaw size". In: *Non-Destructive Testing* 5.2, pp. 92–100.

Wilcox, P. D., D. O. Thompson, and D. E. Chimenti (2011). "Array imaging of noisy materials". In: DOI: 10.1063/1.3591941. URL: http://dx.doi.org/10.1063/1.3591941.

Wilcox, P. D. and A. Velichko (2010). "Efficient frequency-domain finite element modeling of two-dimensional elastodynamic scattering". In: *Journal of the Acoustical Society of America* 127, pp. 155–165. ISSN: 0001-4966. DOI: 10.1121/1.3270390.

Willems, H (1987). "A new method for the measurement of ultrasonic absorption in polycrystalline materials". In: pp. 473–481.

Yalda, I., F. J. Margetan, and R. B. Thompson (1996). "Predicting ultrasonic grain noise in polycrystals: A Monte Carlo model". In: *Journal of the Acoustical Society of America* 99, pp. 3445–3455. ISSN: 0001-4966.

Yu, L., R. B. Thompson, and F. J. Margetan (2010). "The spatial correlation of backscattered ultrasonic grain noise: theory and experimental validation". In: *IEEE transactions on ultrasonics, ferroelectrics, and frequency control* 57.2, pp. 363–378.

Zener, C. M. and S. Siegel (1949). "Elasticity and Anelasticity of Metals." In: *The Journal of Physical Chemistry* 53.9, pp. 1468–1468.

Zhang, J. et al. (2010). "Defect detection using ultrasonic arrays: The multi-mode total focusing method". In: *NDT & E International* 43.2, pp. 123–133.

Zhang, J. et al. (2018). "Methodologies for validating ray-based forward model using finite element method in ultrasonic array data simulation". In: DOI: 10.1063/1.5031559. URL: http://dx.doi.org/10.1063/1.5031559.

Zhang, X. G. et al. (2004). “Ultrasonic attenuation due to grain boundary scattering in copper and copper-aluminum”. In: *Journal of the Acoustical Society of America* 116, pp. 109–116. ISSN: 0001-4966. DOI: 10.1121/1.1744752.